الجـــمـهـوريـــة الجـزائـريـة الديمـقـراطيـة الـشـعـبيـة

PEOPLE'S DEMOCRATIC REPUBLIC OF ALGERIA

وزارة التـــعـليـــم العـــــالي والبـــحث العـــــلـمـــي

MINISTRY OF HIGHER EDUCATION AND SCIENTIFIC RESEARCH

جـــــــــــامعة سعيدة – د. الطاهر مولاي –

University of Saida - Dr. MOULAY TAHAR
Faculty of Technology

A, Dissertation Submitted to the Department of Telecommunications in Partial Fulfillment of the Requirements for Degree of Master of Systems of Telecommunications

Title

Study and Design of Planar Hyperfrequency Filters Application to Millimeter and Sub-millimeter Frequencies in DGS Technology

Presented by: **Tennah Yousra**
Addadi Faiza

Defended on June, 2024 in front of the jury composed of :

Miss. NOURI Keltouma	Prof	President
Mr. DAMOU Mehdi	Dr	Supervisor
Mr. BOUBAKER.H	Dr	Examiner
Mr. GOUNI Slimane	Dr	Co-Supervisor

2023/2024

Acknowledgment

First of all, I thank ALLAH the Almighty for helping me and giving me the will to complete this final year project.

We would like to first thank my parents who supported me throughout the period of my studies, for helping me and guiding me to the right path.

We would like to thank my supervisor Mr. DAMOU. MEHDI and my co-supervisor M.. GOUNI SLIMAN. A for directing this work.

We thank the members of jury Miss .K.NOURI and Mr. BOUBAKER.H

Our thanks also go to all the professors

We would like to thank all of our colleagues and friends who have helped

And finally, We thank everyone who contributed directly or indirectly to the realization of this final year project.

Dedication

This dissertation is dedicated to my father,

Who taught me that the best kind of

Know ledge to have is that which is learned for its own sake. It

is also dedicated to my mother,

Who taught me that even the largest task can be

accomplished if It is done one step at a time.

To all my dearest brothers and sisters, a big thank

for their support and encouragement and for

putting color sin my life, may Allah bless you all.

TENNAH YOUSRA

Dedication

This dissertation is dedicated to my father,

Who taught me that the best kind of

Know ledge to have is that which is learned for its own sake. It

is also dedicated to my mother,

Who taught me that even the largest task can be

accomplished if it is done one step at a time.

To all my dearest brothers and sisters, a big thank

for their support and encouragement and for

putting color sin my life, may Allah bless you all.

ADDADI FAIZA

Abstract

Abstract

Microwaves, with frequencies between 300 MHz and 300 GHz, are used in various applications. Filter networks manipulate signals at different frequencies in microwave systems. Designing filters can be challenging due to material properties and dimensions.

Techniques like defected-ground structures (DGS) and Substrate Integrated Waveguide (SIW) improve filtering mechanisms. HFSS software is commonly used for filter design and frequency response analysis. This dissertation presents various designs of microwave devices, including band-pass filters, using different technologies and modeling techniques.

The research contributes to the development of communication and sensing technologies.

Key words:

microwave , filter , frequencies , design , material , dimensions , DGS , SIW, band-passe filters , HFSS , modelling techniques .

ملخص

تستخدم الموجات الدقيقة بترددات تتراوح بين 300 ميجاهرتز و300 جيجا هرتز في العديد من التطبيقات. تعالج شبكات الترشيح الإشارات عند ترددات مختلفة في أنظمة الموجات الدقيقة. قد يكون تصميم المرشحات أمرًا صعبًا بسبب خصائص المواد وأبعادها. تعمل تقنيات مثل الهياكل الأرضية المنشقة (DGS) والدليل الموجي المتكامل للركيزة (SIW) على تحسين آليات الترشيح. يشيع استخدام برنامج HFSS لتصميم المرشحات وتحليل استجابة التردد. تقدم هذه الأطروحة تصميمات مختلفة لأجهزة الموجات الدقيقة، بما في ذلك مرشحات تمرير النطاق، باستخدام تقنيات وتقنيات النمذجة المختلفة. يساهم البحث في تطوير تقنيات الاتصالات والاستشعار.

الكلمات المفتاحية :

الميكروويف , مرشح, التصميم, المواد, الأبعاد. , SIW,DGS, مرشحات , تمرير النطاق , HFSS, التقنيات

Résumé

Les micro-ondes, avec des fréquences comprises entre 300 MHz et 300 GHz, sont utilisées dans diverses applications. Les réseaux de filtres manipulent des signaux à différentes fréquences dans les systèmes micro-ondes. La conception de filtres peut être difficile en raison des propriétés et des dimensions des matériaux. Des techniques telles que les structures de sol défectueuses (DGS) et le guide d'ondes intégré au substrat (SIW) améliorent les mécanismes de filtrage.

Le logiciel HFSS est couramment utilisé pour la conception de filtres et l'analyse de la réponse en fréquence. Cette thèse présente diverse conceptions de dispositifs micro-ondes, y compris des filtres passe-bande, utilisant différentes technologies et techniques de modélisation. La recherche contribue au développement des technologies de communication et de détection.

Mots-clés : Micro-onde , fréquences , filtres , matériaux , dimensions DGS , SIW , filtre passe bande, HFSS , technique de modélisation .

List of contents

List of Contents

Chapter 2: DGS (Detected Ground Structure) Filter

Chapter 3: Substrate Integrated Waveguide (SIW)

Chapter 4: Simulation And Results

List of Tables

LIST OF TABLES

Chapter 1 : Microwave Filters

Chapter 2: DGS (Detected Ground Structure) Filter

Chapter 3: Substrate Integrated Waveguide (SIW)

Chapter 4: Simulation And Results

List of Figures

LIST OF FIGURES

Chapter 1: Microwave Filters

Chapter 2: DGS (Detected Ground Structure) Filter

Chapter 3: Substrate Integrated Waveguide (SIW)

Chapter 4: Simulation And Results

List of abbreviations

LIST OF ABBREVIATIONS

RF	Radio Frequency
EM	Electromagnetic
TE	Transverse Electric
TM	Transverse Magnetic
LPF	Low pass Filter
BPF	Band pass Filter
FBW	Fractional Bandwidth
WG	Wave Guide
HFSS	High Frequency Structural Simulator
BW	Bandwidth
DGS	Defected ground structure
AWR	Design Environnent.
SIW	Substrate Integrated Waveguide
LTCC	Low-Temperature Co-fired Ceramics
DFWG	Dielectric-filled waveguide
AFWG	Air-filled waveguide

List of Symbols

LIST OF SYMBOLS

f	Frequency
ω	angular frequency
fo	central frequency
fc	cutoff frequency
L	Inductance
C	Capacitance
R	Resistance
εr	relative dielectric constant of the material
εeff	effective dielectric constant
h	substrate height
Zo	characteristic impedance
λo	wavelength in free space
λg	wavelength in the guided medium
E	electric field
H	magnetic field
μ	permeability of the medium
C	velocity of light in free space
Q_e	quality factor

General Introduction

General Introduction

Microwaves are electromagnetic waves that have frequency between 300 MHz and 300 GHz, corresponding to wavelengths between 1 m and 1 mm in free space. Because the wavelengths of electromagnetic waves in the millimeter range (1–10 mm), those with frequencies over 30 and up to 300 GHz are also referred to as millimeter waves. It is the radio-frequency (RF) spectrum that is used for microwave frequencies. Depending on the specific technologies created for the exploitation of that particular frequency range, the boundary between radio frequency (RF) and microwaves might be relatively arbitrary. Thus, the term "RF/microwave applications" can also refer to radio astronomy, sensing, radar, communications, navigation, medical instrumentation, and other fields that investigate the use of frequency spectrums in this range.

In RF/microwave systems, filter networks are used to combine, reject, or choose signals at various frequencies. At lower frequencies, distributed structures with coupling elements are utilized in filter design, but at microwave frequencies, lumped elements are more frequent. The design of microwave filters is difficult because of material properties and geometric dimensions. The first step in the process is to translate the filter parameters into physical dimensions by defining a rational function.

Contemporary microwave communication systems often use high-performance and small filtering mechanisms, such as defected-ground structures (DGS). Filtering circuits use DGS cells with intrinsic resonant features to improve pass and stop bands. Commercial solvers were used to analyze transmission characteristics of printed transmission lines with DGS. Accurate modeling techniques and design equations were essential for optimizationare discussed in chapter 2with design examples.Comparable circuit representations facilitate design, and circuit simulators can quickly and cheaply compute outcomes.

In order to construct waveguides for microwave and millimeter-wave circuits, the Substrate Integrated Waveguide (SIW) approach is investigated in the chapter 3. Among other production techniques, it discusses metallic waveguide technologies and printed planar technologies. Complete shielding and minimal losses are provided by metallic waveguide technology, but it is more labor-intensive and time-consuming than printed components, which are less expensive, lightweight, and small.

The final chapter discusses the design of microwave filters using HFSS software, a tool that aids in filter design and frequency response plotting. It also explores a new type of microstripresonator and a new class of bandpass SIW filters, demonstrating their applications in filter applications

CHAPTER 1 :

Microwave Filters

1.1 Introduction

Filter networks are used to select/reject or separate/combine signals at different frequencies in a host of RF/microwave systems and equipment. Although the physical realization of filters at RF/microwave frequencies may vary, the circuit network topology is common to all.

Lumped elements filter design is well established [1]. These filters are generally used at lower frequencies due to the rapid degradation of the performance as the frequency increases. For microwave frequencies where lumped components are not practical, microwave filters are implemented using distributed structures with coupling elements to achieve specified transfer characteristics. The design of microwave filters is a vastly more challenging engineering task.

In general, the response of a microwave filter is controlled by the geometrical dimensions and the material parameters. The design process starts by specifying a rational function that approximates the desired filter specifications [1].The design procedure involves translating the parameters of the equivalent circuit into physical dimensions within a selected technology. There is a need to determine an accurate set of structure parameters that meets desired requirements such as operating frequency, insertion loss, bandwidth, etc

1.2 Filter types

1.2.1 Low-pass filter

A low-pass filter is a filter that passes signals with a frequency lower than a certain cutoff frequency and attenuates signals with frequencies higher than the cut-off frequency [2]. The exact frequency response of the filter depends on the filter design. The filter is sometimes called a high-cut filter, or treble cut filter in audio applications. A low-pass filter is the complement of a high-pass filter .

1.2.2High-passfilter

A high-pass filter is an electronic filter that passes signals with a frequency higher than a certain cutoff frequency and attenuates signals with frequencies lower than the cutoff frequency. The amount of attenuation for each frequency depends on the filter design. A high-

pass filter is usually modeled as a linear time-invariant system. It is sometimes called a low-cut filter or bass-cut filter. High-pass filters have many uses, such as blocking DC from circuitry sensitive to non-zero average voltages or radio frequency devices. They can also be used in conjunction with a low-pass filter to produce a band-pass filter[3].

1.2.3Band-pass filter

A band-pass filter is a device that passes frequencies within a certain range and rejects (attenuates) frequencies outside that range.The concept of bandpass filter is a mathematical transformation applied to data (a signal). Implementation of a bandpass filter can be done digitally or with electronic components. This transformation has the function of attenuating the frequencies outside the bandwidth, the frequency interval between the cutoff frequencies. Thus, only the frequencies within this range are kept intact or with a low attenuation [1].

1.3RF Filters

A microwave filter is typically a passive, reciprocal, 2-port linear filter.

If port 2 of this device is terminated in a matched load, then we can relate the incident and output power as:

$$P_{out} = |S_{21}|^2 P_{inc} \tag{1.1}$$

We define this power transmission through a filter in terms of the power transmission:

$$|S_{21}|^2 = \frac{P_{out}}{P_{inc}} \tag{1.2}$$

Since microwave filters are typically passive, we find that:

$$0 \leq \frac{P_{out}}{P_{inc}} \leq 1 \tag{1.3}$$

In other words,$P_{out} \leq P_{inc}$

Two possibilities can happen to the missing power $P_{inc} - P_{out}$,either it will be absorbed (P_{abs}) by the filter (converted to heat), or converted it will be reflected (P_r) at the input port.

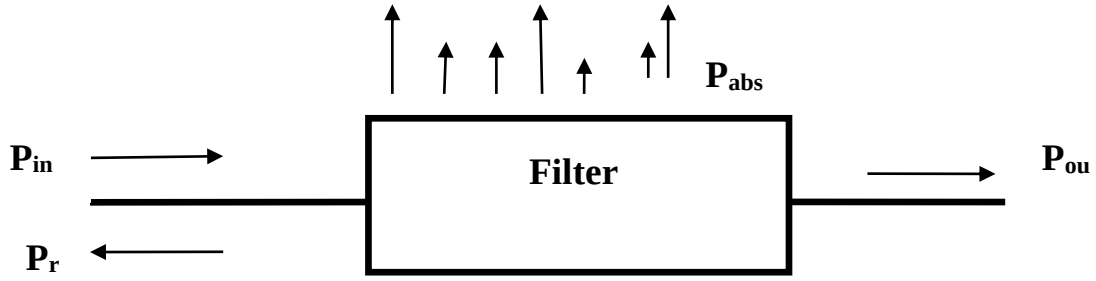

Thus, by conservation of energy:

$$P_{inc} = P_r + P_{abs} + P_{out} \tag{1.4}$$

Now ideally, a microwave filter is lossless, therefore $P_{abs} = 0$and:

$$P_{inc} = P_r + P_{out} \tag{1.5}$$

Which alternatively can be written as:

$$\frac{P_{inc}}{P_{inc}} = \frac{P_r + P_{out}}{P_{inc}} \tag{1.6}$$

$$1 = \frac{P_r}{P_{inc}} + \frac{P_{out}}{P_{inc}}$$

we can define ${P_r}/{P_{inc}}$ asthe power reflection coefficient :

$$\Gamma = \frac{P_r}{P_{inc}} = |S_{11}|^2 \tag{1.7}$$

We again emphasize that the filter output port is terminated in a matched load.

Thus, we can conclude that for a **lossless** filter:

$$|S_{11}| + |S_{21}| = 1 \tag{1.8}$$

1.3.1Insertion Loss:

In telecommunications, insertion loss is the loss of signal power resulting from the insertion of a device in a transmission line or optical fiber and is usually expressed in decibels (dB).

If the power transmitted to the load before insertion is P_T and the power received by the load after insertion is P_R, then the insertion loss in dB is given by

$$IL(dB) = 10log_{10}(\frac{P_T}{P_R}) \quad (1.9)$$

For passive filters, P_R will be smaller than P_T. In this case, the insertion loss is positive and measures how much smaller the signal is after adding the filter [4].

- **Link with scattering parameters:**

In case the two measurement ports use the same reference impedance, the insertion loss (IL) is defined as:

$$\text{IL}=-20log_{10}|S_{21}|\text{dB} \quad (1.10)$$

Here S_{11} and $S_{21}$are two of the scattering parameters. It is the extra loss produced by the introduction of the DUT between the 2 reference planes of the measurement. The extra loss can be introduced by intrinsic loss in the DUT and/or mismatch. In case of extra loss the insertion loss is defined to be positive [1].

1.3.2Cut-off frequency f_c

Cut-off frequency is the frequency at which the filter insertion loss is equal to 3 dB . It is a very convenient point for expressing the pass band and stop band boundary points. In addition, it allows a convenient means to normalize the frequency response of a filter.

1.3.3Center Frequencyf_0

Is the frequency at which band-pass filters are geometrically centered. For example, if f_1 and f_2 represent the 3 dB frequency points of a band-pass filter, then the center frequency $f_0$is calculated as follows:

$$f_0 = \sqrt{f_1 \times f_1} \quad (1.11)$$

When the bandwidth, f_2-f_1, is a small percentage of the value of f_0, then f_0, the geometric mean between f_2 and f_1, will approximately equal the arithmetic mean between f_1 andf_2

1.4Approximation and Synthesis

There are several approximations to the ideal lowpass filter. Butterworth, Chebyshev, elliptic, and pseudo-elliptic functions approximate the ideal lowpass magnitude response [2].

1.4.1Butterworth Function Approximation

The maximally flat or Butterworth approximation is the simplest meaningful approximation to an ideal lowpass filter. The amplitude-squared transfer function for Butterworth filters, which have an insertion loss A_{max}=3.01dB at the cutoff frequency w_c is given by:

$$|S_{21}(j\omega)|^2 = \frac{1}{1+\left(\frac{\omega}{\omega_c}\right)^{2n}} \tag{1.12}$$

This suggests that$(s) = 1, F(s) = s^n$ and $K(\omega) = \omega^n$ .Where n is the order of the prototype filter, which corresponds to the number of reactive elements, required in the lowpass prototype filter. It's all stopband zeros (transmission zeros) located at infinity [1].

The Butterworth approximation demonstrates maximal possible flatness of the insertion loss curve. The -3dB cutoff frequency occurs at ω_c= 1 rad/sec and marks the transition between the passband and stopband. This transition becomes more rapid when the order of the filter ishigher. The calculated maximally flat prototype transmission characteristics corresponding to different circuit orders are illustrated in Figure 1.1

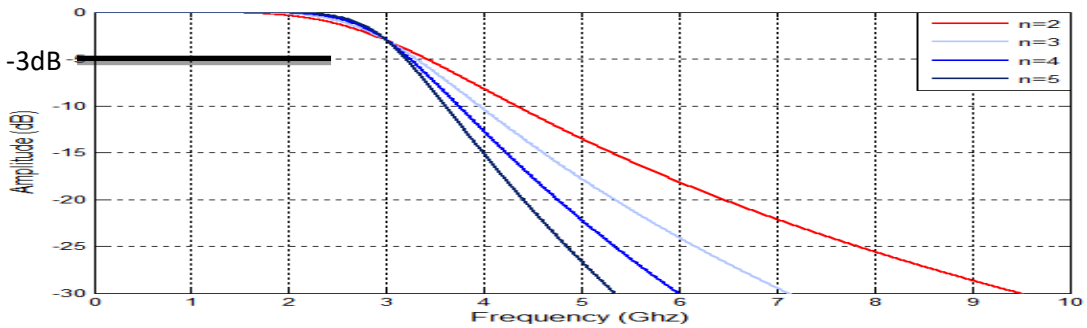

***Figure 1.1** : Butterworth response for various filter order n [2].*

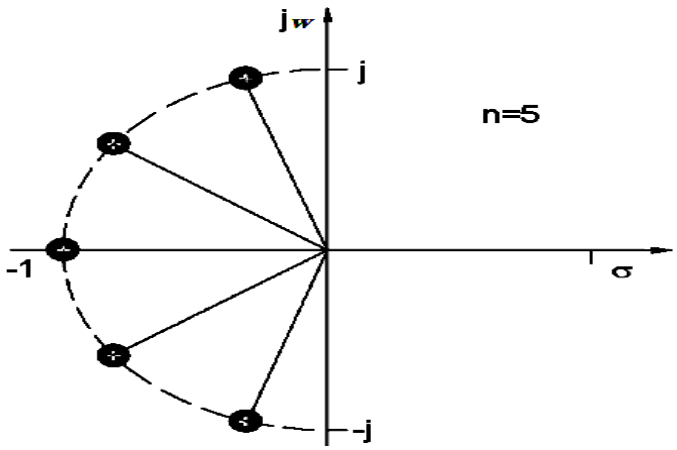

***Figure 1.2** : Pole distribution for Butterworth response*

1.4.2Chebyshev Function Approximation

- **Chebyshev Response:**

The Chebyshev response that exhibits the equal-ripple pass band and maximally flat

Stop and is depicted in Figure 1.3. The amplitude-squared transfer function that Describes this type of response is

$$|S_{21}(j\omega)|^2 = \frac{1}{1+\varepsilon^2 T_n^2(\omega)} \tag{1.13}$$

where the ripple constant $\varepsilon$is related to a given passband rippleA_{max} in dB by

$$\varepsilon=\sqrt{10^{\frac{L_{Ar}}{10}}-1} \tag{1.14}$$

and$T_n(\omega)$is a Chebyshev polynomial of degree n. Thus, $P(s)=1$, $F(s)=T_n(s/j)$

and $T_n(\omega)$, which can be expressed by

$$T_n(\omega)=\begin{cases}\cos(n\cos^{-1}\omega), \omega \le 1\\ \cosh(n\cosh^{-1}\omega), \omega \ge 1\end{cases} \tag{1.15}$$

Able to derived a general formula of the rational transfer function from (1.13) for the Chebyshev filter, that is [5]

The same as in the case of Butterworth, all transmission zeros are located at infinity.

Typical frequency response of the Chebyshev filter prototype is illustrated in Figure 1.3.

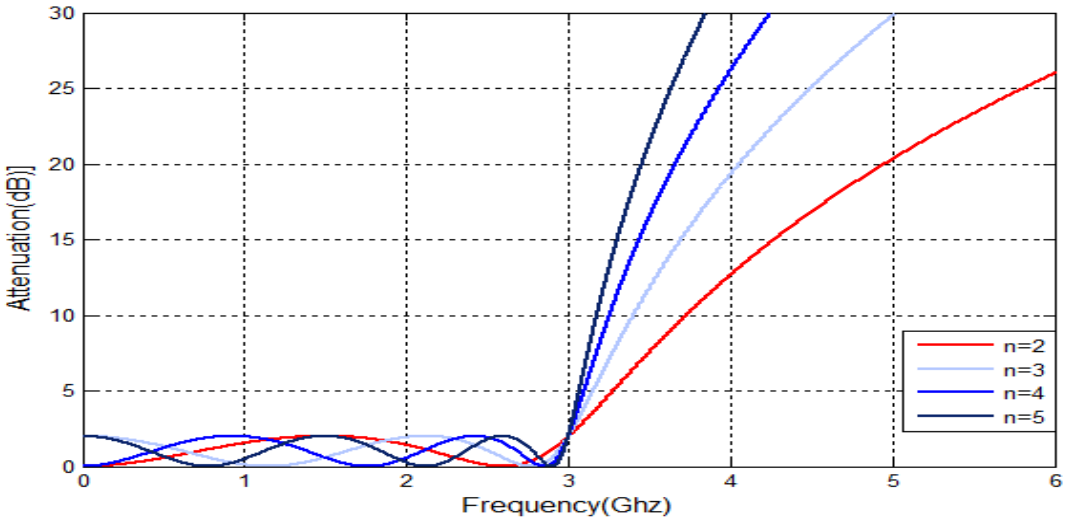

Figure 1.3 *: Chebyshev response for various filter order n*

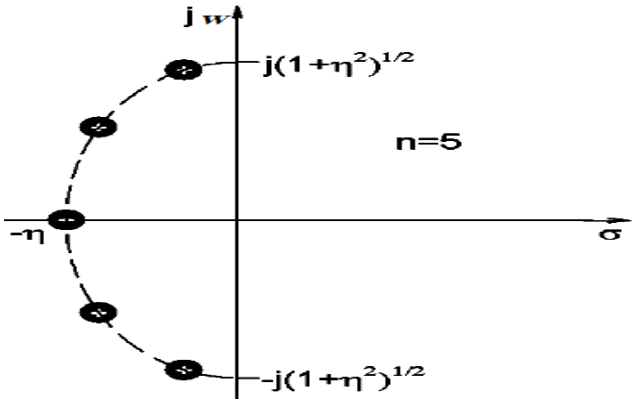

Figure 1.4 *: Pole distribution for Tchebychev response [1].*

1.5Lowpass prototype filters and elements

1.5.1Butterworth lowpass prototype filter

- The component values for a Butterworth lowpass prototype are determined using the following equations :

$$L_A(\omega') = 10\log_{10}\left[1 + \varepsilon^2\left(\frac{\omega}{\omega_c}\right)^{2n}\right] \qquad (1.16)$$

Where

$$\varepsilon = \sqrt{10^{\frac{L_{Ar}}{10}} - 1} \tag{1.17}$$

Or from The table below

Orders N	g_1	g_2	g_3	g_4	g_5	g_6	g_7	g_8
1	2.0000	1.0000						
2	1.4142	1.4142	1.0000					
3	1.0000	2.0000	1.0000	1.0000				
4	0.7654	1.8478	1.8478	0.7654	1.0000			
5	0.6180	0.6180	2.0000	1.6180	1.6180	1.0000		
6	0.5176	1.4142	1.9318	1.9318	1.4142	0.5176	1.0000	
7	0.4450	1.2470	1.8019	2.0000	1.8019	1.2470	0.4450	1.0000

Table 1.1: Elements values for Butterworth LPF [1].

1.5.2 Chebyshev lowpass prototype filter

- The component values for a Chebyshev lowpass prototype are determined using the following equations :

$$g_0 = 1$$

$$g_1 = \frac{2a_1}{\gamma}$$

$$g_k = \frac{4a_{k-1}a_k}{b_{k-1}g_{k-1}} \qquad (k = 2,3,4 \ldots . n)$$

$$g_{n+1} = \begin{cases} \coth\left(\frac{\beta}{4}\right)^2 & (\text{n even}) \\ 1 & (\text{n odd}) \end{cases} \tag{1.18}$$

Where

$$\beta = \ln\left(\coth\left(\frac{L_{Ar}}{17.372}\right)\right)$$

$$\gamma = \sinh\left(\frac{\beta}{2n}\right) \tag{1.19}$$

$$a_k = sin\left[\frac{(2k-1)\pi}{2n}\right], (k = 1,2, \ldots . . n) b_k = \gamma^2 + sin^2\left[\frac{k\pi}{2n}\right], (k = 1,2, \ldots . . n) \tag{1.20}$$

Where

n is the filter order.

Or from The table below

Orders	N	g_1	g_2	g_3	g_4	g_5	g_6	g_7	g_8
	1	0.3052	1.0000						
	2	0.8431	0.6620	1.3554					
	3	1.0316	1.1474	1.0316	1.0000				
	4	1.1088	1.3062	1.7704	0.8181	1.3554			
	5	1.1468	1.3712	1.9750	1.3712	1.1468	1.0000		
	6	1.1681	1.4040	2.0562	1.5171	1.9029	0.8618	1.3554	
	7	1.1812	1.4228	2.0967	1.5734	2.0967	1.4228	1.1812	1.0000

Table 1.2: Elements values for Chebyshev [1].

1.5.3Quasi-elliptic lowpass prototype filters

The synthesis procedures of lowpass prototype filters with Butterworth and Chebyshev characteristics are given above. For these two types of responses, all of transmission zeros (attenuation poles) are at infinite frequencies.

Where the transmission zeros are at $\omega' = \pm\omega'_a$and infinity. Some useful quasi-elliptic filtershave been synthesized in [1].

The general synthesis process to find the values of elements in the prototype quasi-elliptic low pass filter has been given in [9].

However, the exact synthesis procedure is quite complicated, and there does not existclosed-form formulas for the element values of quasi-elliptic filters as those for Butterworth and Chebyshev filters.

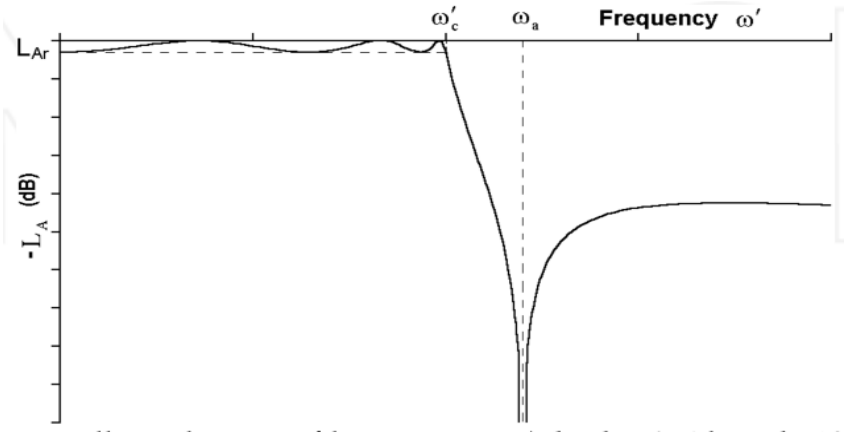

***Figure 1.5** : A typical quasi-elliptic lowpass filter response [9].*

1.6Elements Transformations

1.6.1Steps for designing Bandpass Filter

- Center frequency f_0 =910MHz.
- Bandwidth BW= 40MHz.
- Maximum pass band return loss RL <-20 dB.
- Pass band ripples value is 0.04dB.
- $A_{s1} \geq 30$ dB for$f_{s1}>$ 11.35GHz,
- $A_{s2}\geq$ 30dB dB for f_{s2}>10.62 GHz.
- Tchebychev characteristic.

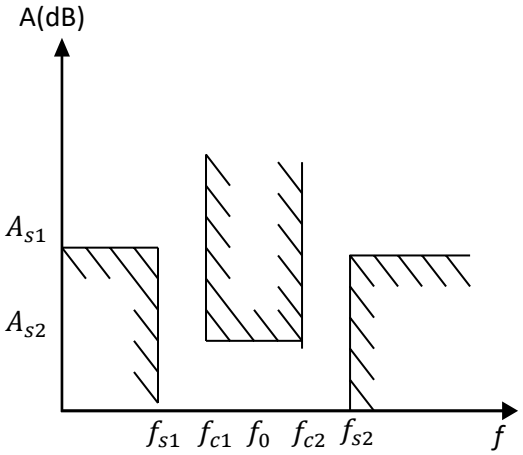

1.6.2Bandpass Transformation

A low-pass filter may be converted to a bandpass filter response with a passbandω_2-ω_1, where$\omega_1$and $\omega_2$denote the passband-edge angular frequency, the required frequency transformation can be described as[1][5]:

$$\Omega = \frac{f_c}{FBW}\left(\frac{\omega}{\omega_0}-\frac{\omega_0}{\omega}\right) \tag{1.21}$$

$$FBW = \frac{\omega_2-\omega_1}{\omega_0} \tag{1.22}$$

$$\omega_0 = \sqrt{\omega_1\omega_2}$$

- Where Ω and ω are angular frequencies of the LPF and BPF respectively.
- The lowpass prototype filter has a cutoff frequency $\Omega_c = 1 rad/s$ and a normalized source impedance g_0=1
- *FBW* is referred to as the fractional bandwidth; $\omega_0$is the centre frequency.
- The impedance scaling factor $\gamma_0$is defined as:‘

$$\gamma_0 = \begin{cases} Z_0 / g_0 & \text{for } g_0 \text{ being the resistance} \\ g_0 Z_0 & \text{for } g_0 \text{ being the conductance} \end{cases}$$

If we apply this frequency transformation to a reactive element g of the lowpass prototype [1], we have:

$$j\Omega g \rightarrow j\omega \frac{\Omega_c g}{FBW} + \frac{1}{j\omega} \frac{\Omega_c \omega_0 g}{FBW} \tag{1.23}$$

An inductive/capacitive element g in the lowpass prototype will transform to a series/parallel LC resonant circuit in the bandpass filter, where, the impedance scaling has been taken into account as well [1].

$$j\Omega g = j\frac{\Omega_c}{FBW}\left(\frac{\omega}{\omega_0} - \frac{\omega_0}{\omega}\right)g = j\frac{\Omega_c}{FBW}\frac{\omega}{\omega_0}g - j\frac{\Omega_c}{FBW}\frac{\omega_0}{\omega}g$$

$$L_s = \left(\frac{\Omega_c}{\omega_0 FBW}\right)\gamma_0 g \qquad C_s = \left(\frac{FBW}{\omega_0 \Omega_c}\right)\frac{1}{\gamma_0 g} \qquad L_p = \left(\frac{\Omega_c}{\omega_0 FBW}\right)\frac{\gamma_0}{g} \qquad C_p = \left(\frac{FBW}{\omega_0 \Omega_c}\right)\frac{g}{\gamma_0}$$

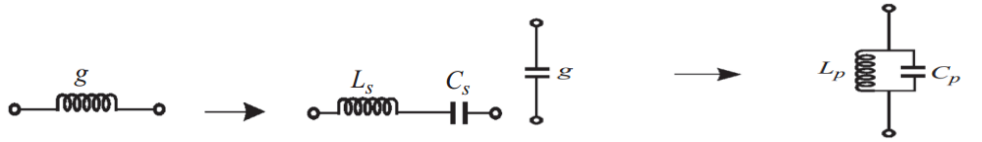

for **g** represent the inductance for **g** represent the capacitance

1.7.Immittanceinverters

1.7.1. Filters with immittance inverters

A series inductance with an inverter on each side looks like a shunt capacitance from its exteriors terminals, likewise a shunt capacitance with an inverter on each side looks like a series inductance from its external terminals.

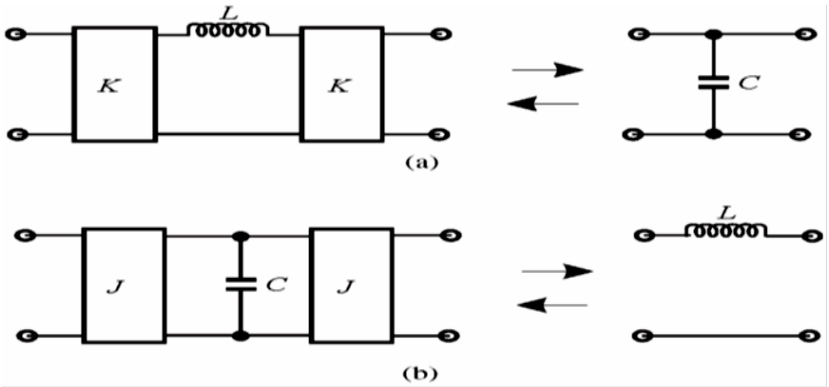

***Figure 1.6** : (a) Immittance inverters used to convert a shunt capacitance into an equivalent circuit with series inductance. (b) Immittance inverters used to convert a series inductance into an equivalent*

circuit with shunt capacitance.

Inverters have the ability to shift impedance or admittance levels depending on the choice of K or J parameters.

Making use these properties enable us to convert a filter circuit to an equivalent form that would be more convenient for implementation with microwave structures.

1.7.2 Bandpass filters with Immittance inverters

Since the source, impedances are assumed the same in the both filters as indicated, no impedance scaling is required.

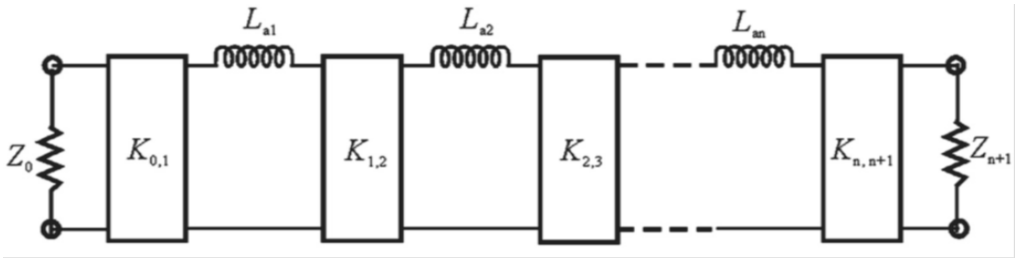

Figure 1.7 *: Lowpass prototype filters modified to include impedance inverters*

$$K_{0,1} = \sqrt{\frac{Z_0 L_{a1}}{g_0 g_1}}\,,\ K_{i,j+1} = \sqrt{\frac{L_{ai} L_{a(i+1)}}{g_i g_{i+1}}}\,,\ K_{n,n+1} = \sqrt{\frac{L_{an} Z_{n+1}}{g_n g_{n+1}}} \qquad (1.24)$$

Transforming the inductors of the lowpass filter to the series resonators of the bandpass filter, we obtain:

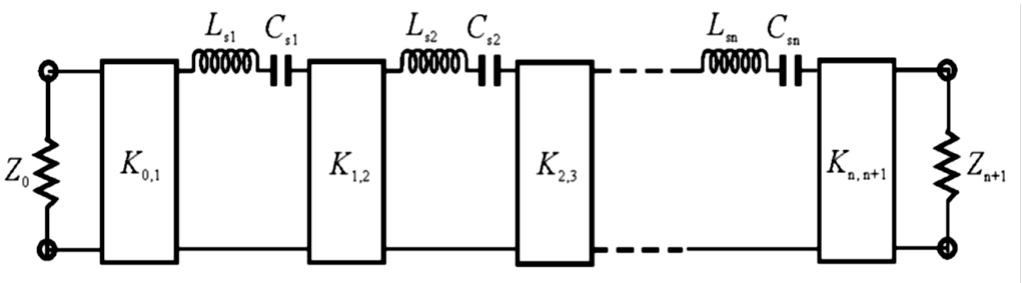

Figure 1.8 *: Bandpass filters using impedance inverters*

$$K_{0,1} = \sqrt{\frac{Z_0 FBW\,\omega_0 L_{s1}}{\Omega_c g_0 g_1}}, K_{i,j+1} = \frac{FBW\,\omega_0}{\Omega_c}\sqrt{\frac{L_{si} L_{s(i+1)}}{g_i g_{i+1}}}\,,\ K_{n,n+1} = \sqrt{\frac{FBW\,\omega_0 L_{sn} Z_{n+1}}{\Omega_c g_n g_{n+1}}} \qquad (1.25)$$

$$C_{si} = \left.\frac{1}{\omega_0^2 L_{si}}\right|_{i=1 \text{ to } n} \qquad (1.26)$$

Similarly, with the admittance inverters:

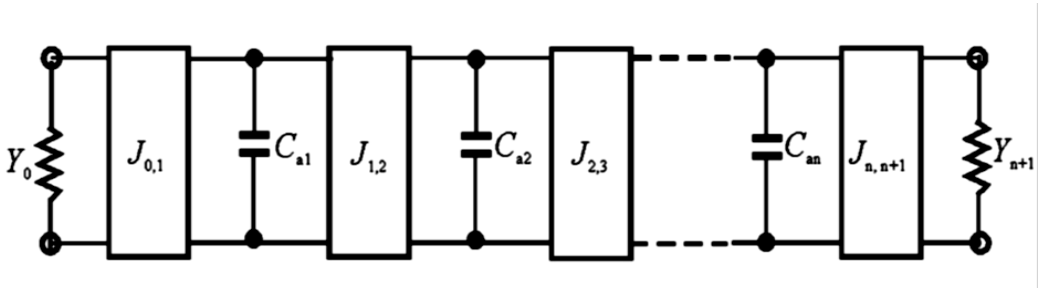

Figure 1.9 *: Lowpass prototype filters modified to include admittance inverters*

$$J_{0,1} = \sqrt{\frac{Y_0 C_{a1}}{g_0 g_1}}, J_{i,j+1} = \sqrt{\frac{C_{ai} C_{a(i+1)}}{g_i g_{i+1}}}, J_{n,n+1} = \sqrt{\frac{C_{an} Y_{n+1}}{g_n g_{n+1}}} \quad (1.27)$$

Transforming the capacitance of the lowpass filter to the shunt resonators of the bandpass filter, we obtain: $J_{0.1}$

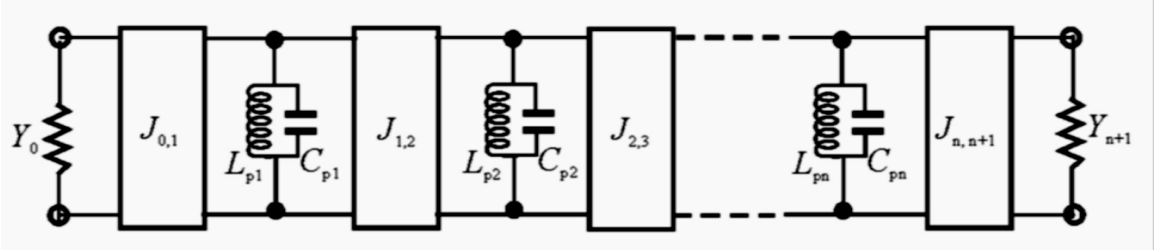

Figure 1.10 *: Band pass filter using admittance inverters*

$$J_{0,1} = \sqrt{\frac{Y_0 FBW \omega_0 C_{p1}}{\Omega_c g_0 g_1}}, J_{i,j+1} = \frac{FBW\omega_0}{\Omega_c}\sqrt{\frac{C_{pi} C_{p(i+1)}}{g_i g_{i+1}}}, J_{n,n+1} = \sqrt{\frac{FBW \omega_0 C_{pn} Y_{n+1}}{\Omega_c g_n g_{n+1}}} \quad (1.28)$$

$$L_{pi} = \frac{1}{\omega_0^2 C_{pi}}\Big|_{i=1 \text{ to } n} \quad (1.29)$$

1.7.3 Practical realization of immittance inverters

One of the simplest forms of the inverters is a quarter-wavelength of transmission lines. Besides a quarter-wavelength, there are some other circuits that operate as inverters. It should be noticed that some of the inductors and capacitors have negative values. Figure shows four typical lumped-element immittance inverters. While the inverters in figure 1.11 (a) and (b) are of interest for use as *K* inverters, those shown in figure 1.11(c) and (d) are of interest for use as J inverters [6].

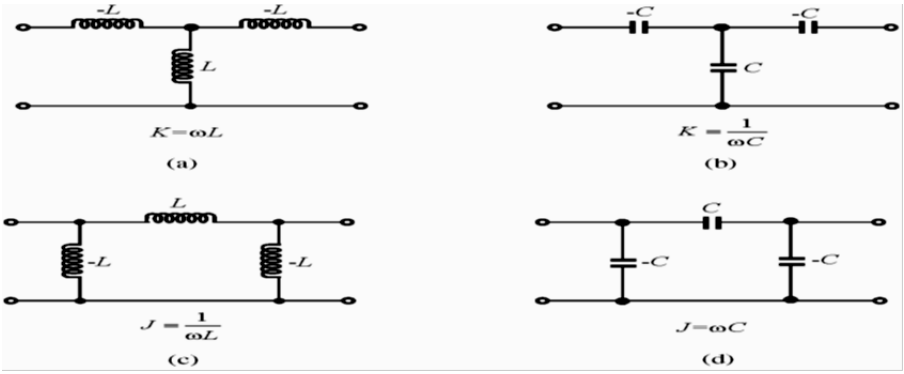

***Figure 1.11** : Lumped-element immittance inverters*

Any one of this inverters can be treated as either K or J inverter. It can be shown that the inverters in figure 1.11 (a) and (d) have a phase shift (the phase of S_{21}) of $+90^{\circ}$, while those figure 1.11 (b) and (c) have a phase shift of -90°,this is why the " $\pm$" and " $\mp$" signs appear in the $ABCD$ matrix expressions of immittance inverters.

1.8Synchronously Tuned Coupled-Resonator Circuits

1.8.1 Extraction of the Inter resonator Coupling Coefficient

1.8.1.1Electric coupling

Shown in figure 1.12 is an equivalent lumped element circuit model for electrically coupled resonator structures where L and$C$ are the self-inductance and self-capacitance, and Lrepresents the mutual inductance.

The equivalent circuit is shown in figure 1.12, it can be shown that the electric coupling between the two resonant loops is represented in by an impedance inverter$J = \omega C_m$.

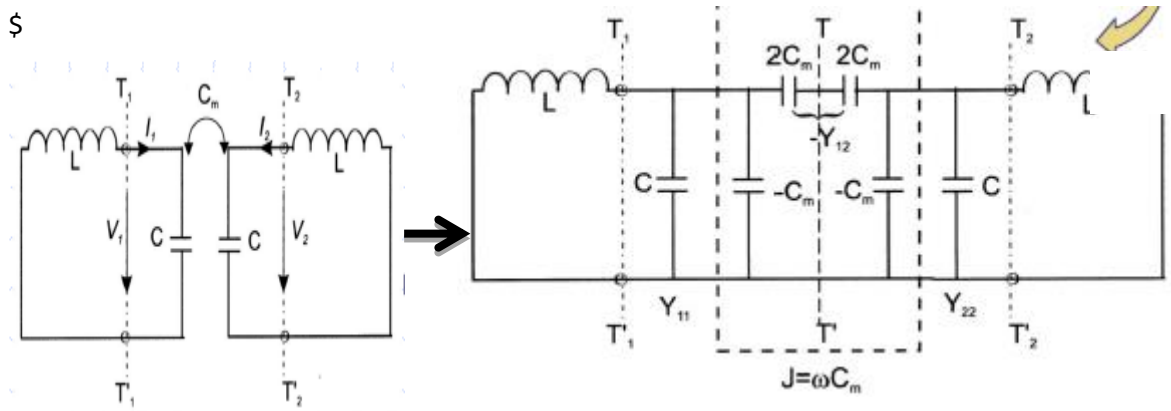

***Figure 1.12** : Synchronously tuned coupled resonator circuit with electric coupling represented by an admittance inverter* $J = \omega C_m$ *to represent the coupling.*

If the symmetry plane is replaced by an electric wall (or a short-circuit), the resultant circuit has a resonant frequency [1]:

$$f_e = \frac{1}{2\pi\sqrt{L(C + C_m)}} \tag{1.30}$$

This resonant frequency is lower than that of an uncoupled single resonator. A physical explanation is that the coupling effect enhances the capability to store charge of the single resonator when the electric wall is inserted in the symmetrical plane of the coupled structure. Similarly, replacing the symmetry plane by a magnetic wall (or an open circuit) results in a single resonant circuit having a resonant frequency [1].

$$f_m = \frac{1}{2\pi\sqrt{L(C - C_m)}} \tag{1.31}$$

In this case, the coupling effect reduces the capability to store charge so that the resonant frequency is increased.

the electric coupling coefficient k_E

$$k_E = \frac{f_m^2 - f_e^2}{f_m^2 + f_e^2} = \frac{C_m}{C} \tag{1.32}$$

which is not only identical to the defination of ratio of the coupled electric energy to the stored energy of uncoupled single resonator, but also consistent with the coupling coefficient for coupled-resonator filter.

1.8.1.2 Magnetic Coupling

Shown in figure 1.13 is an equivalent lumped element circuit model for magnetically coupled resonator structures where$L$ and$C$ are the self-inductance and self-capacitance, and Lrepresents the mutual inductance.

The equivalent circuit is shown in figure 1.13, it can be shown that the magnetic coupling between the two resonant loops is represented in by an impedance inverter $k = \omega L_m$.

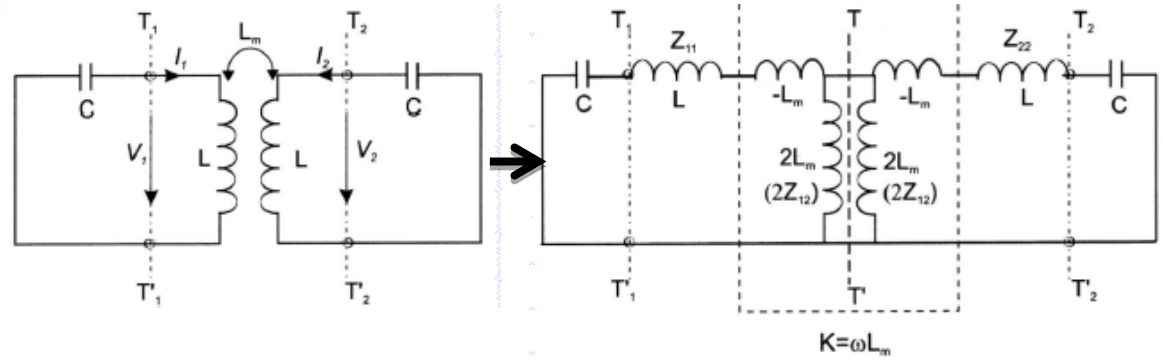

Figure 1.13 *: Synchronously tuned coupled resonator circuit with magnetic coupling represented by an impedance inverter $k = \omega L_m$ to represent the coupling[1] [2]*

If the symmetry plane is replaced by an electric wall (or a short-circuit), the resultant circuit has a resonant frequency:

$$f_e = \frac{1}{2\pi\sqrt{(L - L_m)C}} \tag{1.33}$$

It can be shown that the increase in resonant frequency is because the coupling effect reducing the stored flux in the single resonator circuit when the electric wall is inserted in the symmetric plane. If a magnetic wall (or an open-circuit) replaces the symmetry plane the resultant single-resonant circuit has a resonant frequency.

$$f_m = \frac{1}{2\pi\sqrt{(L + L_m)C}} \tag{1.34}$$

In this case, the coupling effect increases the stored flux, so that the resonant frequency is shifted down.

Similarly, equations (1.36) and (1.37) can be used to find the magnetic coupling coefficientk_M:

$$k_M = \frac{f_e^2 - f_m^2}{f_e^2 + f_m^2} = \frac{L_m}{L} \tag{1.35}$$

It should be emphasized that the magnetic coupling coefficient defined by eq. (1.37) corresponds to the defination of ratio of the coupled magnetic energy to the stored energy of an uncoupled single resonator [7].

1.8.1.3Mixed coupling

In this coupling, there is the both electric and magnetic coupling. By inserting an electric wall and a magnetic wall, respectively, we obtain:

$$f_e = \frac{1}{2\pi\sqrt{(L - L'_m)(C - C'_m)}} \tag{1.36}$$

$$f_m = \frac{1}{2\pi\sqrt{(L + L'_m)(C + C'_m)}} \tag{1.37}$$

Where C, L, C'_m and L'_m are the self-capacitance, the self-inductance, the mutual capacitance and the mutual inductance of an associated equivalent lumped-element circuit. We can also identify an impedance inverter $K = \omega L'_m$ and an admittance inverter$\mathrm{J} = \omega C'_m$, which represent the magnetic coupling and the electric coupling, respectively[8].

As can be seen, both the magnetic and the electric coupling have the same effect on the resonance frequency shifting.

From equations (1.36) and (1.37), the mixed coupling coefficient $K_x$can be found to be

$$K_x = \frac{f_e^2 - f_m^2}{f_e^2 + f_m^2} = \frac{CL'_m + LC'_m}{LC + L'_m C'_m} \tag{1.38}$$

It is reasonable to assume that $L'_m C'_m \ll LC$, and thus equation (1.37) becomes

$$k_x \approx= \frac{L'_m}{L} + \frac{C'_m}{C} = K'_M + K'_E \tag{1.39}$$

Which clearly indicate that the mixed coupling results from the superposition of the magnetic and electric coupling.

1.8.2Extraction of the External Quality FactorQ_e

The external quality factor of a single resonator can be found by simulating $|S_{21}|$ response with one port weakly coupled.

The external quality factor Q_e can then be calculated from the simulated $|S_{21}|$ response using the following formula:

$$Q_e = \frac{\omega_0}{\Delta\omega_{\pm 3dB}} \tag{1.40}$$

Where, ω_0 is the resonant frequency of the loaded resonator and $\Delta\omega_{\pm 3dB}$ is the 3 dB bandwidth.

1.9Microstrip Line

Microstrip line is a transmission line which consists of a conducting strip separated from a ground plane by a dielectric layer [10]. Figure (1.14) shows the cross section of the microstrip line and field lines .The characteristic impedance of the microstrip line is depending on the width of the guided wave line, substrate thickness

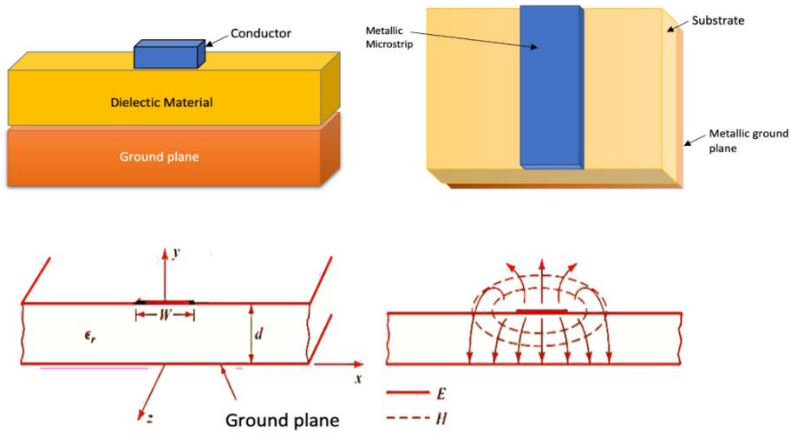

***Figure 1.14**: Microstrip cross section showing the parameters and field lines.*

However, with the presence of the two guided-wave media (the dielectric substrate and the air), the waves in a microstrip line will have no vanished longitudinal components of electric and magnetic fields and their propagation velocities will depend not only on the material properties, but also on the physical dimensions of the Microstrip

1.9.1 Quasi-TEM Approximation

Microstrip has most of its field lines in dielectric region , it's concentrated between the strip conductor and the ground plane, and some fraction in the air region above the substrate. This reason give microstrip cannot support the pure TEM wave [10]. When the longitudinal components of the fields for the dominant mode of a microstrip line remain very much smaller than the transverse components, they may be neglected. In this case, the dominant mode then behaves like a TEM mode and the TEM transmission-line theory is applicable for the microstrip line as well as this is called the quasi-TEM approximation. Figure (1.14) illustrates the cross section of field (E,H) distribution.

1.10 Conclusion

In this chapter we have established a brief state of the art of planar microwave filtering. We have highlighted the interest of topologies responding to approximation functions. As well as frequency transformations based on low-pass prototypes.

In addition gave some type of planar filters, Among these filters, We are interested in to the bandpass filter type Based on Microstrip line.

1.11 References

[1] J.S. Hong and M.J. Lancaster, Microstrip filters for RF/microwave applications, Wiley, New York, NY, 2001.
[2] Richard J Cameron, Chandra M Kudsia, and Raafat R Mansour. Microwave filters for communication systems. Wiley-Inter science, 2007.
[3] G. Matthaei, L. Young, and E.M.T. Jones, Microwave Filters, Impedance-Matching Networks, and Coupling Structures, Artech House, 1980.
[4] Talal F. Skaik, '' Synthesis of Coupled Resonator Circuits with Multiple Outputs using Coupling Matrix Optimization '', The University of Birmingham ,2011.
[5] D. G. Swanson, "Narrow-band microwave filter design," IEEE Microwave Magazine, pp. 105-114. Oct. 2007.
[6] Pozar D. "*Microwave Engineering*", Third Edition. John Wiley and Sons, USA, 2005, pp. 278- 279, 370-430.
[7] Ian Hunter. Theory and design of microwave filters. Number 48. Iet, 2001.
[8] David M Pozar. Microwave engineering. John Wiley & Sons, 2009.
[9] Rhodes, J. D., & Alseyab, S. A. (1980). A design procedure for bandpass channel

[10] Hammerstad E, Jensen O (1981) Accurate models for microstrip computer-aided design.Microw Symp Digest, MTT-S 81 (1):407–409

CHAPTER 2 :

DGS Filter

2.1 Introduction

The exacting specifications of contemporary microwave communication systems are often satisfied by high-performance and small filtering mechanisms. There have been many reports of such filters that use generic structures known as defected-ground structures (DGS). Filtering circuits have been using DGS cells with intrinsic resonant features to improve the characteristics of the pass and stop bands.

However, the conversation was restricted to the overviews of certain key DGS types. Commercial solvers were utilized in the initial development stage to analyze the transmission characteristics of a printed transmission line with a DGS underneath[1]. The engineers understood very well that accurate modeling techniques and suitable design equations were essential since there was no other way to optimize the geometry except via trial and error. The initial attempt, published in 2001[2], recommended evaluating a DGS by means of a comparable LC circuit. Comparable circuit representations facilitate the design process, especially when working with several DGS units. It is now feasible to swap out every DGS unit for its matching circuit and examine the outcomes using a circuit simulator, which computes quickly and cheaply. We have given a quick introduction to parameter extraction techniques and DGS modeling approaches in this chapter.

2.2 DGS Unit

here are the structures DGS for the shown analysis. This visual representation Figure 2.1 showcases a variety of attached area shapes, including square heads and H-head slots, each with unique and specialized characteristics.

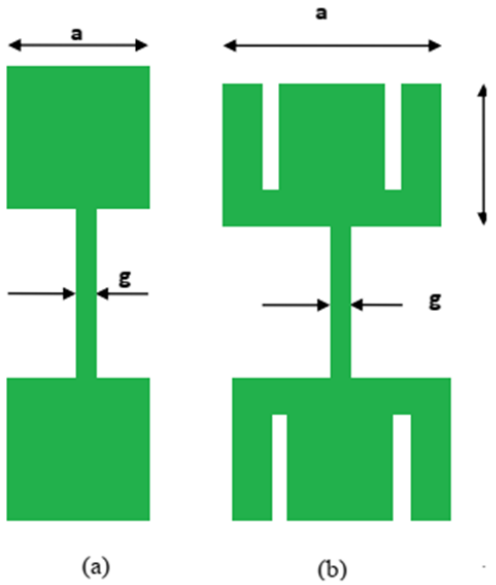

Figure 2.1:*shows the suggested DGS's (a) square head and (b) H-head configurations*

2.3 Characteristics of DGS Frequency

Etching offa defectfrom the ground plane ofa microstrip line realizes a DGS unit, outs a flaw from the microstrip line ground plane. The geometry of the defect form might be simple or complex. In the ground plane, an etched flaw modifies the shield current distribution. In order to get the band-stop property and slow-wave effect, this distribution modifies the capacitance and inductance of the transmission line. When linked in series with transmission lines at both ends, a DGS unit functions as a parallel RLC or LC resonant circuit. It can typically provide both strong attenuation qualities in the stopband and slow-wave propagation in the passband. There are two recognized DGS unit forms in this area.

as shown in Figure 2.2. On the rear metallic ground plane, the DGS has an etched H-head slot form. Without DGS periodicity, the DGS unit section may provide a cut-off frequency and attenuation pole at a certain frequency. We looked at the frequency characteristics of the DGS region using the HFSS simulator.

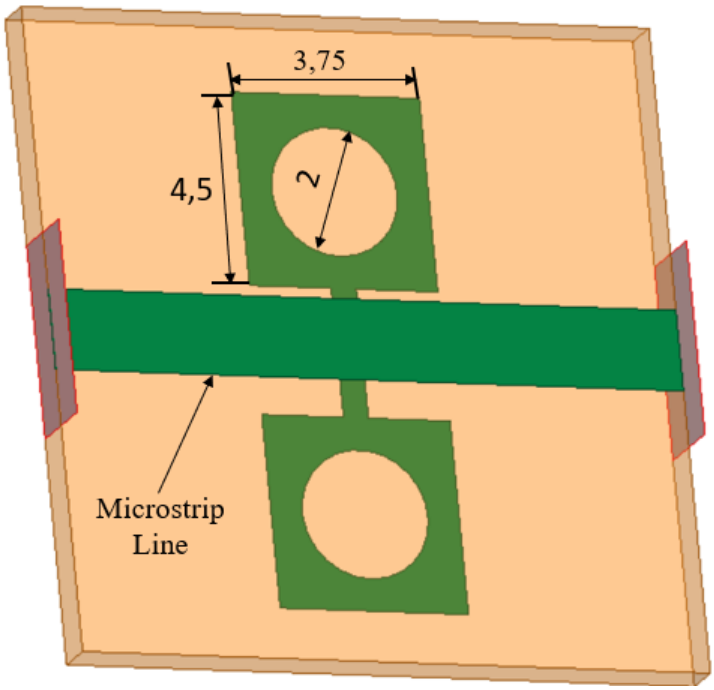

(a)

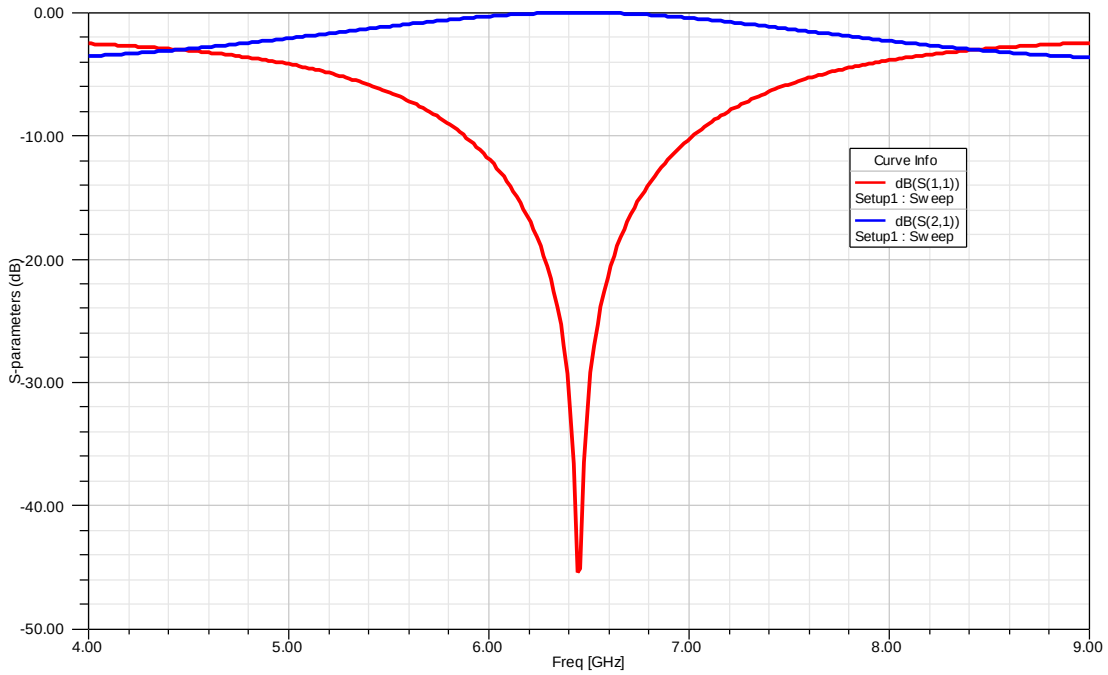

(b)

***Figure2.2*:**An H-head DGS in 3-D (b) The H-head DGS with EM simulation using S_{11} and S_{12}

2.4Modeling using LC and RLC

Below a 50 Ω microstrip line, Figure 2.3 displays a basic dumbbell-shaped DGS and its transmission characteristics, which vary based on the DGS parameters. In a parallel LC circuit, an attenuation pole and a cut-off indicate the typical resonance characteristics. This is the genesis of the notion that a DGS should have a comparable C and L combination, as Figure 2.5 illustrates.

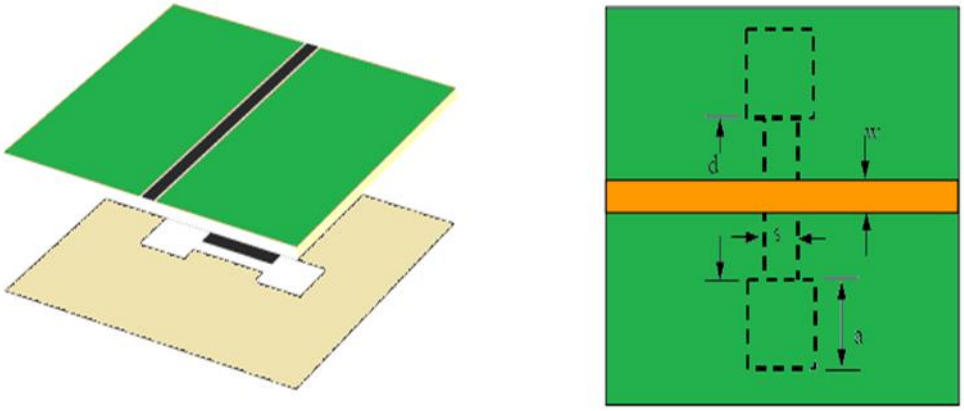

(a) (b)

Figure 2.3:(a) 3-D view of the rectangular DGS slot and (b) Wire frame view of the rectangular DGS slot

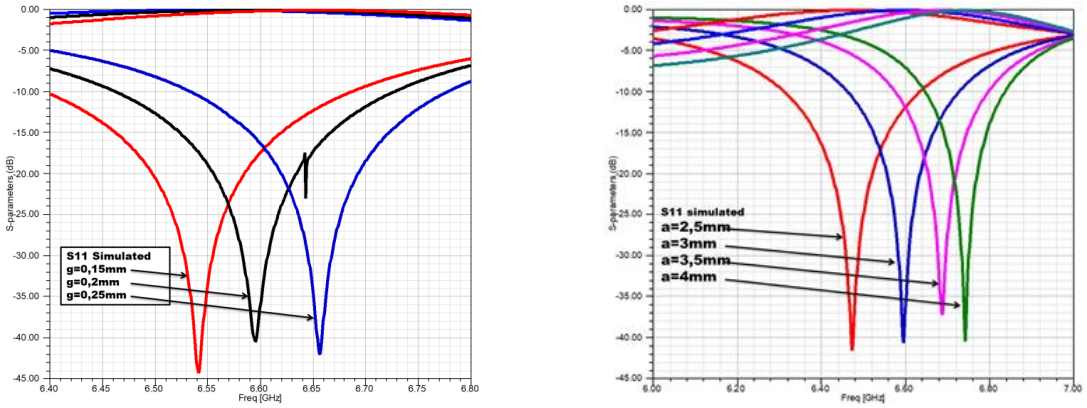

(a) (b)

Figure 2.4: (a) Modelled S-parameters by changing a, b and using g = 0.15mm; (b) Using a = b = 2.5mm and changing g, the S-parameters were simulated. With a line width of 1.57mm and a subsequent thickness of h = 1.575mm, ε_r = 9.8. Origin: Taken from An and colleagues

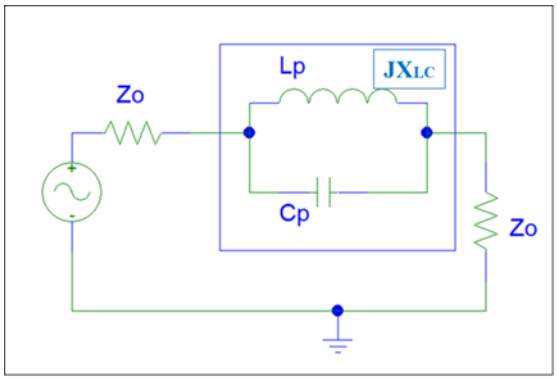

Figure 2.5: DGS single-cell equivalent circuit in dumbbell shape that is LC comparable. [1].

Two separate parts contribute to the equivalent capacitance and inductance of a dumbbell DGS. Electric fields coupled across the narrow connection slot provide an equivalent capacitance, while the current running around the square heads produces an analogous inductance. This feature is compatible with the fake S_{11}. This causes the attenuation poles to move towards the lower frequency, as seen in Figure 2.4a. On the other hand, Figure2.4bshows how the attenuation poles shift to the right as the gap size progressively widens. With a rising distance, its corresponding capacitance C decreases, shifting resonance to the right.

2.4.1 Extraction of Equivalent Circuit Parameters

Obtaining commensurately appropriate L and C values for a specified configuration is necessary in order to accurately represent a defective ground structure (DGS) within a functional circuit framework. we created a model to extract parameters for a dumbbell-shaped DGS with a relative permittivity of 2.2 by positioning a 31 mil RT Duroid 5880 substrate under a 50 Ω microstrip line [1]. Figure 2.6 illustrates the expected transmission characteristics for a specific DGS design. It is noteworthy that the attenuation pole and the cut-off frequenc f_c occur at 8 GHz and 3.87 GHz, respectively.

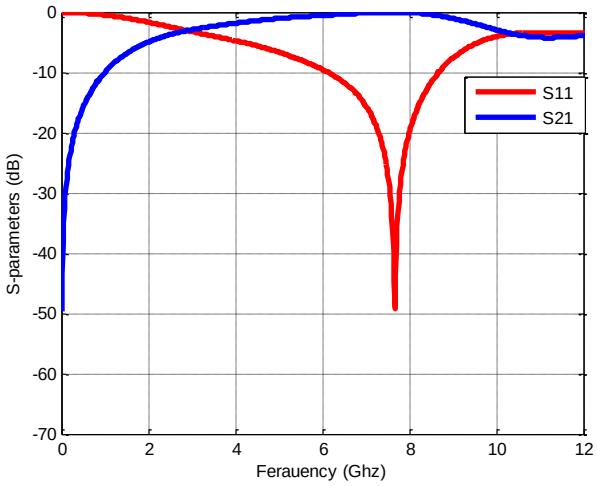

Figure 2.6: The 50 microstrip line's simulated S-parameters vs. frequency were integrated using dumbbell-shapedd DGS, where a = b = 5mmm and g = 0.5mmm. h = 31mmil for the substrate thickness and εr = 2.2 for the dielectric constant. Reproduced from Ahn et al. [1]

An expression for a parallel LC circuit's impedance is

$$Z_{LC} = \frac{Z_L Z_C}{Z_L + Z_C} = \frac{j\omega L}{1-\omega^2 LC} \tag{2.1}$$

and its resonance frequency as

$$\omega_0 = 2\pi f_0 = \frac{1}{\sqrt{LC}} \tag{2.2}$$

The reactance of this circuit is

$$X_{LC} = \frac{1}{\omega_0 C\left(\frac{\omega_0}{\omega} - \frac{\omega}{\omega_0}\right)} \tag{2.3}$$

In order to emulate a DGS with the response seen in Figure2.6, this LC circuit should function as a band-stop filter at resonance and an LPF (low-pass filter) at the cut-off. Thus, it is necessary to consider both behaviors in order to extract the values of L and C. First, a comparison is made between the reactance of the comparable circuit and a one-pole LPF of the Butterworth type that is running at the -3dB cut-off frequency. Next, the resonance frequency F_0 is equivalent to the attenuation pole. For handling a one-pole Butterworth-type LPF, one starts with an N-pole low-pass prototype filter. Figure 2.7 [2] shows this prototype form, which consists of normalized elements g1 through gn with the angular cut-off frequency set to unity.

$$g_i = 2sin\left(\frac{(2i-1)\pi}{2n}\right) \quad i = 1\ to\ n \tag{2.4}$$

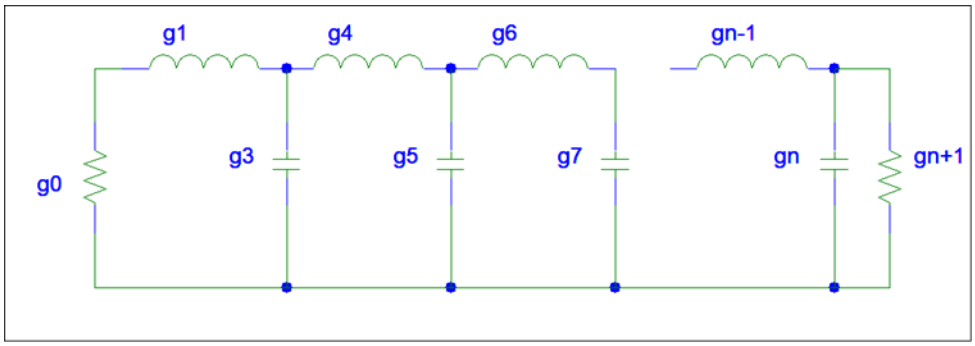

Figure 2.7: Prototype a lowpass filter for even n values using a ladder network. Based on a translation from Hong and Lancaster [2].

The load resistance and source resistance are both set to unity and are g_0 and g_{n+1}, respectively. One can use frequency and element transformations to obtain the elements for a specific frequency response [2]. Therefore, as seen in Figure 2.8, a one-pole filter consists of a single component, or g_1, as well as the load and source impedances, g_0 and g_2. The reactance of such a one-pole LPF is determined by impedance and frequency scaling.

$$X_{LB} = \frac{Z_0 g_1}{\omega_c}\omega = \omega' Z_0 g_1 \tag{2.5}$$

Where ω' is the normalizedangular frequency, ω_c is the cut-off angular frequency, and Z_0 is the impedance scaling to unite the source and load impedances.

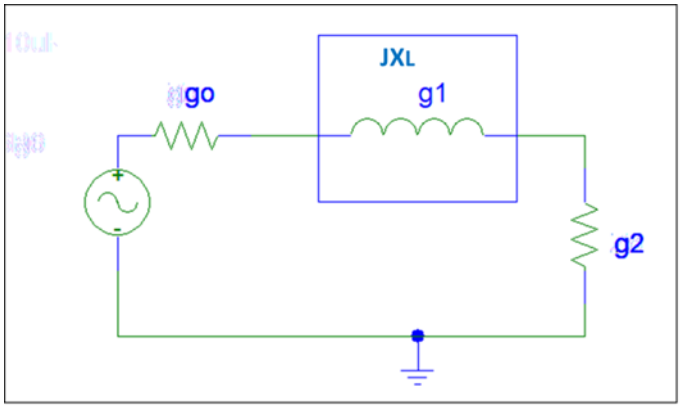

Figure 2.8: Prototype one-pole low-pass filter circuit

Reactance at the cut-off for a one-pole LPF should be as follows to match its response to the analogous circuit of our interest:

$$X_{LC}|_{\omega=\omega_c} = X_{LB}|_{\omega''=1} \tag{2.6}$$

leading to

$$\frac{1}{\omega_0 C\left(\frac{\omega_0}{\omega_c}-\frac{\omega_c}{\omega_0}\right)} = Z_0 g_1 \tag{2.7}$$

Or,

$$C = \frac{\omega_c}{Z_0 g_1(\omega_0^2-\omega_c^2)} \tag{2.8}$$

Equation (2.2), with the help of (2.9), yields

$$L = \frac{1}{4\pi^2 f_0^2 C} \tag{2.9}$$

Now, with Z0 = 50Ω and g_1 = 2 for a one-pole LPF, the corresponding values are

$$C = \frac{5f_c}{\pi(f_0^2 - f_c^2)} \tag{2.10}$$

$$L = \frac{250}{(\pi f_0)^2 C} \tag{2.11}$$

Given in GHz, the corresponding values are the cut-off frequency (f_c) and attenuation pole (f_0). Thus, the transmission characteristics of a certain DGS help in figuring out f_0 and fc, and thus the associated L and C values. From the examplein Figure2.6, where f_0 = 8GHz and fc = 3.87GHz, we can obtain equivalent L and C as 3.139nH and 0.126pF, $respectively, using the values from (2.10) and (2.11). Figure 2.9 displays the resulting equivalent circuit, while Figure 2.10 compares the circuit's S-parameter response to values generated via electromagnetic field simulation. The S-parameter answer demonstrates a strong degree of consensus. Table 2.1 presents the outcomes of this technique applied to several DGS dimensions.

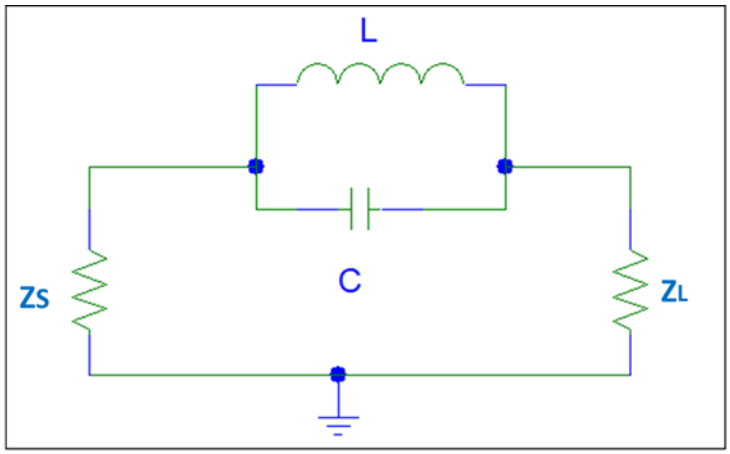

***Figure 2.9**:* The circuit equivalent for the dumbbell-shaped DGS with a width of 0.5mm, a length of 5mmm, and width of 5 mm is depicted in Figure 2.4a.

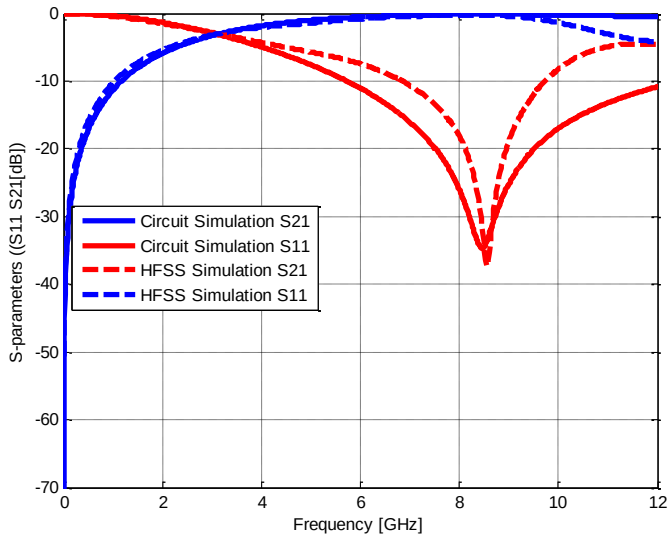

***Figure 2.10**:* Comparison of the extracted LC equivalent circuit's simulated S-parameters (Figure 2.9) with those of a DGS integrated 50Ω microstrip line (Figure 2.4(a)).

Table 2.1 lists the components and features of the analogous circuit shown in Figure 2.5for different DGS diameters fashioned like dumbbells.

Dimensions (mm) of a DGS in the form of a dumbbell						
equivalent circuit elementsand characteristics	g = 0.15			a = b = 2.5		
	A=b=2	A=b=3	A=b=4	g=0.1	g=0.3	g=0.5
Inductance measuredin nH	0.7056	1.2940	1.991	1.273	1.345	1.348
capacitance measuredin pF	0.5409	0.513	0.5155	0.5678	0.4124	0.3499
Cut-off frequency (fc) in GHz	6.81	4.82	3.66	4.59	5.1	5.4
Pole of attenuation f_0 (GHz)	8.15	6.18	4.97	5.77	6.76	7.33

2.4.2 Design of an N-Pole DGS Filter

We can now implement a more complex n-pole DGS filter solely through circuit simulations using the equivalent circuit extractedin Section2.2.1 as a "unit", eliminating the need for any EM-based complete wave analysis. We have shown a typical illustration of a three-pole LPF that is maximally flat and has a defined cutoff frequency of 2.3GHz. As previously mentioned, the prototype of this device comprises three components, g1, g2, and g3, as well as the source and load impedances, $g_0 = g_4 = 1$. Figure 2.11a shows the lumpedcircuit model based on the previously stated frequency scaling and impedance. Below resonance, the DGS in an analogous parallel LC circuit functions as an inductor.

$$L|_{f<f_0} = \frac{L_{eq}}{\left[1-\left(\frac{f}{f_0}\right)^2\right]} nH \tag{2.12}$$

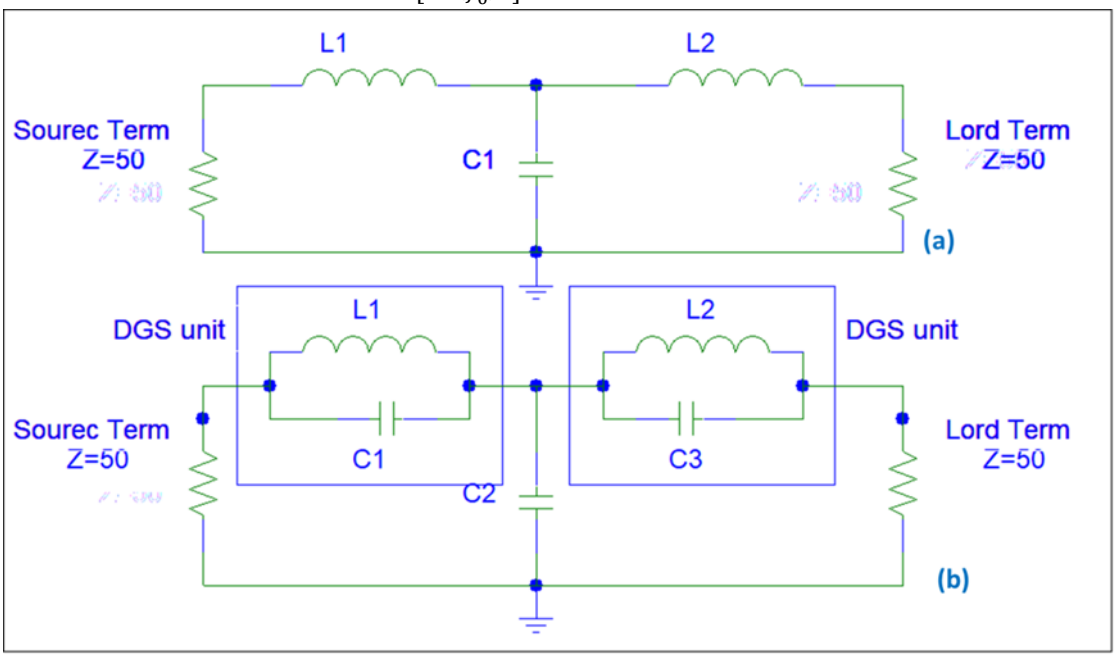

Figure 2.11(a) The schematic design shows a 3-pole Butterworth lowpass filter with a 2.3 GHz cut-off frequency that uses lumped circuit parts. (b) The circuit shown in (a) has been modified using a dumbbell DGS equivalent circuit. 2.3 GHz is the cut-off frequency, and the ripple is 0.01 dB. Origin: Taken from Ahn and colleagues [1].

It is possible to replace L_1 and L_2 in Figure 2.11a with an equivalent DGS since this inductance varie slowly as a function of frequency below the cut-off. Figure 2.11b provides further clarification on the situation. Figure 2.12a symbolizes a pair of DGS units connected in a series. The realization of the lumped capacitor C_2 in Figure 2.11b involves introducing an unfinished stub (Figure 2.12a). The corresponding computation uses Kuroda identities, and Richards transforms [2]. Figure 2.12b presents the LPF circuit's (Figure 2.11b) scattering qualities as determined by circuit modeling and is shown next to a comparable DGS design, Figure 2.12a. They have an excellent mutual understanding. Up to 8GHz, the LPF offers more than 20 dB of rejection. Comparing these DGS filters to a traditional LPF, the stopbands are broader and more profound. Creating a high-impedance inductance with a standard microstrip line is also extremely difficult because the line width is too narrow. However, the DGS filter makes it feasible.

(a)

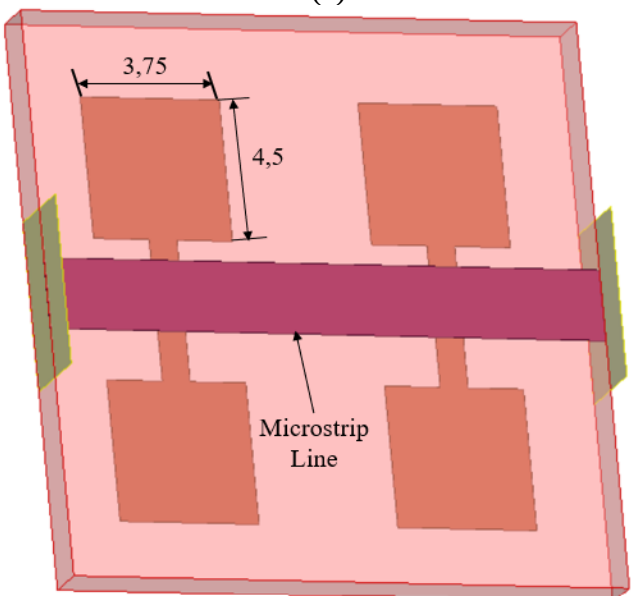

Figure2. 12: Realized lowpass filter with T-junction open stub (LT = 7mm, w =5 mm) and two unit cell DGSs. Parameters in line with Figure 2.5. Source: Taken from Ahn and colleagues [1].

(b)

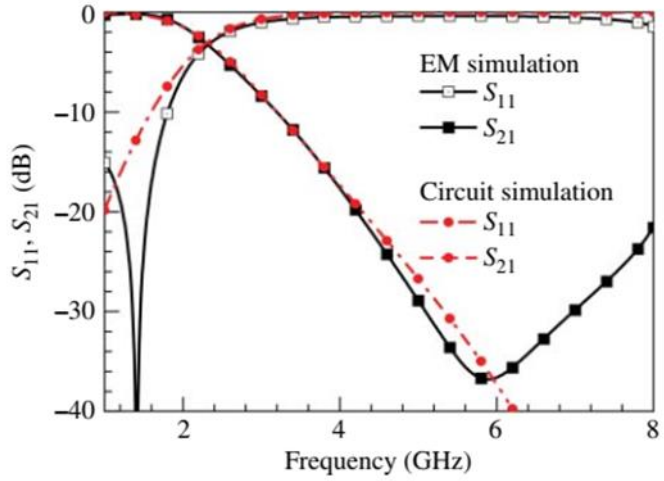

Figure 2.13Compares the simulated S-parameters from the comparable circuit (Figure 3.11b) with the printed DGS-integrated LPF (Figure 2.12). Figures 2.8 and 2.9 show the parameters, respectively

After extracting the LC equivalent of a simple DGS, it can be effectively employed in designing a higher-order filter and its DGS version without requiring time consuming iteration or trial and-error approaches using EM simulation.

2.4.3 Circuit Modeling for RLC Systems

Although an RF circuit clearly experiences radiation, leakage, and conductor/dielectric heating, the parallel LC circuit modeling of a DGS does not account forany losses. Figure 2.14 comparative analysis supports this. As seen in Figure 2.14a, a realistic model would thus include an analogous L and C connected in parallel to resistance R [3]. The transmission line equation [3] has this loss resistance R taken out as:

$$R = \frac{2Z_0}{\sqrt{\frac{1}{|S_{11}(\omega)|^2} - \left(2Z_0\left(\omega C - \frac{1}{\omega L}\right)\right)^2} - 1} \tag{2.13}$$

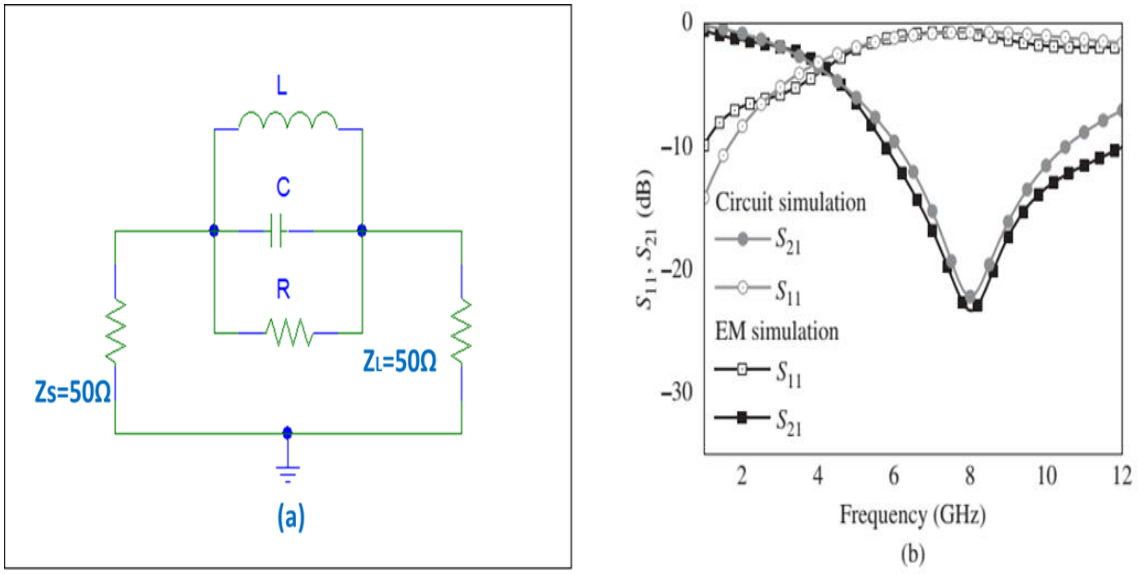

***Figure 2.14**:* For the shape like a DGS shown in Figure 2.12, with a = b = 5mm and g = 0.5mm, (a) the corresponding RLC circuit was extracted; (b) the circuit simulated S-parameters for the aforementioned RLC circuit were compared with the EM-simulated S-parameters for the DGS in Figure 2.12a

Worth

$$S_{11}(\omega) = \frac{Z_{in} - Z_0}{Z_{in} + Z_0} \tag{2.14}$$

With the provided attenuation pole and cut-off frequency values depicted in Figure2.7, the magnitude of$S_{11}(\omega)$ is calculated to be 0.9063. L and C values from (2.10) and (2.11) quickly assist in the computation of R = 1186.23Ω. Comparing Figure 2.14b to Figure 2.14a, the circuit simulation for the corresponding RLC circuit shows a considerably closer resemblance to the EM simulation.

2.5 Modeling LC Circuits: Modifications and Advancements

Researchers completed numerous additional studies on other DGS forms after successfully modeling the dumbbell-shaped DGS as circuits analogous to LC and RLC. During that procedure, researchers investigated specific novel variants to enhance the precision and clarify the characteristics of specific DGS shapes. This section covers a few of these crucial structures and the circuit representations that g_0 along with them.

2.5.1 Equivalent Circuit of Pi Type

Including more circuit segments has increased the RLC model's order of accuracy[4]. A couple of extra RC networks handle the bordering fields surrounding the step discontinuities in Figure 2.15, which illustrates one such situation. Figure 2.15 additionally includes parts of the transmission lines to account for the electrical length of the DGS. The values of the network

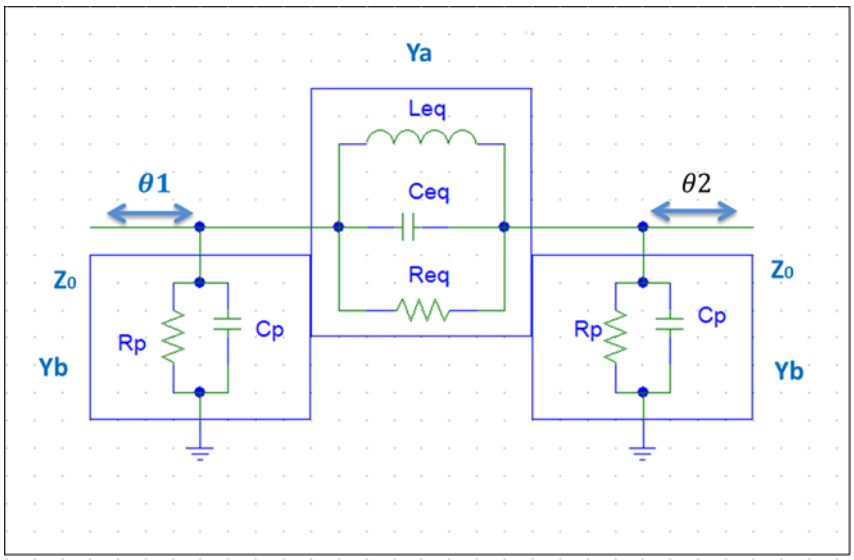

Figure2. 15: *Equivalent circuit of a Pi for a DGS with a single-cell dumbbell form. Source: Park et al. [4].*

To obtain the values of the DGS characteristics (S-parameter), we match them with the ABCD parameters [4]. These relationships are offered by:

$$A = \frac{(1+S_{11})(1-S_{22})+S_{12}S_{21}}{2S_{21}} \quad (2.15)$$

$$B = \frac{(1+S_{11})(1+S_{22})-S_{12}S_{21}}{2S_{21}} \quad (2.16)$$

$$C = \frac{1}{Z_0}\frac{(1-S_{11})(1-S_{22})-S_{12}S_{21}}{2S_{21}} \quad (2.17)$$

$$D = \frac{(1-S_{11})(1+S_{22})+S_{12}S_{21}}{2S_{21}} \quad (2.18)$$

For the Pi-type network, the ABCD parameters are often represented by the admittance values Y_a and Y_b, as shown in Figure2.15.

$$A = 1 + \frac{Y_b}{Y_a} \quad (2.19)$$

$$B = \frac{1}{Y_A} \quad (2.20)$$

$$C = 2Y_b + \frac{Y_b^2}{Y_a} \quad (2.21)$$

$$D = 1 + \frac{Y_b}{Y_a} \quad (2.19)$$

These two sets of formulas, 2.15–2.18 and 2.19–2.22, respectively, provide

$$Y_b = \frac{1}{B} = \frac{1}{R_{eq}} + jB_a \quad (2.22)$$

$$Y_b = \frac{A-1}{B} = \frac{D-1}{R_p} + jB_p \quad (2.23)$$

Whereas B_p represents the susceptance of the CR circuitry that corresponds to Y_b, B_a represents the susceptance of the LCR analog circuit equivalent to Y_a.

Equation(2.23) yields the equivalent capacitance with the aid of (2.2).

$$C_{eq} = \frac{B_a}{\omega_0\left(\frac{\omega_c}{\omega_0} - \frac{\omega_0}{\omega_c}\right)} \quad (2.24)$$

The resonance condition of (2.9) yields the corresponding inductance as

$$L_{eq} = \frac{1}{\omega_0^2 C_{eq}} \quad (2.25)$$

Utilizing the actual values of Y_a and Y_b, resistances compute R_{eq} and R_p and calculate capacitance C_p.

$$C_p = \frac{B_p}{\omega_c} \quad (2.26)$$

This document presents the equivalent circuit characteristics of the dumbbell-shaped DGS with identical dimensions and substrate specifications, as depicted in Figure2.4.Req = 2330Ω, Rp = 2560Ω, Leq = 3.43nH, Ceq = 0.116pF, and Cp = 0.36pF are the retrieved values for fc = 3.88GHz and f_0 = 8GHz. They respond in a way that is very similar to the EM-generated data, as shown in Figure 2.14, based on the circuit simulation. Compared to Figure 2.16, it offers a more significant agreement at the cut-off frequency. Furthermore, there is a more remarkable similarity than what a primary RLC circuit would have anticipated.

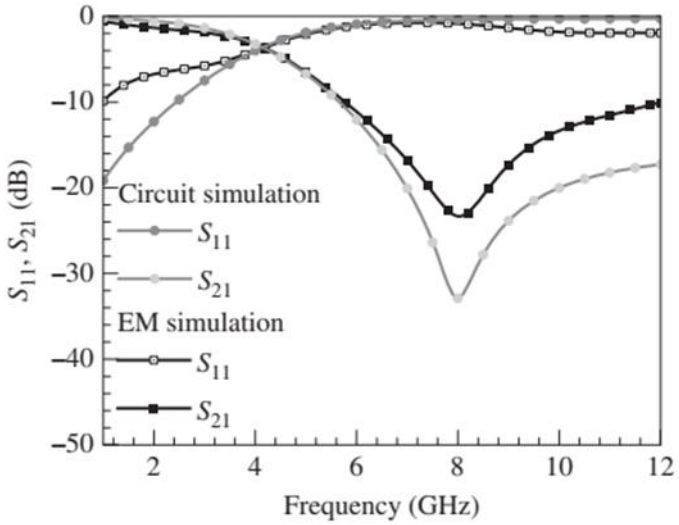

***Figure2. 16*:**The electromagnetic simulated curves for the distributed ground structure integrated 50Ω microstrip line, were juxtaposed with the circuit simulated S-parameters for the Pi equivalent circuit in Figure 2.15.

2.5.2DGS Modeling Using Aperiodic Stopbands

Aperiodic multiple stopbands are present in various additional geometries, in contrast to spiral DGS. The distance between the two stopbands may potentially be regulated by a few DGS geometrical factors. Figure 2.17 illustrates two instances of CPW and microstrip arrangements. The frequency up to the second stop band is carefully considered for the majority of their applications; Figure 2.18 showcases a typical response. For a transit frequency f_T, the first and double resonances are represented by frequencies f_{01} and f_{02}. The interaction between two consecutive periodic resonances and their effect on the transmission characteristics have been modeled in Figure2.19[8]. For the first and second resonances, two parallel LC resonators account for their behavior, while a T-network represents the interplay between these two resonators. Here, the analogous circuit characteristics have been retrieved using circuit theory using Z-parameter data derived from EM simulations, as opposed to a Butterworth prototype LPF .

$$C_i = \frac{1}{Z_0}\frac{1}{4\pi\Delta f_{3dB-i}} \tag{2.27}$$

$$L_i = \frac{1}{(2\pi f_{0i})^2 C_i} \; where\; i = 1,2 \tag{2.28}$$

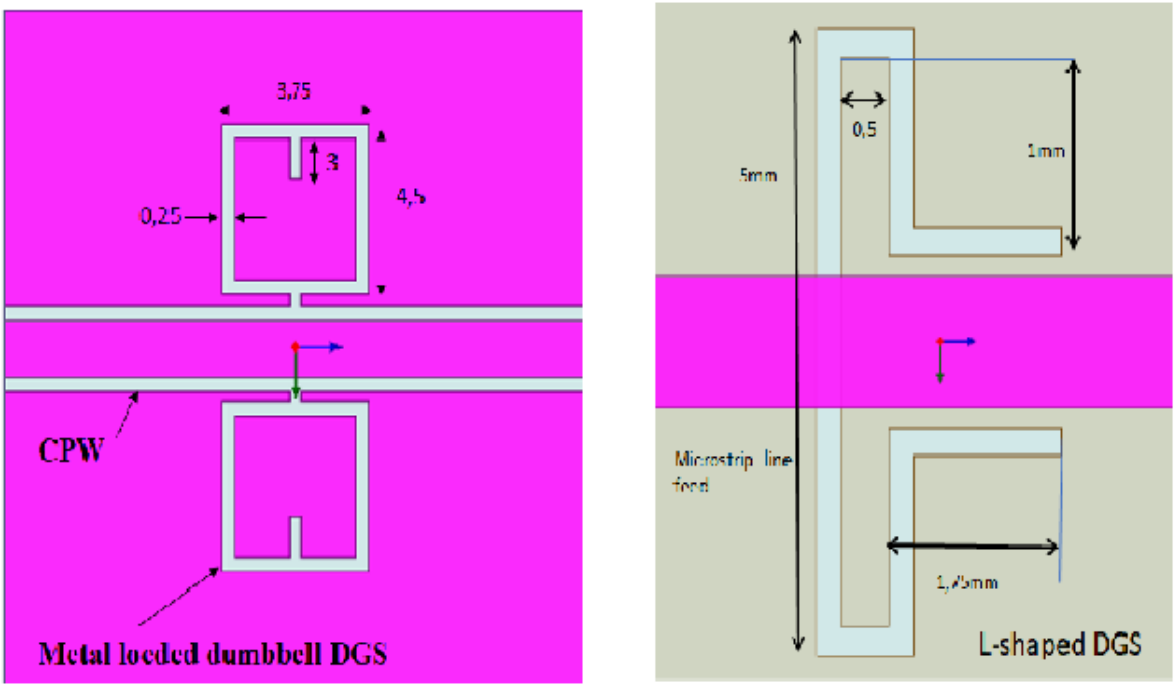

Figure 2.17: DGS geometries with different aperiodic stopband characteristics are presented in this study. These include an L-shaped DGS integrated with a 50Ω microstrip line and a 50Ω CPW integrated with a metal-loaded dumbbell DGS. The dielectric constant (εr) is 10.8, and all measurements are in millimeters, with the substrate having a a thickness of 1.27mm. This information has been adapted from the work of Hong and Karyamapudi ..

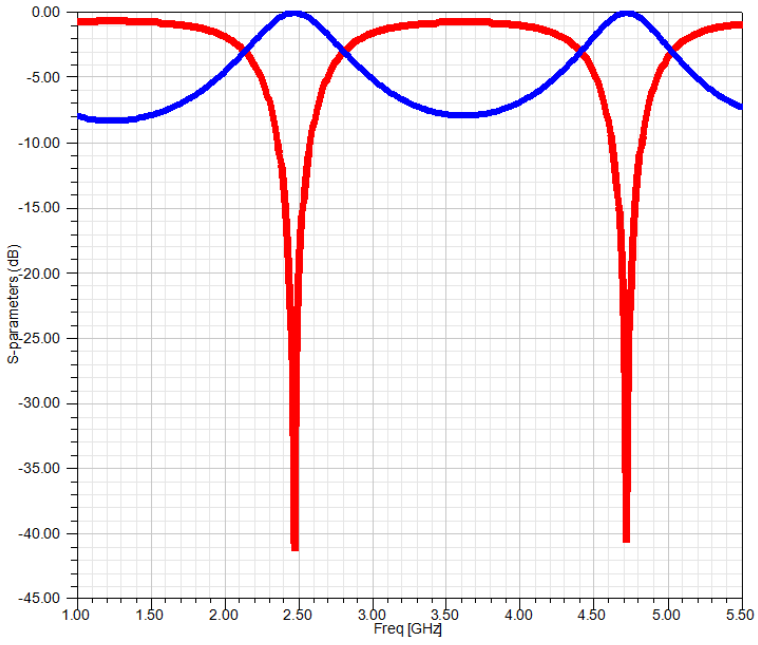

Figure 2.18: The multi-stopband DGS's typical response has two resonant frequencies, f_{01} and f_{02}, and a transition frequency, f_T. [8].

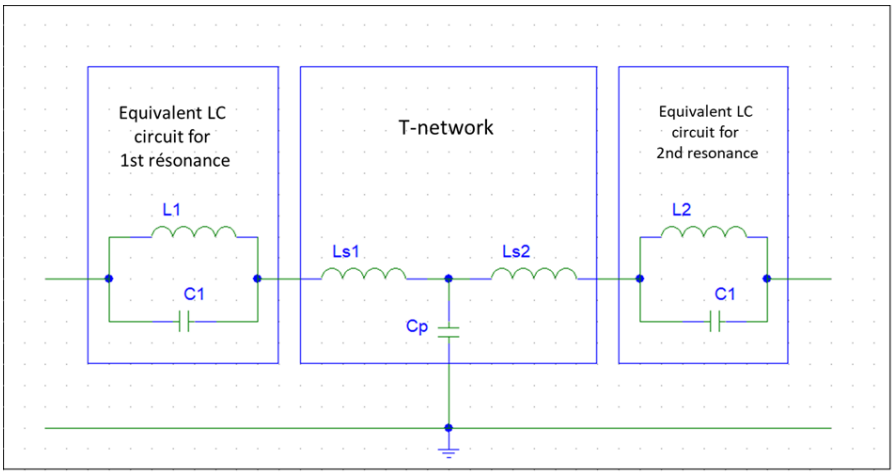

Figure 2.19: A DGS generic equivalent circuit model .

$$C_p = \frac{1}{2\pi f_T X_{21}} \tag{2.29}$$

$$L_{si} = \frac{X_{ii} - X_{21}}{2\pi f_T} + \frac{L_i}{\left(\frac{f_r}{f_{oi}}\right)^2 - 1} \; where \; i = 1; 2 \tag{2.30}$$

X_{11}, X_{22}, and X_{21} represent the imaginary component of the Z-parameter, and Δf_{3dB_1} and Δf_{3dB_2} are the 3 dB bandwidths for frequencies f_{01} and f_{02}. Using data from an electromagnetic simulation, we find the 3 dB bandwidth and resonance frequencies, f_{01} and f_{02}. The conventional S-to-Z-parameter conversion method yields equivalent Z-parameters [9]. It is now possible to extract the corresponding circuit parameters for each of the two geometries in Figure 2.19. They use a 50Ω line on dielectric substrates that are 1.27mm thick and have ε_r = 10.8. Table 2.2 provides the extracted values.

Table 2.2 Figure 2.19 displays the extracted parameters for the L-shaped DGS and the dumbbell loaded with metal.

the DGS extracted parameters							
DGS Type	L_1(nH)	C_1(pF)	L_2(nH)	C_2(pF)	L_{s1}(nH)	L_{s2}(nH)	C_p(pF)
Dumbbell loaded with metal	**1.226**	**0.89966**	**0.2212**	**0.632**	**0.995**	**-0.919**	**0.033**
L-shaped	**0.4184**	**1.349**	**0.082**	**1.02**	**-0.749**	**0.5745**	**0.028**

Table 2.2 shows intense reciprocal matches between the S_{11} and S_{21} characteristics derived from circuit simulations and the EM simulated curves in Figure 2.17.

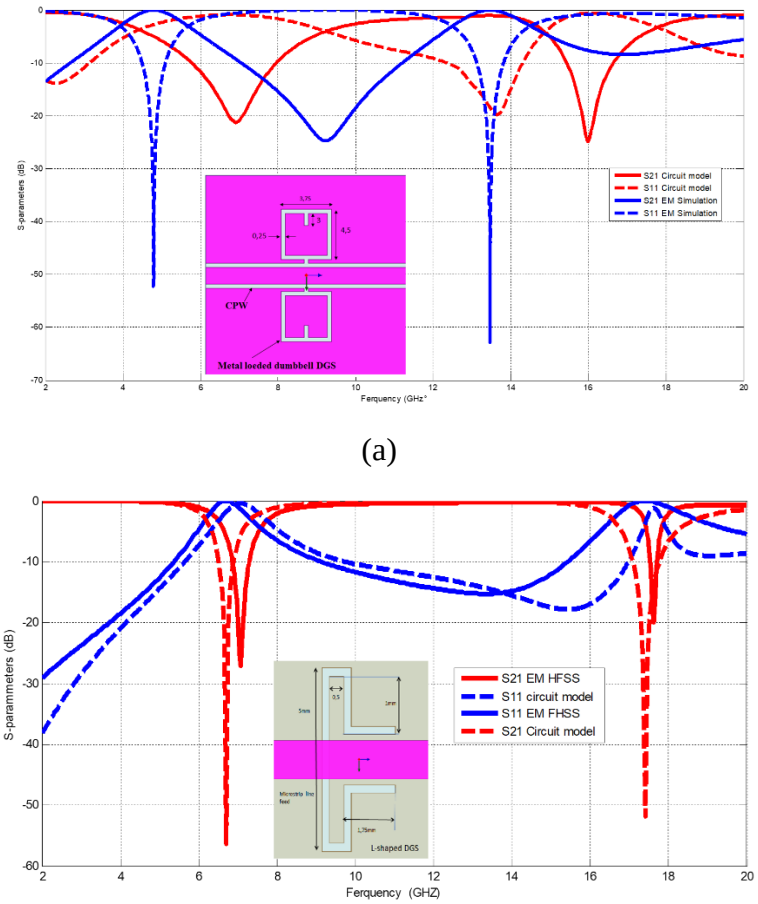

Figure 2.20:Comparing the S_{11} and S_{21} magnitudes for (a) metal-loaded DGS (Figure 2.17a) and (b) L-shaped DGS (Figure 2.17b) between circuit simulation and electromagnetic simulation. as shown in Figure 2.17 for parameters

2.5.3 A Few Changes to the Modeling Technique

Researchers have investigated several adjustments to a DGS's fundamental LC resonator circuit model over time. Their primary purpose is to handle a few specific DGS geometries. Figures 2.21 and 2.22 show two instances of this kind.

Figure 2.21[10]shows an interdigital geometry and its corresponding circuit. The circuit includes Lp from the defect itself and a series of combinations of L_s and C that make up the interdigital pattern[11]. Figure 2.21 shows the suggested equivalent circuit for an open square DGS [12]. The researchers show the DGS with a series of L_2C_2 combinations and a parallel LC resonator (L_1C_1) to consider how the microstrip line works[12]. Researchers use the connection between the ABCD parameters and the EM-simulated S-parameters to extract the equivalent circuit [9]. There are significant fringing field effects in the area of small gaps. Using L_3, L_4, L_5, and C_3 models, the T-network

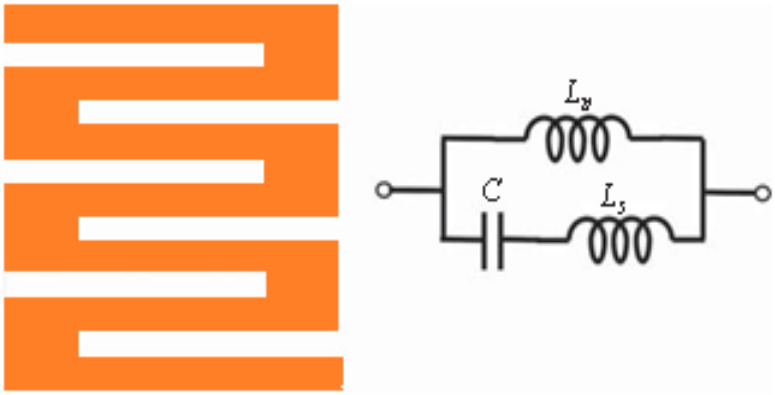

***Figure 2.21**:* A DGS with a inter digital form and its corresponding circuit. [10]

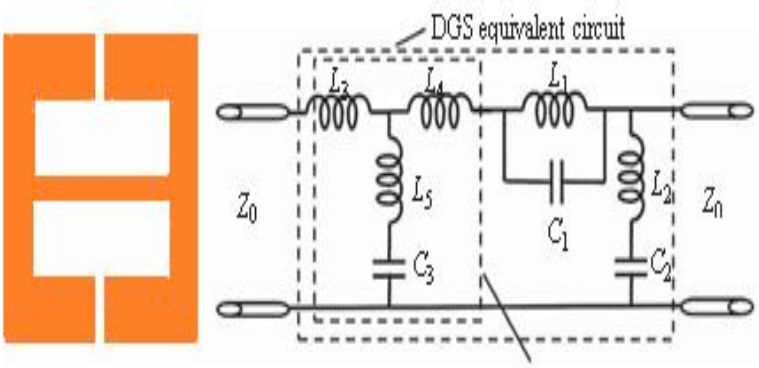

***Figure2. 22**:* The geometry of the open square DGS and its equivalent circuit [12].

2.6 Modeling Transmission Lines

The transmission line model of the DGS is based on a proposal from [13], and Figure 2.23 displays the schematic geometry. Two distinct frequencies cause the structure to resonate, and Figure 2.23 illustrates the ensuing magnetic fields around the slots to provide important context for understanding how the faults work. Whereas the second resonance frequency only allows the folded arms to work, the first resonance frequency activates the whole slot. It is thus possible for two different transmission lines at two different resonances to indicate the same problem. Figure 2.23a displays the input port position for the appropriate transmission line to be examined at first resonance on the plane of symmetry denoted as "1". Figure 2.24a displays the modeled three segments. It consists of two parallel, open-ended stubs similar to a transmission line. The input port for the second resonance is represented by the planeof symmetryin Figure2.23b, which is designated as "2." As a result, as shown in Figure 2.24b, one side arm has been modeled as an open-circuit transmission. The lengths of the relevant segments determine the resonance frequencies in Figure 2.24.

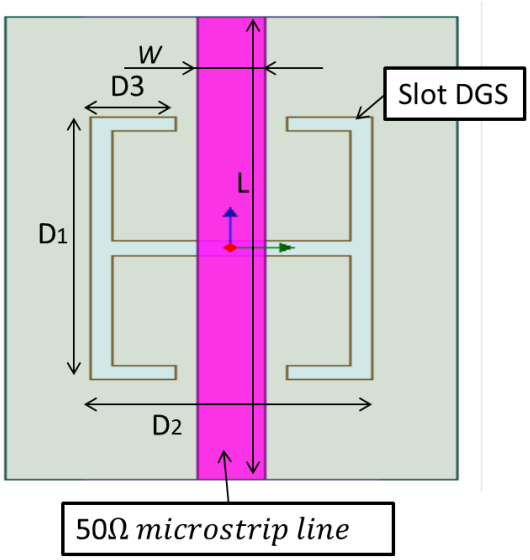

Figure 2.23: Diagrammatic geometry of a transmission line model-analyzed DGS. The following parameters are in millimeters: w = 0.635mm, L = 37.8mm, d_1 = 3.30mm, d_2 = 1.27mm, d_3 = 3.68, slot width = 0.254mm, substrate thickness = 0.635mm, εr = 10.2. [13]

Figure 2.23 illustrates the modeling of the same DGS using an analogous circuit. For the initial resonance, a parallel RLC circuit is responsible. Figure 2.23 depicts the second resonance as a series RLC circuit, while Figure 2.22 models it as an open-ended stub. We have derived the corresponding circuit parameters using the previously mentioned approach. Figure 2.26 displays the circuit simulations' response to the full-wave simulation data. Another transmission line model [14]describes how a DGS and a microstrip line couple. Figure 2.24a [14] illustrates the shape, which resonates at

$$f_m \cong m\frac{C_0}{2d\sqrt{\varepsilon_{eff}^{slot}}} \quad where\ m = 1,2,3 \ldots \tag{2.31}$$

The DGS traps the RF energy over the stopbands as usual. Figure 2.24b illustrates the suggested comparable circuit, which is somewhat different. It takes this into account.

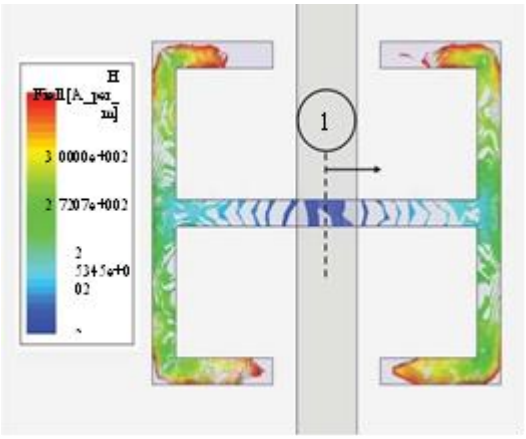

(a)

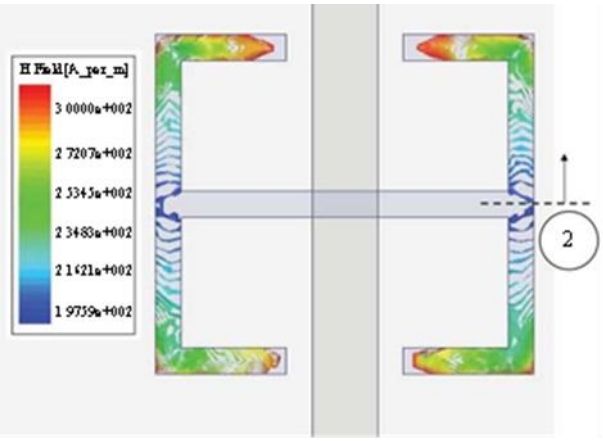

(b)

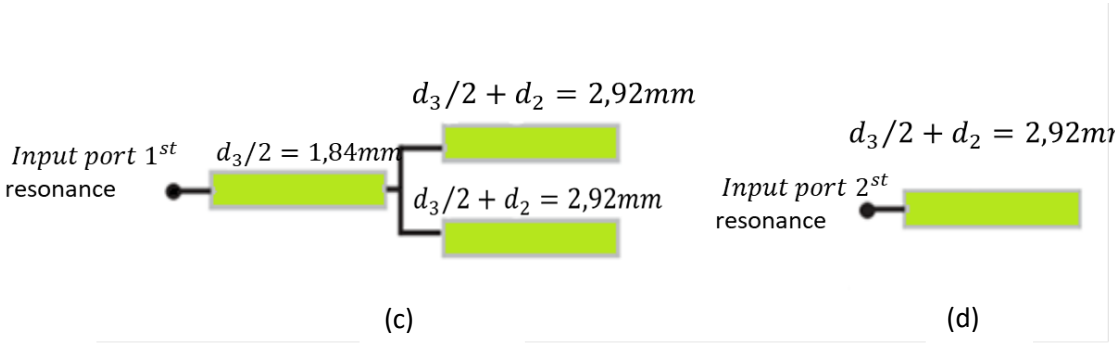

Figure2. 24:DGS transmission line model : (a) first resonance at 7.19GHz; (b) second resonance at 12.86GHz. Refer to Figure 2.23 for information on the input ports. [13].

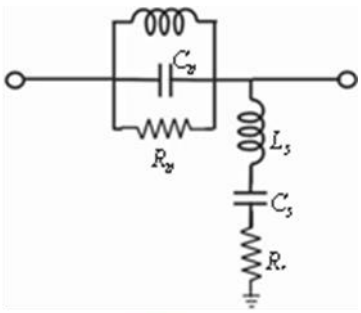

Figure 2. 25*:* shows the equivalent circuit of the DGS. The extracted parameters are as follows: Rs = 4.41Ω, Ls = 6.61nH, Cs = 23.16pF, Lp = 1.55nH, Cp = 0.315pF, Rp = 3125Ω. [13]

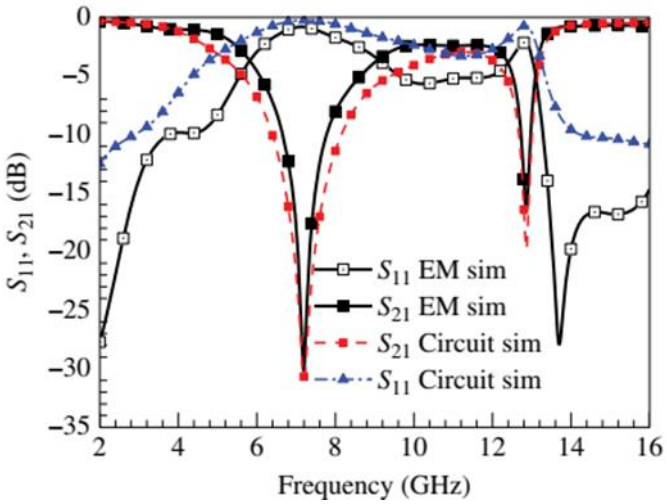

Figure 2.26*:* ameters for the comparable circuit in Figure 2.29 are compared with the EM simulated data for the DGS integrated line in Figure 2.29.[13]

There are N_s number of DGS slots, and each slot is represented as a transmission line with the electrical length $\theta=\theta_1+\theta_2=\beta_0^{slot}$d and characteristic impedance Z_0^{slot}. The position of the micro-strip line determines the input port's reference, and for a symmetrical deployment concerning slot width "d," this yields $\theta_1 = \theta_2$. The pairing of the microstrip line with the slots is shown by an

2.7 Modeling in Quasistatic

As shown in [15], this is a unique modeling strategy for a dumbbell DGS. The following discussions suggest how it differs from the ones mentioned in Sections 2.2–2.4. Utilizing the conventional design methodology:

The initial stage is setting the desired parameters (such as the operating frequency, Q-factor, stopband attenuation, and bandwidth).

Step 2: Determine the DGS geometry and approximate its dimensions roughly.

Step 3: Select an appropriate dielectric substrate for the application

Step 4: Create S-parameter characteristics by doing EM simulations.

Step 5: Determine whether you've achieved the required frequency response.

Step 6: Give up if you get the desired outcome. If not, alter the measurements and go to step 4. Continue doing this until you've achieved the objective.

Although it takes a lot of time, this iterative trial-and-error approach is the only one available since no relationship exists between a DGS electrical performance and physical dimensions.

A comparable LC circuit may represent the DGS design once it is complete. This form of modeling can derive the corresponding circuit characteristics by using a typical n-pole LPF prototype and some pre-knowledge obtained from the EM simulated data of the DGS under test. On the other hand, the quasistatic method extracts the circuit parameters straight from the DGS values by establishing a connection between the analogous circuits and DGS dimensions. As a result, the modeling is trustworthy and quick.

The dumbbell DGS was shown to have quasistatic modeling[15]. The quasi-TEM mode is known to propagate across a regular microstrip line by passing its return RF current via the ground plane. Current distribution is disrupted when a flaw is lodged in the ground plane. A crucial part of this research is examining the effective current path around the fault, which may be done using a commercial EM simulator, as Figure2.27 [15] illustrates.

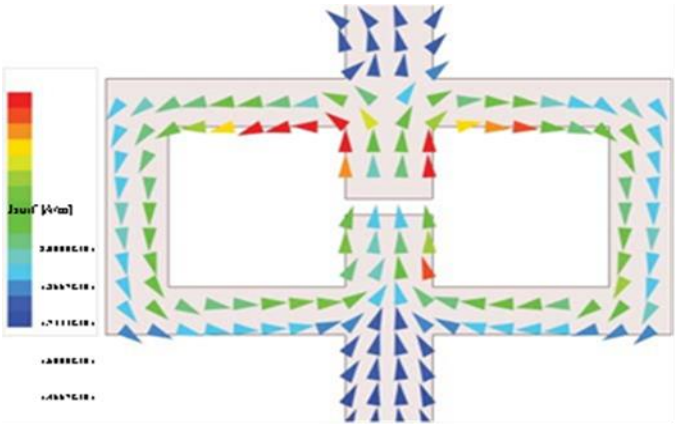

Figure 2.27*:* A commercial electromagnetic simulator determined the surface current distribution around the defect's perimeter. Source: Taken from Karmakar and colleagues [16]

Figure 2.28a shows the compact three-dimensional structure of a gap-coupled microstrip line. The current concentration zones help to portray a 2D comparable current ribbon model, as Figure 2.28b illustrates. Both two microstrip cross structures and a gap discontinuity are present. Their modeling, as shown here, is the next step.

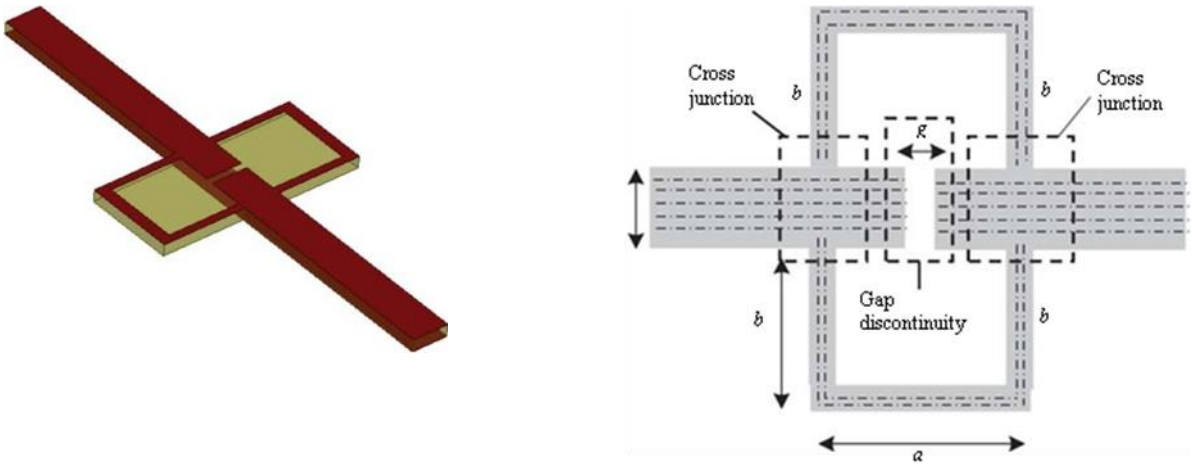

(a) (b)

***Figure 2.28**:* Dumbbell DGS modeling of a gap-coupled microstrip line: (a) comparable current ribbon; (b) three-dimensional perspective. Source: Taken from Karmakar and colleagues [16]

2.7.1 Model of Microstrip Gap

An equivalent circuit for a microstrip gap discontinuity, consisting of two parallel line capacitances, Cp, and a gap capacitance C , is shown in Figure 2.29a [15]. The odd and even mode capacitances[15], provide them with the following values:

$$\begin{cases} C_p = \frac{1}{2} C_{even} \\ C_{gap} = \frac{1}{2}\left(C_{odd} - \frac{1}{2} C_{even}\right) \end{cases} \quad (2.33)$$

$$\begin{cases} C_{odd}(pf) = Wx \left(\frac{S}{W}\right)^{m_0} e^{K_0} \\ C_{even}(pf) = Wx \left(\frac{S}{W}\right)^{m_e} e^{K_e} \end{cases} \quad (2.34)$$

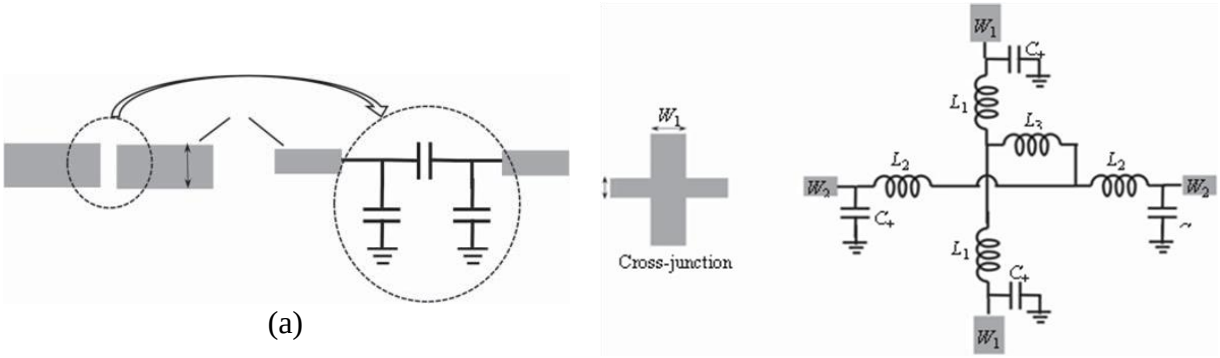

(a) (b)

Figure2. 29: For the portions seen in Figure 2.36, the circuits listed below are equivalent: (a) microstrip cross and (b) microstrip gap. Extracted from [16] Karmakar et al.

Al.
$$\begin{cases} m_0 = \frac{W}{h}\left(0.619 log \frac{W}{h} - 0.3853\right) \\ K_0 = 4.26 - 1.453 log \frac{W}{h} \end{cases} \quad for\ 0.1 \le \frac{S}{W} \le 0.3 \quad (2.35)$$

$$\begin{cases} m_e = 0.8675 \\ k_E = 2.043 \left(\frac{W}{h}\right)^{0.12} \end{cases} \quad for\ 0.1 \le \frac{S}{W} \le 0.3 \quad (2.36)$$

$$\begin{cases} m_e = \frac{1.565}{\left(\frac{W}{h}\right)^{0.16}} - 1 \\ K_e = 1.97 - \frac{0.03}{\frac{W}{h}} \end{cases} \quad for\ 0.3 \le \frac{S}{W} \le 1 \quad (2.37)$$

$$\begin{cases} C_{odd}(pf) = C_{odd}(9.6)\left(\frac{\varepsilon_r}{9.6}\right)^{0.8} \\ C_{even}(pf) = C_{even}(9.6)\left(\frac{\varepsilon_r}{9.6}\right)^{0.9} \end{cases} \quad (2.38)$$

where $\varepsilon_r = 9.6$, S = gap width, and W = microstrip line width

2.7.2 Model of Microstrip Cross Junction

In Figure 2.29b, the cross-connection shown in Figure 2.28b is represented as an LC combination. A series of relationships established in[17] are used to compute the inductance and capacitance values.

$$C_+(pF) = W_1\left\{\left(\frac{W_1}{H}\right)^{-\frac{1}{3}}\left[\left(86.6\frac{W_2}{h} - 30.9\sqrt{\frac{W_2}{h}} + 367\right) log\left(\frac{W_1}{h}\right) + \left(\frac{W_2}{h}\right)^3 + 74\frac{W_2}{h} + 130\right] - 1.5\frac{W_1}{h}\left(1 - \frac{W_2}{h}\right) + \frac{2h}{W_2} - 240\right\} \quad (2.39)$$

$$L_1 = L_2 = h\left(\frac{W_1}{h}\right)^{-\frac{3}{2}} \times \left[\frac{W_1}{h}\left(165.6\frac{W_2}{h} + 31.2\sqrt{\frac{W_2}{h}} - 11.8\left(\frac{W_2}{h}\right)^2\right) - 32\frac{W_2}{h} + 3\right] \quad (2.40)$$

$$L_3 = h\left[337.5 + \frac{h}{W_2}\left(1 + \frac{7h}{W_1}\right) - 5\frac{W_2}{h} cos\left(\frac{\pi}{2}\left(1.5 - \frac{W_1}{h}\right)\right)\right] \quad (2.41)$$

Where W_1 and W_2 stand for the microstrip line widths, and h is the thickness.

2.8 Conclusion

This chapter comprehensively overviews Defected Ground Structure (DGS) units and their applications within electronic circuit design. The discussion commences by introducing the fundamental concept and significance of DGS units, followed by a detailed analysis of their frequency responses. Various modeling approaches are then explored, encompassing the extraction of equivalent circuit parameters, the design intricacies of N-pole DGS filters, and modeling considerations for RLC systems. Furthermore, the chapter delves into modeling LC circuits, emphasizing enhancements and alterations within the field. Transmission line modeling and quasistatic methodologies, such as microstrip lines, microstrip cross-junctions, and rest current pathways, are also scrutinized. An examination of isolated DGS application modeling is included, culminating in reflections on the diverse modeling methodologies discussed. Lastly, a reference section is included to facilitate additional reading and in-depth exploration of the topics addressed in this chapter.

2.9 References

[1] A. Fernández-Prieto, "Defected Ground Structure (DGS) Based Antennas: Design Physics, Engineering, and Applications [Book Review]," *IEEE Antennas and Propagation Magazine*, vol. 66, no. 1, pp. 96-98, 2024.

[2] D. Ahn, J.-S. Park, C.-S. Kim, J. Kim, Y. Qian, and T. Itoh, "A design of the low-pass filter using the novel microstrip defected ground structure," *IEEE transactions on microwave theory and techniques*, vol. 49, no. 1, pp. 86-93, 2001.

[3] J.-S. G. Hong and M. J. Lancaster, *Microstrip filters for RF/microwave applications*. John Wiley & Sons, 2004.

[4] I. Chang and B. Lee, "Design of defected ground structures for harmonic control of active microstrip antenna," in *IEEE Antennas and Propagation Society International Symposium (IEEE Cat. No. 02CH37313)*, 2002, vol. 2: IEEE, pp. 852-855.

[5] J.-S. Park, J.-H. Kim, J.-H. Lee, S.-H. Kim, and S.-H. Myung, "A novel equivalent circuit and modeling method for defected ground structure and its application to optimization of a DGS lowpass filter," in *2002 IEEE MTT-S International Microwave Symposium Digest (Cat. No. 02CH37278)*, 2002, vol. 1: IEEE, pp. 417-420.

[6] C.-S. Kim, J.-S. Lim, S. Nam, K.-Y. Kang, and D. Ahn, "Equivalent circuit modelling of spiral defected ground structure for microstrip line," *Electronics Letters*, vol. 38, no. 19, p. 1, 2002.

[7] C.-S. Kim *et al.*, "The equivalent circuit modeling of defected ground structure with spiral shape," in *2002 IEEE MTT-S International Microwave Symposium Digest (Cat. No. 02CH37278)*, 2002, vol. 3: IEEE, pp. 2125-2128.

[8] M. Makimoto and S. Yamashita, "Bandpass filters using parallel coupled stripline stepped impedance resonators," *IEEE Transactions on microwave theory and techniques*, vol. 28, no. 12, pp. 1413-1417, 1980.

[9] J.-S. Hong and B. M. Karyamapudi, "A general circuit model for defected ground structures in planar transmission lines," *IEEE microwave and wireless components letters*, vol. 15, no. 10, pp. 706-708, 2005.

[10] D. A. Frickey, "Conversions between S, Z, Y, H, ABCD, and T parameters which are valid for complex source and load impedances," *IEEE Transactions on microwave theory and techniques*, vol. 42, no. 2, pp. 205-211, 1994.

[11] A. Balalem, A. R. Ali, J. Machac, and A. Omar, "Quasi-elliptic microstrip low-pass filters using an interdigital DGS slot," *IEEE Microwave and wireless Components letters*, vol. 17, no. 8, pp. 586-588, 2007.

[12] R. Wyndrum, "Microwave filters, impedance-matching networks, and coupling structures," *Proceedings of the IEEE*, vol. 53, no. 7, pp. 766-766, 1965.

[13] J.-X. Chen, J.-L. Li, K.-C. Wan, and Q. Xue, "Compact quasi-elliptic function filter based on defected ground structure," *IEE Proceedings-Microwaves, Antennas and Propagation*, vol. 153, no. 4, pp. 320-324, 2006.

[14] C.-C. Chang, C. Caloz, and T. Itoh, "Analysis of a compact slot resonator in the ground plane for microstrip structures," in *APMC 2001. 2001 Asia-Pacific Microwave Conference (Cat. No. 01TH8577)*, 2001, vol. 3: IEEE, pp. 1100-1103.

[15] C. Caloz, H. Okabe, T. Iwai, and T. Itoh, "A simple and accurate model for microstrip structures with slotted ground plane," *IEEE Microwave and Wireless Components Letters*, vol. 14, no. 3, pp. 127-129, 2004.

[16] N. C. Karmakar, S. M. Roy, and I. Balbin, "Quasi-static modeling of defected ground structure," *IEEE Transactions on Microwave Theory and Techniques*, vol. 54, no. 5, pp. 2160-2168, 2006.
[17] R. Garg and I. Bahl, "Microstrip discontinuities," *International Journal of Electronics Theoretical and Experimental*, vol. 45, no. 1, pp. 81-87, 1978.
[18] E. J. Denlinger, "A frequency dependent solution for microstrip transmission lines," *IEEE transactions on microwave theory and techniques*, vol. 19, no. 1, pp. 30-39, 1971.
[19] A. Gopinath and P. Silvester, "Calculation of inductance of finite-length strips and its variation with frequency," *IEEE Transactions on Microwave Theory and Techniques*, vol. 21, no. 6, pp. 380-386, 1973.
[20] F. W. Grover, *Inductance Calculations, Working Formulas and Tables: By Frederick W. Grover*. 1962.
[21] B. Easter, "The equivalent circuit of some microstrip discontinuities," *IEEE Transactions on Microwave Theory and Techniques*, vol. 23, no. 8, pp. 655-660, 1975.

CHAPTER 3 :

Substrat Integrated Waveguide (SIW)

3.1 Introduction

The Substrate Integrated Waveguide (SIW) technique for building waveguides—which direct electromagnetic waves from one place to another—is covered in this chapter. The intricate design of millimeter-wave and microwave circuits and systems requires the integration of antennas, transmission lines, active devices, and passive parts. To maximize their performance, manufacturers usually fabricate these components individually via a variety of manufacturing procedures. There are several techniques for fabricating millimeter-wave and microwave components.

Microstrip lines and coplanar waveguides are two examples of printed planar technologies that are widely used to create passive parts, interconnects, and antennas that operate in the microwave frequency range[1].These technologies use economical procedures to produce lightweight, low-profile, and compact components. However, printed components are prone to radiation leakage and undesired coupling between neighboring pieces, and they often suffer large losses, particularly at millimeter-wave frequencies. They are also not very good at managing electricity.

However, applications requiring total shielding and low losses often choose metallic waveguide technology. Metallic waveguides are appropriate for highly selective filters and high-power applications because they have low losses and high-quality factors. But they take a lot of time, money, and effort to make, and they are heavy and large.

It may be challenging to integrate parts from several fabrication processes into a system. Well-designed transitions are necessary when combining components from several technologies, and they may result in more losses, less operating bandwidth, and higher packaging costs.

In order to overcome the drawbacks of planar and metallic waveguide technologies, we have created a substrate-integrated waveguide, or SIW. Utilising conventional rectangular waveguides in a flat shape is made feasible by SIW technology. This offers several advantages, such as producing lightweight, compact components at a low cost using well-known techniques like printed circuit boards, high quality, high power handling, and electromagnetic wave blocking. With the use of SIW technology, a whole system may be integrated into a single substrate, doing away with the requirement for component transitions and lowering parasitics and losses. Moreover, coplanar waveguides and microstrip lines may be connected to SIW circuits with ease on the same substrate.

Microstrip lines and coplanar waveguides are two examples of printed planar technologies that are widely used to create passive parts, interconnects, and antennas that operate in the microwave frequency range. These technologies use economical procedures to produce lightweight, low-profile[1], and compact components. However, printed components are prone to radiation leakage and undesired coupling between neighboring pieces, and they often suffer large losses, particularly at millimeter-wave frequencies. They are also not very good at managing electricity.

In contrast, applications needing full shielding and low losses should favor metallic waveguide technology. Metallic waveguides are appropriate for highly selective filters and high-power applications because they have low losses and high-quality factors. But they take a lot of time, money, and effort to make, and they are heavy and large.

It may be challenging to integrate parts from several fabrication processes into a system. Well-designed transitions are necessary when combining components from several technologies, and they may result in more losses, less operating bandwidth, and higher packaging costs.

In order to overcome the drawbacks of planar and metallic waveguide technologies, we have created a substrate-integrated waveguide, or SIW. SIW technology

3.2 History

Since the early 1990s, numerous efforts have been made to develop planar waveguide structures. The earliest documented reference is a Japanese patent in 1994, which introduced a novel dielectric-charged waveguide consisting of two rows of metal vias within a dielectric substrate[2]. Following this, in 1995, an American patent proposed a waveguide utilizing a Low-Temperature Co-fired Ceramics (LTCC) process, also known as multilayer dielectric structures [3], as depicted in Figure 4.1

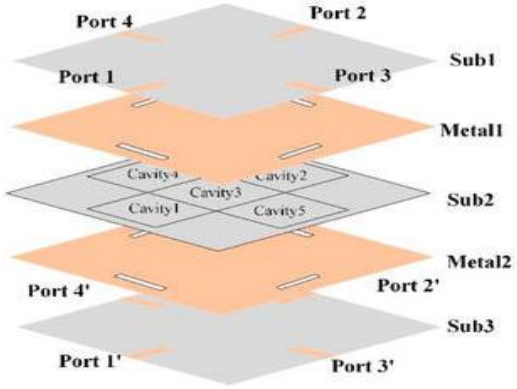

Figure 1:*The multilayer structure*

In 1997, the first application of Substrate Integrated Waveguide (SIW) technology emerged for antennas, marking a significant milestone. This was followed by studies focusing on millimeter waves and other related areas. Subsequently, SIW components were utilized in Low-Temperature Co-fired Ceramics (LTCC). Since the early 2000s, a research team led by Professor Ke Wu at the Poly-Grames Research Center, Polytechnic School of Montreal, has extensively explored SIW technology and component integration. A notable development occurred in 2001, where the transition from microstrip line to SIW topology was documented and became the standard for SIW circuit excitations[4].

SIW technology has been adopted for most microwave electronic functions, including various planar transitions, filters, couplers, duplexers, hexapoles, circulators, and antennas. Due to its ease of integration, SIW technology has also enabled the implementation of several active functions, such as oscillators, mixers, and amplifiers[5].

3.3 Definition of SIW technology:

SIW technology is a technology that, as its name suggests, allows the integration of a waveguide of a volume technology in a dielectric substrate of a technology planar. As the dielectric substrate of planar technology is metallized by planes of mass on the lower and upper walls, to arrive at a waveguide of classic volume technology, the conductive side walls of the latter will be replaced by rows of metal vias (metallic cylindrical rods), which will act as reflective walls during the propagation of the EM wave inside this guide, and Thus, the SIW technology will be created, which combines the advantages of both technologies. previous ones. The dimensions of the vias integrated into the substrate will represent parameters. important for the design of a structure based on SIW technology.

Technology traditional, whether planar or not, is incapable of providing all the characteristics to the times when we don't know what we're talking about: low cost and low losses. Waveguides rectangular have low losses but are expensive to manufacture, and their integration is difficult. With planar circuits[6]. Planar circuits have a low quality factor[6]. but negligible weight and low manufacturing costs. These antagonistic constraints have led to the use of SIW technology in order to combine the respective advantages of technologies mentioned previously. This concept combines the use of production technology[6].

planar with that of guide type, cavity... These structures can be produced by processes. classic planers (PCB, LTCC, etc.). Technically, the waveguides are buried in the substrate. The side faces are replaced by rows of metallized holes, which connect the upper and lower faces of the substrate, as shown in Figure 3.2.

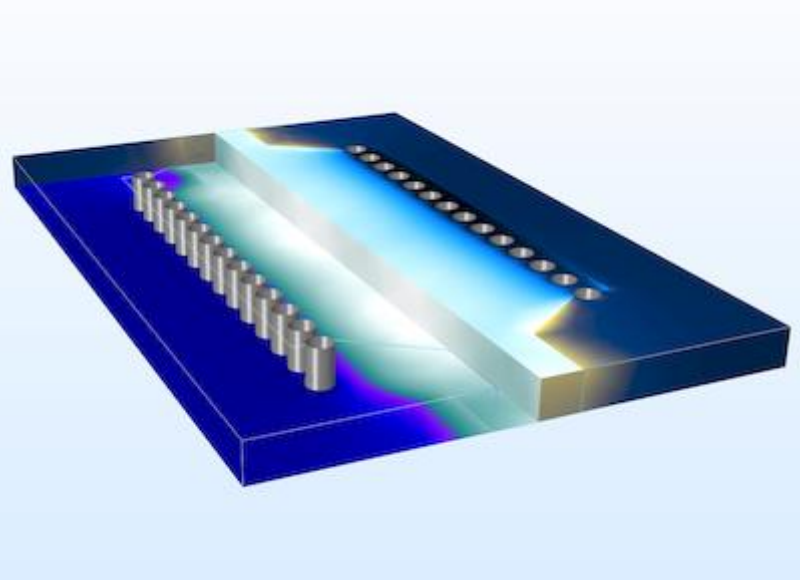

Figure 3.2 : *Topology of a SIW guide.*

3.4 Geometry SIW and Design Equations

Figure 3.3presents the structure of the substrate-integrated waveguide transmission line[7]. This physical geometry indicates that the SIW is formed by inserting a dielectric substrate between two opposite metal plates. The side walls of the SIW structure are achieved using two lines of regular metallic vias positioned adjacent to the lengths of the substrate, equivalent to the metal sidewalls of the conventional waveguide[7].

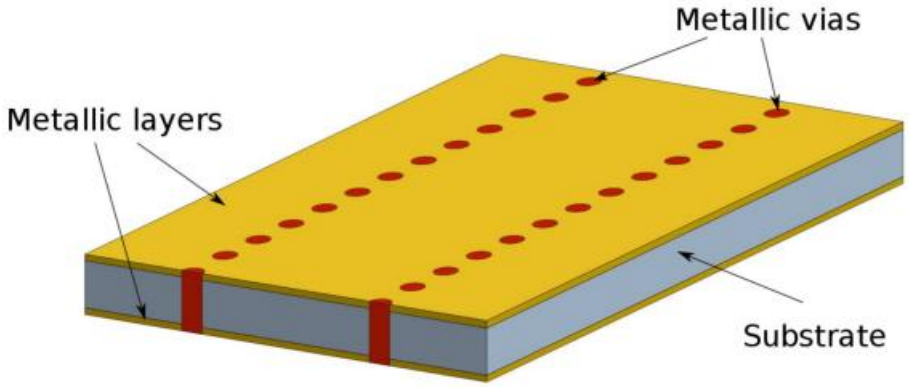

Figure 3.3 *:Physical structure of the substrate-integrated waveguide transmits*

The foundational principles of an SIW design are established by examining the correlation between the dimensions and b of a dielectric-filled waveguide (DFWG) and an air-filled waveguide (*fc*). As illustrated in Figure 3.3, the cut-off for an AFWG

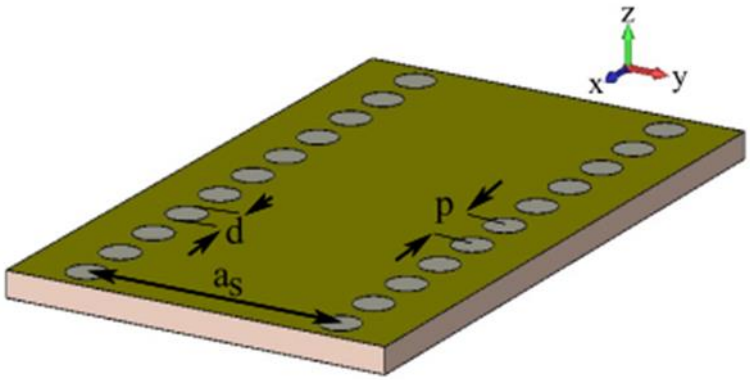

Figure 3.4:*SIW Geometry for Substrate Integrated Waveguide Testing [8]****.***

Frequency of a mode is given by:

$$f_c = \frac{c}{2\pi}\sqrt{\left(\frac{m\pi}{a}\right)^2 + \left(\frac{n\pi}{b}\right)^2} \qquad (3.1)$$

Where:

c: speed of light

m, n: mode numbers

a, b: dimensions of the waveguide

For TE_{10}mode, the much-simplified version of this formula is:

$$f_c = \frac{c}{2\pi} \tag{3.2}$$

For yang AFWG.

For DFW with the same cut-off frequency, the dimension "ad" is found by:

$$a_d = \frac{a}{\sqrt{\varepsilon_r}} \tag{3.3}$$

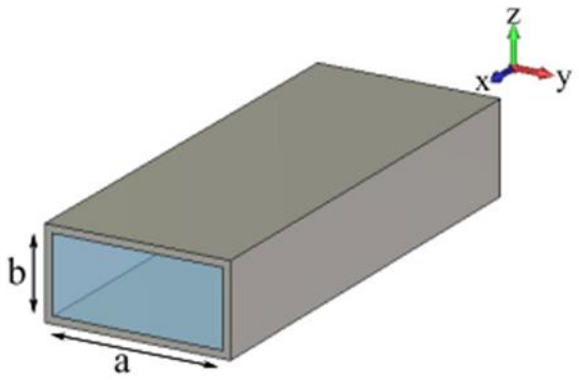

Figure 3.5:*Waveguides typically have rectangular perimeters*

One can achieve an equivalent fc (i.e., for the dominant TE_{10} mode) for a DFWG by substituting a with ϵr, which represents the relative dielectric constant of the dielectric that lines the waveguide. The initial empirical design equation for an SIW establishes a relationship between its width and the dominant TE10 mode of the SIW, denoted as fc, as specified in [8].

$$a_s = a_d + \frac{d^2}{0.96p} \tag{3.4}$$

As illustrated in Figure 3.6, whereas represents the width of the DFWG that corresponds to the same f_c, d denotes the diameter of the vias, and *p* signifies the center-to-center separation between the vias along the longitudinal axis. [8] A general guideline for determining *d* and *p* can be found in (3.5) and (3.6), respectively.

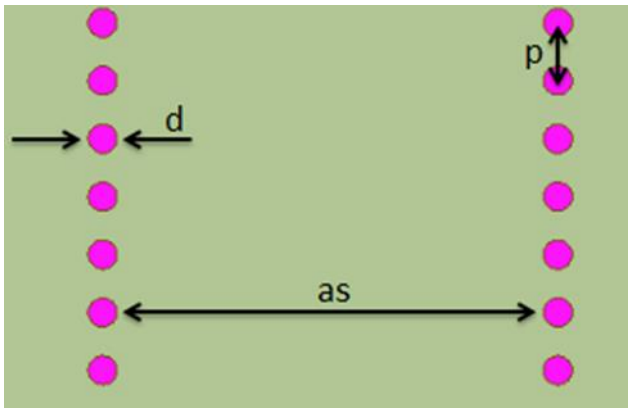

Figure 3.6:*Dimensions of SIW*

$$d < \lambda g/5 \quad (3.5)$$

$$p < 2d \quad (3.6)$$

where λg is the guided wave length [17] and is given by.

$$\lambda_g = \frac{2\pi}{\sqrt{\left(\frac{\varepsilon_r(2\pi f)^2}{c^2}\right) - \left(\frac{\pi}{a}\right)^2}} \quad (3.7)$$

It should be noted that the design equations remain unaffected by the thickness of the substrate. However, the loss of the structure is influenced by the thickness, and thus, the low-loss advantage associated with a thick substrate should be considered.

On possible interpretation of equations (3.5) and (3.6) is that the efficacy of a SIW is influenced by the pitch length, p, for a fixed via diameter, d. Using HFSS, we simulate the S-parameters (S_{11}andS_{21}) of the geometry depicted in Figure. 3.6 to examine the transmission and reflection characteristics of an SIW structure as p values vary. To stimulate the SIW geometry as a DFW, the input and output terminals of the HFSS are represented by rectangular vias. Employing rectangular vias to stimulate the SIW geometry as a DFW diminishes the likelihood of encountering meshing errors in the simulator that arise from circular vias at the ports. Rogers3003, which has a loss tangent of 0.0013, a thickness of 10 mil, and ε_r = 3, is extensively employed in industry as the substrate. Copper conductors measuring 0.7 microns in thickness are utilized.

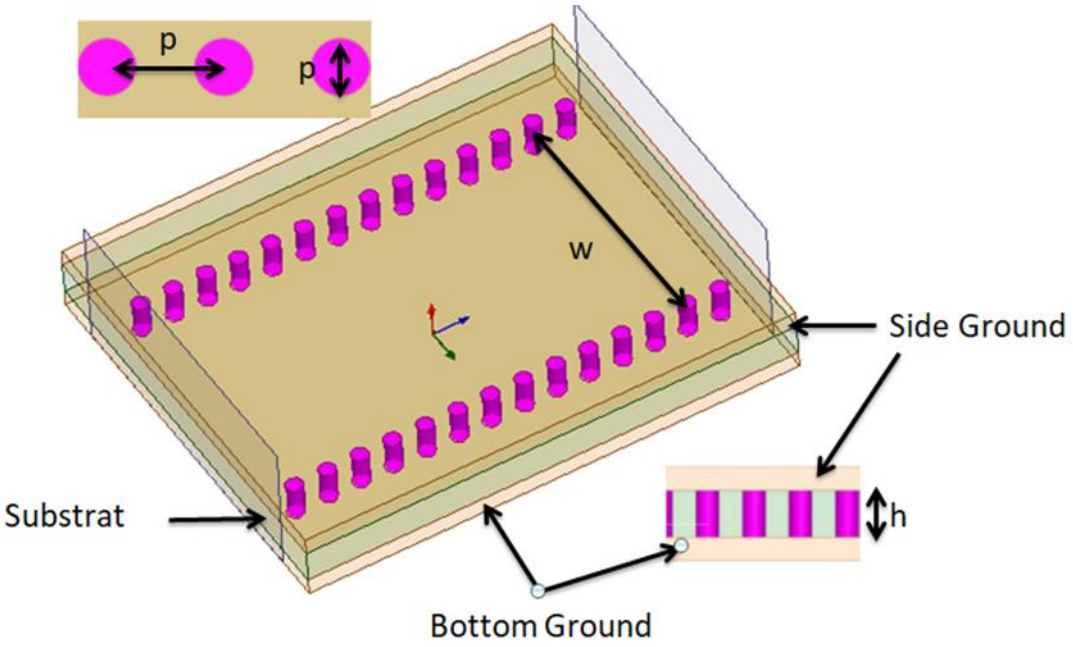

Figure 3.7:*Geometry of SIW for testing*

The SIW structure has been purposefully engineered to operate within the Ka-band frequency range of 6–17GHz. λg = 4.5466 mm at this frequency; consequently, the utmost d is 0.909mm, as calculated in (4.4). As a result, we established d = 0.508mm, which is one of the conventional via diameters. We then manipulate the pitch length, p. Notwithstanding this, we recalculate the SIW's width from (3.3) for each p in order to guarantee that the SIW is designed appropriately. We consistently determine the SIW to have a length of 25,4mm.. We conduct simulations utilizing HFSS, as previously stated. S_{11} versus the frequency of the designed SIW along the Ka-band for various p values (p = 0.508, 0.762, 1.016, and 1.27mm) is depicted in Figure 3.6. Figure 3.7 depicts the [9]S_{21} versus frequency for the identical design and variations [8]. Equation (3.6) specifies that the upper limit for the p value is 1.016mm. The effect of selecting larger values (p = 1.27mm) on the efficacy of the design is assessed. The S-parameter results indicate that as p increases in length, there is a corresponding rise in return loss (S_{11}), with the highest return loss value dropping from -30 dB to -17dB.

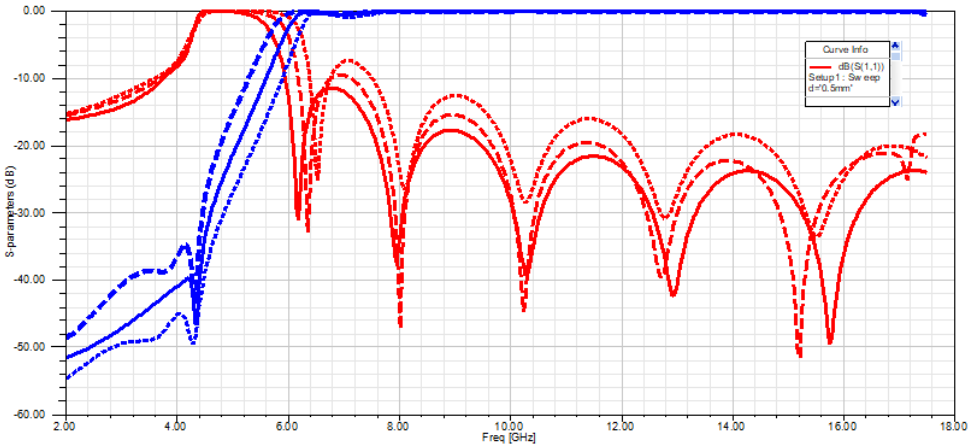

***Figure 3.8**: S_{11} results for d=0.508mm.and p=0.508, 0.762, 0.016 , and 1.27mm*

For the geometry illustrated in Figure. 3.7

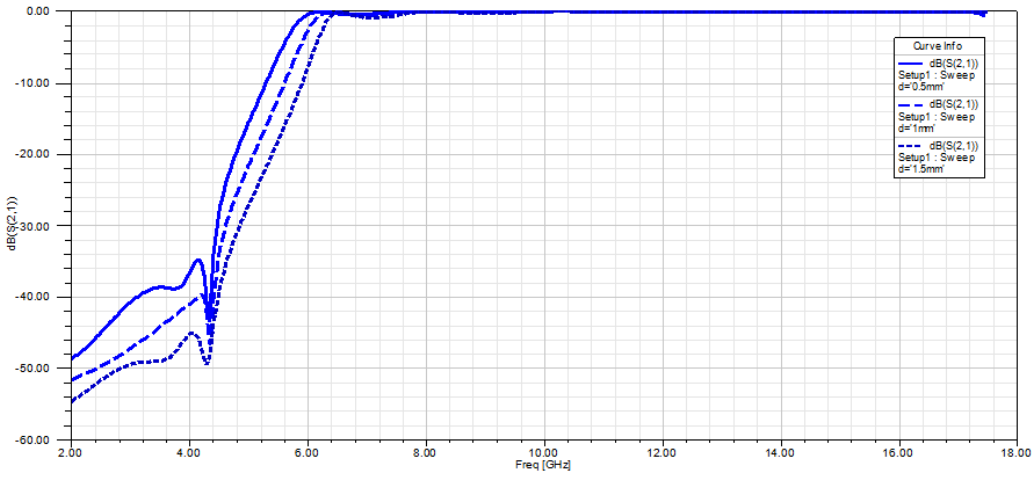

***Figure 3.9:** S_{21} results for d=0.508mm and p=0.508, 0.76, 1.016, and 1.27mm for the geometry illustrated in Figure. 3.7*

The increase in insertion loss and the emergence of oscillations (refer to Figure 3.9) in the frequency band are caused by a rise in RF leakage between the vias.

Upon examination of the outcomes illustrated in Figures3.8 and 3.9, it becomes evident that the design equations provided in equations (3.5) and (3.7) function satisfactorily. Nevertheless, a more practical approach to SIW design entails employing them as initial design equations, which can be refined for optimization. SIW provides greater latitude for determining the cut-off frequency than conventional waveguides.

Finally, we investigate thee operating frequency of SIW in the X-band. We implemented the architecture shown in Figure 3.7. This design utilizes a 0.635mm-thick Rogers TMM10issubstrateewith ε_r= 9.8, a loss tangent of 0.002, and am thickness of ρ_r = 9.8. The critical SIW parameters and dimensions for the design are p = 0.71mm, d = 0.4mm, and as = 7.54mm.

When all modes are accounted for in the simulations, TE_{20}, which is comparable to an AFWG, is the next higher mode after the prevalent TE_{10}emode. As demonstrated in Figure 4.6, the TE_{10}mode X-bandcut-off frequency for the SIW is approximately 6.7 GHz, followed by a cut-off frequency of 13.4 GHz, roughly double the frequency above. As with AFWG, TE_{20}moderepresents the subsequent highe mode of SIW. Consequently, the operational frequency ranges of conventional AFWG (provided in Appendix A) also apply to SIW structures.

3.5 Transitions to Other Guiding Structures

All transitions are matched for both broad and narrow bands through the integration of SIW with waveguides and printed structures. This section delivers detailed explanations of the transitions that are frequently utilized, including the microstrip to SIW transition, grounded coplanar waveguide, and rectangular waveguide.

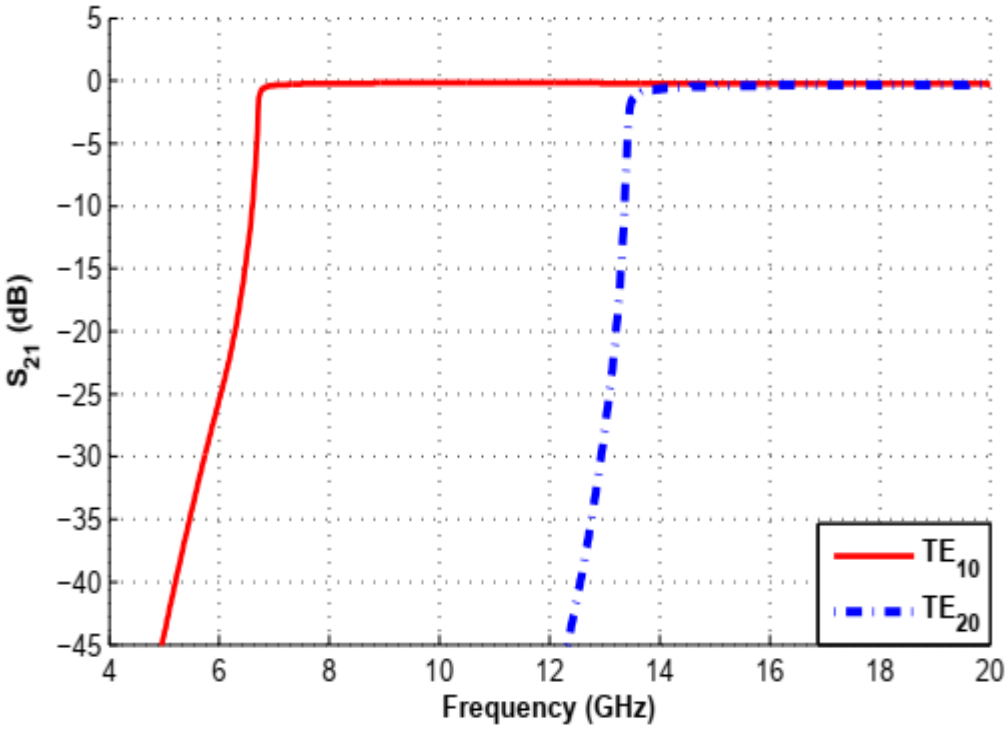

Figure 3.10: *SimulatedeS$_{21}$ results for TE_{10} and TE_{20} modes*

3.5.1 Microstrip to SIW Transition

As illustrated in Figure 3.11, the tapered microstrip transition is generally preferred for joining microstrip structures to SIW. Broadband synchronization is typically achieved compared to alternative printed transitions [11]. However, due to the lengthy wavelength vat low frequencies, the taper length may be relatively long. As a result, may consider alternative transition topologies for low-frequency applications.

As both the substrate and the frequency band are extensively utilized in microwave applications, we opted for Rogers 5880 with a thickness of 0.254mm, σr = 2.2, and a loss tangent of 0.0009 at the Ka-band to design a microstrip to SIW transition. The designed SIW has a center-to-center width of 5.02mm. We determined the via diameter (d) to be 0.406mm and established the pitch length (p) at 0.7112mm. The dimensions in question conform to the SIW design equations provided in (3.3)–(3.5). Using optimization, we determined the taper width (wt) to be 1.651mm and the taper length (lt) to be 5.08 mm to attain matching at the Ka-band (see Figure 3.11).

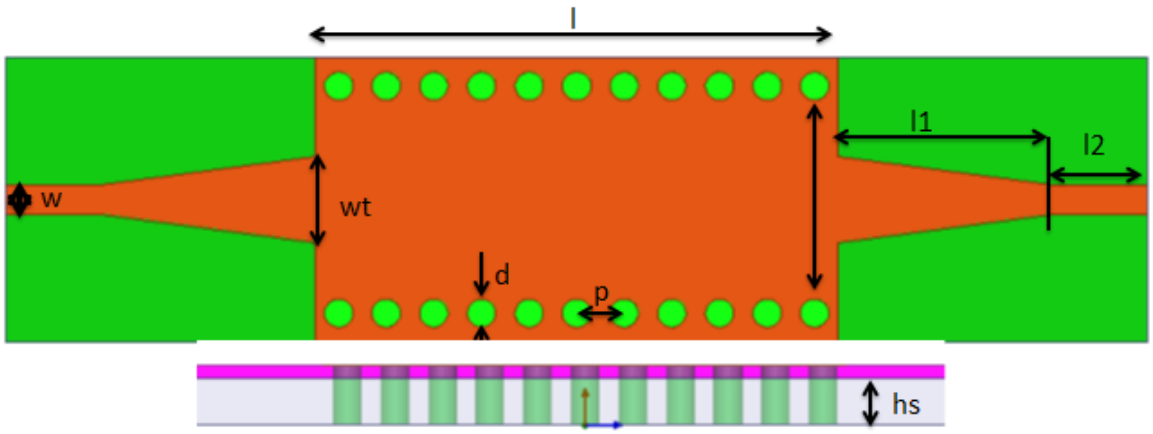

***Figure 3.11**: Microstrip to SIW tapered transition*

For this transition, the simulation results are depicted in Figure 3.11. Broadband matching (S_{11} is less than -15dB across the entire frequencyband) is achieved, as evidenced by the results; insertion loss is primarily attributable to dielectric and conductor losses due to the shallow reflection. The transition loss is predominantly influenced by the substrate and conductor materials selected [8].

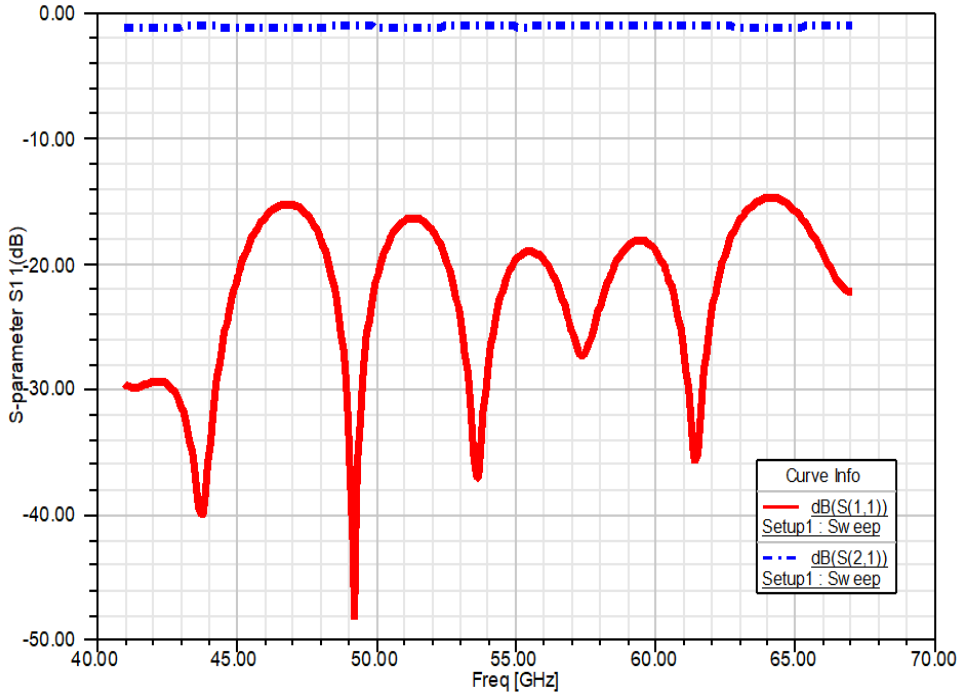

Figure 3.12: *Simulation results of the microstrip to SIW tapered transition*

For predetermined characteristic impedance, the breadth of the microstrip line is determined by the taper parameters, which must be adjusted when the thickness of the substrates altered.

3.5.2 CPW to SIW Transitions

In many situations, coplanar waveguides (CPW) are favored over microstrip lines, especially when integrated with substrate-integrated waveguide (SIW) structures on thick substrates, which help reduce conductor loss but cause large radiation leakage in microstrip lines. CPW, however, is compatible with thick substrates and can be optimized for various thicknesses. Various CPW-to-SIW transition designs have been proposed, the most common involving a 90° slot bend inside the SIW structure, though it can cause spurious radiation. A modified transition with an SIW cavity around the bent slots offers wideband performance, achieving 40% bandwidth with low return and insertion loss at 50 GHz. Another transition for grounded CPW uses a current probe to match the SIW mode. Generally, CPW-to-SIW transitions have lower bandwidth performance compared to microstrip-to-SIW transitions, with conductor-backed CPW offering better performance and wider bandwidth coverage.

3.6 Analysis Techniques of SIW

Various modeling techniques have been employed or custom-developed for the examination of Substrate Integrated Waveguide (SIW) structures, whether for simple interconnects or intricate components.

For the former scenario, the objective of the analysis is to determine the propagation and attenuation characteristics of the SIW modes across varying frequencies, along with identifying the modal field distribution of the fundamental mode and potentially of the subsequent higher modes. Conversely, in the latter scenario, the analysis aims to offer insights into the frequency behavior of the SIW component.

3.6.1 Rectangular Waveguide Equivalent

Substrate Integrated Waveguide (SIW) structures may be modeled most simply and effectively by resembling rectangular waveguides.

The SIW structure may be approximated by an analogous rectangular waveguide of suitable width since the dispersion properties of SIW modes are the same as those of regular rectangular waveguide modes [9].

The width of the analogous rectangular waveguide and the geometrical dimensions of the SIW may be analytically related.

We presented the first and most popular connection in [9]. The effective width, $weff$. The corresponding rectangular waveguide may be calculated using an empirical formula.

We proposed the first and most popular relationship in [9]. Using an empirical equation based on its effective width, we may find a comparable rectangular waveguide.

(a)

(b)

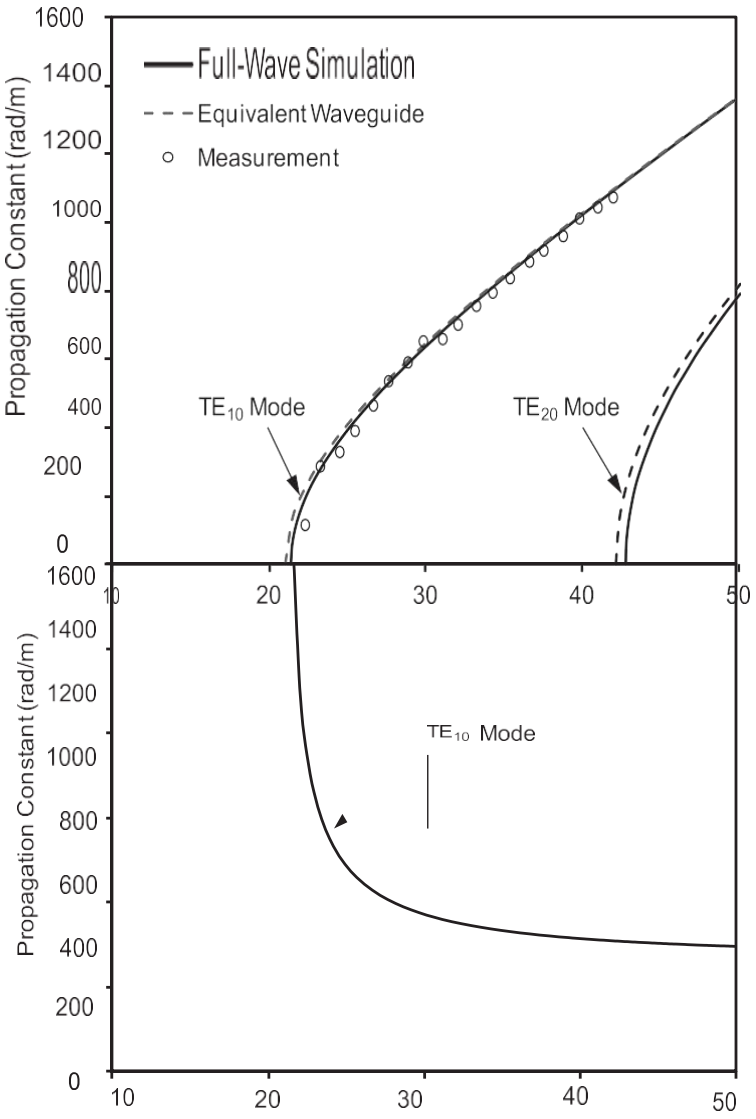

***Figure 3.13**: Below is an example of the SIW modes' dispersion curves.*

(a) Full-wave simulation results are shown as a solid line, the comparable waveguide model is a dashed line, and measurements from reference [9] are indicated by dots.

(b) The wave impedance formulae of the analogous rectangular waveguide, as mentioned in reference [8], are used to compute the characteristic impedance of the basic SIW mode

3.6.2 Full-Wave Electromagnetic Modeling of SIW Interconnects

A more precise characterization of SIW interconnects can be achieved through full-wave electromagnetic modelling. This comprehensive analysis provides a detailed understanding of straight SIW interconnects

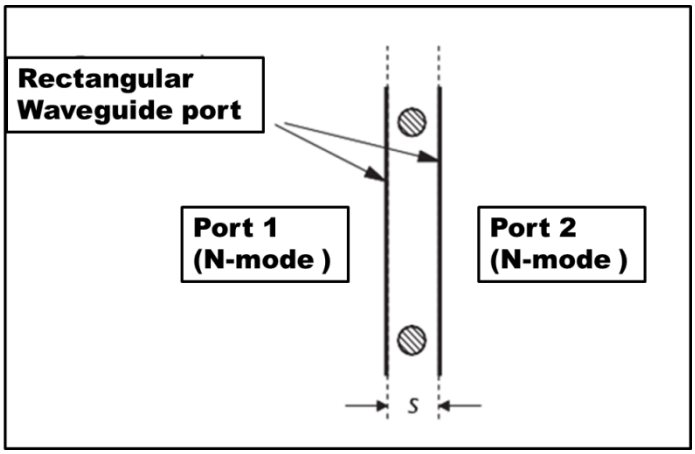

(a)

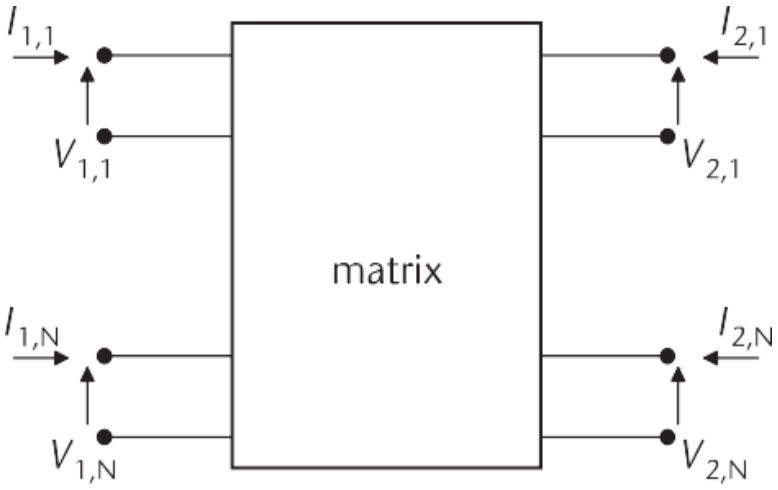

‘(b)

***Figure 3.14**: Two aspects of the SIW structure topology employed in formulating the eigenvalue issue are (a) the unit cell geometry and (b) the ABCD matrix definition.*

Finding the field pattern of the SIW modes and the curves for propagation and attenuation constants vs frequency are the main objectives. Since SIW interconnects are usually modelled utilizing the periodicity of the structure, a unit cell of the periodic structure, rather than a segment of the waveguide, may be taken into account (Figure 3.14).

By using the Floquet-Bloch theorem, analysis methods that use unit cell models may drastically cut down on computing expenses.

- Three primary types of analytic methodologies may be distinguished when modelling SIW interconnects:
- techniques using full waves that express a classical eigenvalue issue [9],.The issue is formulated in terms of a transcendental equation using integral equation methods [2].
- The surface impedance idea serves as the foundation for the analytical techniques [7], [15].

3.6.3 Whole-Wave Simulation of SIW Elements

Substrate Integrated Waveguide (SIW) component full-wave modelling is essential to the development of SIW technology. The critical importance that accurate and adaptable electromagnetic simulators play in optimising the capabilities and versatility of SIW technology cannot be overstated. Consequently, in addition to employing commercial full-wave electromagnetic solvers, we have created specific numerical simulation tools to characterise and design SIW components, with an emphasis on the computation of their scattering or admittance matrices.

3.6.4 Equivalent Circuits Models of SIW Discontinuities

Due to their increased complexity and long processing times, comparative circuit models are a powerful design tool for SIW components, especially in large circuits. This method, rooted in research by Nathan Marcuvitz in the 1940s, breaks down complex circuits into simple building components, reducing computing load and ensuring frequency response.

Simple SIW breaks, such as iris windows, waveguide sections, and waveguide bends, can be the fundamental building blocks for passive SIW parts. These basic building pieces are characterized by equivalent circuit models, which include perfect waveguide sections, resistors, capacitors, and inductors. However, the method used to derive these models is crucial for the quality of results. Accurate models can be produced through full-wave analyses and fitting or processing findings. Parametric equivalent circuit models are also necessary for SIW component design and optimization.

The application of the BI-RME approach is the main topic of this section [10]. The generalized admittance matrix Y of the building block is provided by the BI-RME approach as a pole expansion in the frequency domain, as was covered in the previous section.

$$Y_{ij}(\omega) = \frac{A_{ij}}{j\omega} + j\omega B_{ij} + j\omega^3 \sum_{m=1}^{M} \frac{C_{im}C_{jm}}{\omega_m^2(\omega_m^2 - \omega^2)} \qquad (3.8)$$

Where M is the number of cavity resonances produced by short-circuiting the building block's ports, and i, j, and refer to the port modes. The BI-RME approach calculates the frequency-independent values A_{ij}, B_{ij}, C_{im}, and ω_m relatively efficiently [11].

Yij's equation is recast in the form based on the extraction of the term for ω→∞ from the summation in (3.8).

$$Y_{ij}(\omega) = \frac{1}{j\omega}A_{ij} + j\omega\left(B_{ij} - \sum_{m=1}^{M}\frac{C_{im}C_{jm}}{\omega_m^2}\right) + j\omega\sum_{m=1}^{M}\frac{C_{im}C_{jm}}{(\omega_m^2 - \omega^2)} \qquad (3.9)$$

This expression can be easily identified as the parallel combination of inductor , capacitor, and *M* LC-series resonators (Figure 3.15(a)). The value of the lumped elementsappearinginFigure3.15(a)are directly obtained from expression(3.9)as

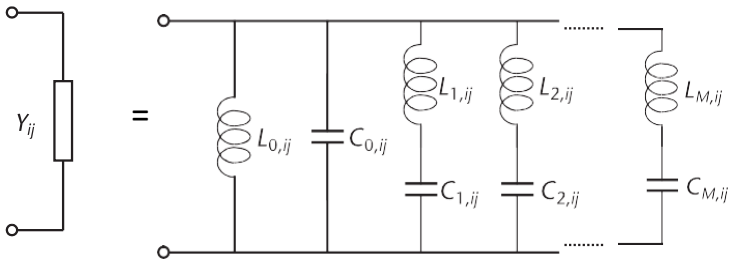

(a)

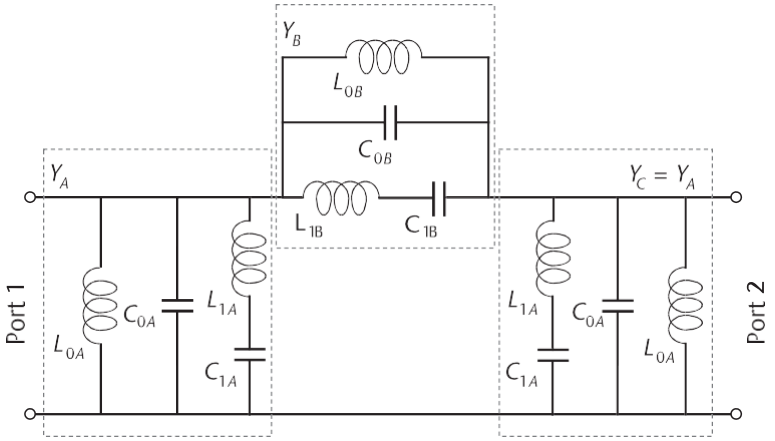

(b)

Figure 3.15*: Equivalent lumped-element circuit model [12]: (a) equivalent circuit of Y_{ij} ; (b) simplified π-type equivalent circuit of a two-port elementary building block*

$$L_{0,ij} = \frac{1}{A_{ij}} \tag{3.10a}$$

$$C_{0,ij} = B_{ij} - \sum_{m=1}^{M} \frac{C_{im}C_{jm}}{\omega_m^2} \tag{3.10b}$$

$$L_{m,ij} = \frac{1}{C_{im}C_{jm}} \tag{3.10c}$$

$$C_{m,ij} = \frac{C_{im}C_{jm}}{\omega_m^2} \tag{3.10d}$$

By explicitly deriving this equivalent circuit from full-wave modelling, we can determine the physical meaning of each lumped member. For instance, we link L_0 and C_0 to the frequency response's low-frequency characteristics. Conversely, the LC-series resonators are connected to the resonant modes of the cavities, which are produced by short-circuiting the ports of the construction block [12]. As such, the precision.

The model is directly impacted by the number of LC-series resonators; increasing the number of resonators in the equivalent circuit model increases its validity range and accuracy. The corresponding model of the building block may be found directly by locating the analogous lumped-element circuit for the ijth item of the Y matrix. Figure 3.15(b) shows the corresponding circuit that results when a 2-port circuit adopts a -type paradigm, with YA = $Y_C = Y_{11}+Y_{12}$ and $Y_B = -Y_{12}$.

This design concentrates on a single LC-series resonator, simplifying the corresponding circuit. Using this approach, we can get the values of the lumped components and the topology of the equivalent circuit directly from the full-wave analysis findings. There's no need for any preliminary fitting or guessing. The process shown for two-port building blocks may, of course, be extended to any number of ports.

This method also makes it possible to develop parametric equivalent circuit models in which the values of the lumped components are determined by the structure's geometrical dimensions. We may create parametric models by doing many full-wave analyses for various geometrical dimensions and using polynomials to match the values of the lumped parts [12].

By considering both conductor and dielectric losses, we may use the same method to derive comparable circuit models of lossy building blocks [13]. The dielectric medium has a complicated dielectric permittivity, whereas the conductor has a limited metal conductivity.

The ij-th element of the Y matrix may be expressed as follows after the term has been extracted from the summation:

$$Y_{j\omega} = \frac{1}{j\omega}A_{ij} + \frac{\sigma_d}{\varepsilon_0\varepsilon_r}B_{ij} + j\omega\left(B_{ij} - \sum_{m=1}^{M}\frac{C_{im}C_{jm}}{\omega_m^2}\right) + j\omega\sum_{m=1}^{M}\frac{C_{im}C_{jm}}{\omega_m^2 + j\omega\omega_m/Q_{m-\omega^2}} \quad (3.11)$$

Where Q_m is the quality factor of the *m*-th resonant cavity mode[13].

Expression (3.11) of the **Y** matrix can be identified as the parallel combination of inductor, resistor, capacitor, and MRL series resonators.

ThevalueofthelumpedelementscanbeanalytICallyobtainedfromexpression (3.11) as

$$R_{0,ij} = \frac{\varepsilon_0\varepsilon_r}{\sigma_d B_{ij}} \quad (3.12a)$$

$$L_{0,ij} = \frac{1}{A_{ij}} \quad (3.12b)$$

$$C_{0,ij} = B_{ij} - \sum_{m=1}^{M}\frac{C_{im}C_{jm}}{\omega_m^2} \quad (3.12c)$$

$$R_{m,ij} = \frac{\omega_m}{Q_m C_{im}C_{jm}} \quad (3.12d)$$

$$L_{m,ij} = \frac{1}{C_{im}C_{jm}} \quad (3.12e)$$

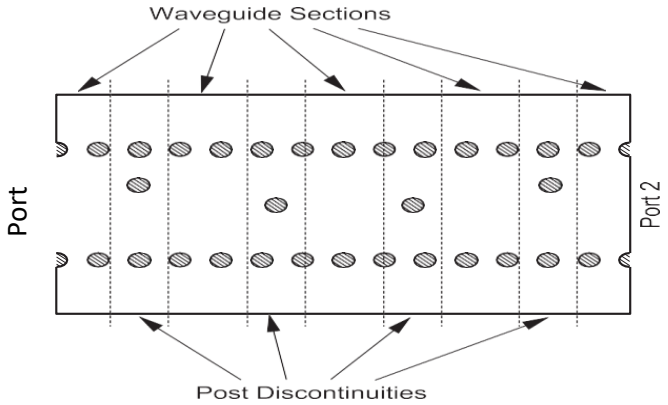

(a)

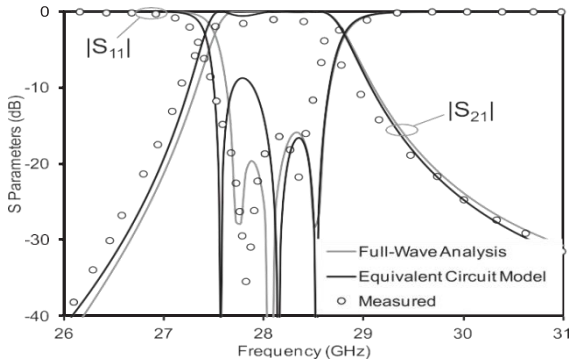

(b)

Figure 3.16: *Modeling of a band-pass SIW filter at 28 GHz by segmentation technique and equivalent circuit models: (a) geometry of the filter and adopted segmentation; (b) scattering parameters of the SIW filter, obtained by full–wave simulations, equivalent circuit model, and measurements (from [12]*

$$C_{m,ij}=\frac{c_{im}c_{jm}}{\omega_m^2} \qquad (3.12f)$$

The model's complete derivation follows the same procedure as in the loss-less case, adding resistors to account for losses [13]. Parametric equivalent circuit models allow for rapid analysis and design of SIW circuits. Once these models become available, one can design SIW circuits using only a Spice-like circuit simulator, eliminating the need for full-wave simulators. To illustrate the use and features of equivalent circuit models, we employ the segmentation technique, dividing the circuit into nine sub-circuits: two centered-post discontinuities, two offset-post discontinuities, and five SIW sections (Figure 3.16(a)).

The EA lumped-element equivalent circuit models each discontinuity, featuring five modes per port and one LC series resonator. The third-order polynomial function expresses the values of the lumped elements (inductance or capacitance) based on the offset value of the post. We use the analytical frequency response of the equivalent rectangular waveguide to model the SIW sections. For each port, we take into account five modes. Figure 3.16(b) displays the filter's frequency response, calculated using equivalent circuit models. It compares with the en-bloc analysis of the BI-RME method and the measurement results from [14].

3.6.5 Substrate Integrated Waveguide Filters Based on a Dielectric Layer with Periodic Perforations:

The investigation of a novel class of bandpass SIW filters based on a periodic perforation of the dielectric substrate is described.The structure has been studied starting from the classical waveguide iris-type filter theory[15]. In particular, the dielectric perforation of the substrate (Figure 3.17(*a*)) helps to reduce the local effective dielectric permittivity , creating waveguide sections below cutoff (Figure 3.17 2(*b*)) thus creating immittance inverters

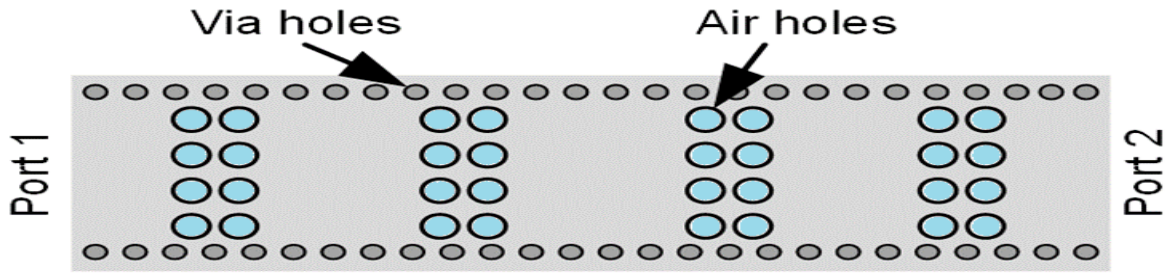

(a)

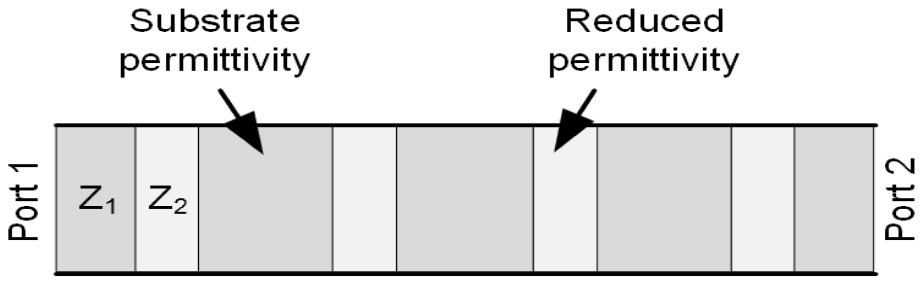

(b)

Figure 3.17: *SIW filter with periodic perforations: (a) physical geometry of the filter; (b) equivalent structure based on alternate sections with substrate permittivity and reduced permittivity (perforated areas).*

The design properties of the immittance inverters have been elucidated, encompassing a comprehensive overview of the meticulous control protocols for the coupling mechanism. Noteworthy is the resonator which upholds a succinct physical length (approximately λg/6 as evidenced in prior demonstrations). Conversely, the dimensions of the coupling components are comparatively more expansive due to their fabrication through perforated waveguide segments. These configurations display enhanced out-of-band capabilities compared to iris-type filters, showcasing reduced susceptibility to manufacturing discrepancies alongside a parallel frequency response.

This attribute of the perforated SIW filters paves the way for innovative manufacturing prospects through the adoption of cost-effective techniques like punching. By integrating a Half-mode structure, the filter's dimensions can be streamlined [15]. An initial prototype has been devised, commencing from a full-mode filter blueprint.

The implementation of the Folded half-mode filter was introduced to surmount the augmented insertion loss of the half-mode structure, while upholding compact dimensions and diminishing radiation losses [15]. Furthermore, the incorporation of transmission zero plays a pivotal role in bolstering the out-of-band rejection capacities.

3.6.5.1 Operation principle of the filte

In order to introduce a circuital model of Figure 3.17, the evanescent waveguide section can be represented as an impedance inverter (plus two transmission lines) and the propagating waveguide sections connecting two evanescent sections as dispersive transmission lines (Figure 3.18).

The normalized impedance inverter $k_{i,j}^{(NOR)} = k_{i,j}/z_0$ can be evaluated directly from the coupling matrix elements

$$k_{S,1}^{(NOR)} = M_{S.1}\sqrt{\frac{\pi}{2}FBW_{\lambda_g}} \tag{3.13}$$

$$k_{N,L}^{(NOR)} = M_{N.L}\sqrt{\frac{\pi}{2}FBW_{\lambda_g}} \tag{3.14}$$

$$k_{i,j}^{(NOR)} = M_{i,j}\frac{\pi}{2}FBW_{\lambda_g} \tag{3.15}$$

Where the subscripts S and L stand for source and load, while indices i and j refer to the i-th and j-th resonator, respectively, and N is the total number of resonators. The fractional bandwidth FBW is calculated by using the waveguide wavelength to account fordispersion[16].

$$FBW_{\lambda_g=\frac{\lambda_{g2}-\lambda_{g1}}{\lambda_{g0}}} \tag{3.16}$$

being λ_g1 and λ_g2the waveguide wavelengths at the lower and higher pass-band edge, respectively, while λ_g0is the waveguide wavelength at the central frequency:

$$\lambda_{g0} = \sqrt{\lambda_{g1}\lambda_{g2}} \tag{3.17}$$

3.6.5.2 Synthesis of the immittance inverter:

The section with reduced permittivity ε_{r1} (Figure. 3.18(a)) acts as an immittance inverter with two transmission line sections (Figure. 3.18(b)). This equivalence is shown by evaluating the reflection coefficient of the evanescent waveguide section[16].

The propagation constant β_0 of the input and output waveguides is real, whereas the one of the evanescent waveguide β_1 is purely imaginary

$$\beta_0 = \sqrt{\left(\frac{2\pi}{\lambda}\right)^2 \varepsilon_{r0-} \left(\frac{\pi}{w}\right)^2} \tag{3.18}$$

$$\beta_1 = -j\gamma_1 = \sqrt{\left(\frac{2\pi}{\lambda}\right)^2 \varepsilon_{r1-} \left(\frac{\pi}{w}\right)^2} \tag{3.19}$$

Where λ the wavelength in vacuum and w is is the waveguide width. Analogously, the characteristic impedance Z_0 (in the propagating waveguide section) is real, whereas Z_1 (in the evanescent waveguide section) is imaginary

$$Z_0 = \frac{\omega\mu}{\beta_0} \tag{3.20}$$

$$Z_0 = \frac{\omega\mu}{\beta_0} = \frac{\omega\mu}{-j\gamma_1} \tag{3.21}$$

The input impedance Zin can be expressed as

$$Z_{in} = Z_1 \frac{Z_0 + jZ_1 tan(\beta_1 l)}{Z_1 + jZ_0 tan(\beta_1 l)} \tag{3.22}$$

Where is the length of the evanescent waveguide section. This allows the evaluation of the reflection coefficient Γ

$$\Gamma = s_{11} = \frac{Z_{in} - Z_0}{Z_{in} + Z_0} = \frac{Z_1 \frac{Z_0 + jZ_1 tan(\beta_1 l)}{Z_1 + jZ_0 tan(\beta_1 l)} - Z_0}{Z_1 \frac{Z_0 + jZ_1 tan(\beta_1 l)}{Z_1 + jZ_0 tan(\beta_1 l)} + Z_0} = \frac{j(Z_1 - Z_0)^2 tan(\beta_1 l)}{2Z_0 Z_1 + j(Z_1 + Z_0)^2 tan(\beta_1 l)} \quad (3.23)$$

$$= \frac{(\gamma_1^2 + \beta_0) tanh(\gamma_1 l)}{2j\gamma_1\beta_0 + (\gamma_1^2 - \beta_0) tanh(\gamma_1 l)}$$

$$= \frac{(\gamma_1^2 + \beta_0) tanh(\gamma_1 l)}{\sqrt{4(\gamma_1\beta_0)^2 + (\gamma_1^2 - \beta_0) tanh(\gamma_1 l)}} = e^{-jarcsin\left(\frac{2\gamma_1\beta_0}{(\gamma_1^2 - \beta_0) tanh(\gamma_1 l)}\right)}$$

Therefore, with reference to the Appendix, the evanescent waveguide section can be represented by an impedance inverter and two transmission line sections, as shown in Figure 3.18(b). In fact, the normalized inverter of value

$$k^{(NOR)} = \frac{k}{Z_0} = \sqrt{\frac{1 + S_{11}^{Ampi}}{1 - S_{11}^{Ampi}}} \quad (3.24)$$

With

$$S_{11}^{Ampi} = \frac{(\gamma_1^2 + \beta_0) tanh(\gamma_1 l)}{\sqrt{4(\gamma_1\beta_0)^2 + (\gamma_1^2 - \beta_0) tanh(\gamma_1 l)}} \quad (3.25)$$

accounts for the return loss amplitude of the evanescent waveguide section, while the transmission line sections at the inverter ports with length

$$\Lambda = \frac{1}{2\beta_0} arctan\left(\frac{2\gamma_1\beta_0}{(\gamma_1^2 - \beta_0) tanh(\gamma_1 l)}\right) \quad (3.26)$$

take into account the return loss phase.

In conclusion, (3.21) and (3.23) provide analytical formulas for the design of the impedance inverter in Figure. 3.18(b).

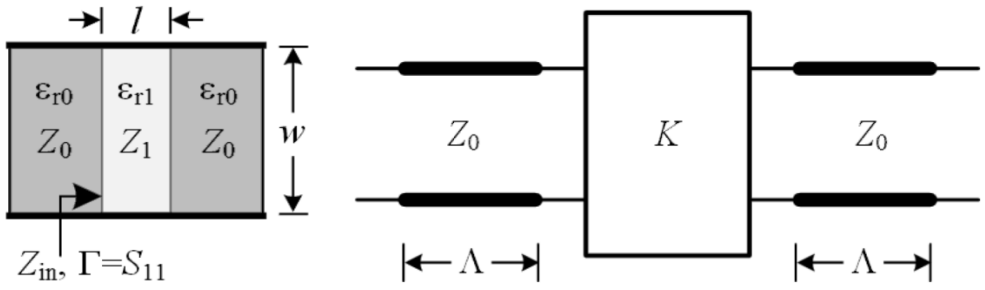

(a) (b)

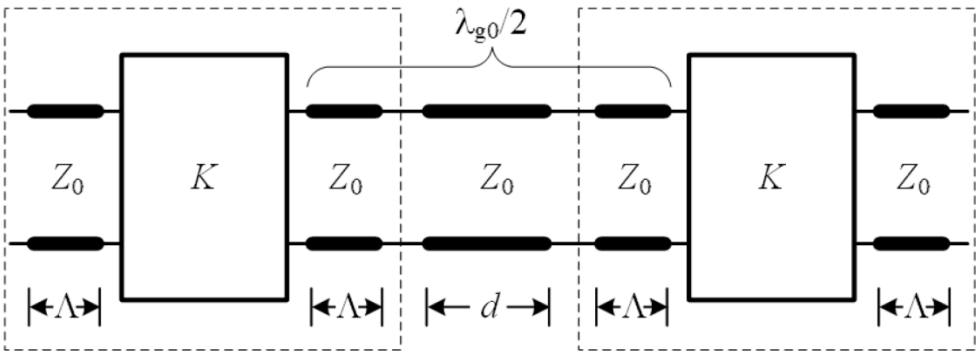

(c)

Figure 3.18: *Evanescent waveguide section: (a) geometrical parameters of the evanescent waveguide section; (b) representation as an inverter and two transmission line sections; (c) resonator by two inverters.*

3.7 The advantages of SIW technology:

SIW technology is a hybrid technology between volumetric technology and planar technology, which combines the advantages of both technologies and solves the problems that arise in each of these technologies for a new GIS technology. It is very promising in terms of quality and price. The following table will summarize the characteristics of the two technologies (volumic and planar) and will thus allow us to deduce the advantages of SIW technology.

Planar technology	Volumic technology
Low manufacturing cost. Space-saving (small size). Low weight. Limited electrical performance. Low quality factor. Better bandwidth. Ease of integration.	Low attenuation losses. High-quality factor. Expensive. Bulky structure. Narrow bandwidth. Impossible integration of circuits.

Table 3.1: Comparative table of planar and volumic technologies.

By combining the advantages of the two previous technologies, we will have the advantage of

- SIW technology is as follows:
- Low manufacturing cost.
- Small size and low weight.
- Ease of integration of millimetre wave circuits.
- Low attenuation losses.
- High-quality factor.
- Expensive.
- Bulky structure.
- Narrow bandwidth.
- Impossible integration of circuits.
- Possibility of integration with passive circuits as well as active circuits.
- No radiation loss and low transmission losses.
- Ease of implementation.
- High-quality factor (the ratio between the centre frequency and the band

passing).

- Excellent broadband application.
- Very good dispersion.
- Isolate most of the parasitic modes and see complete elimination.

3.8 Disadvantages of SIW technology:

The difficulty of modelling, and therefore, the significant adjustment times, are of these structures from a design point of view. This is all the more difficult as SIW structures have low flexibility. Indeed, the coupling possibilities and the topological flexibility is not very important, which makes design work difficult. Their mechanical fragility due to the multitude of metallized holes restricts the possible application areas for these structures.

3.9 Conclusion:

Substrate-Integrated Waveguide (SIW) technology represents a significant advancement in microwave and millimeter-wave circuit design, offering a seamless integration with planar circuits and compatibility with existing PCB manufacturing processes. This integration enables the combination of SIW components with other planar circuits, enhancing functionality and reducing system size.

SIW technology provides low loss, high Q-factor, and broad bandwidth performance, making it ideal for high-frequency applications. Its design flexibility allows for the creation of various passive and active components tailored for specific uses, contributing to its widespread applicability in wireless communications, radar, satellite communication, and sensor networks. Additionally, SIW technology is cost-effective due to the use of standard PCB manufacturing techniques, which reduce size, weight, and manufacturing complexity.

Despite challenges such as thermal management and fabrication tolerances, ongoing research and development aim to address these issues and expand SIW applications to new areas, including terahertz and photonic systems.

Overall, SIW technology is poised to drive innovation in communication and sensing technologies by balancing performance, integration, and cost-effectiveness.

3.10 References

[1] R. Garg, I. Bahl, and M. Bozzi, *Microstrip lines and slotlines*. Artech house, 2013.

[2] M. Bozzi, L. Perregrini, and K. Wu, "Efficient modeling of complex substrate integrated waveguide (SIW) circuits," in *2013 International Conference on Electromagnetics in Advanced Applications (ICEAA)*, 2013: IEEE, pp. 1327-1330.

[3] M. Tatari, P. Goudarzi, and H. Naik, "Study of the accelerator production of 169 Yb radioisotope via various particles nuclear reactions," *Journal of Radioanalytical and Nuclear Chemistry*, vol. 327, pp. 525-532, 2021.

[4] W. MOULESSEHOUL and S. MERIAH, "Conception de cellules rayonnantes a base d'antenne bowtie modifiee pour les reflectarray."

[5] C. Mea, N. CHERIF, H. Boubakar, M. Abri, and H. Badaoui, "SIW based high performance bandpass filter loaded with Hilbert cells," 2024.

[6] A. Rhbanou, M. Sabbane, and S. Bri, "Design of K-band substrate integrated waveguide band-pass filter with high rejection," *Journal of Microwaves, Optoelectronics and Electromagnetic Applications*, vol. 14, pp. 155-169, 2015.

[7] A. O. Nwajana and E. R. Obi, "A review on SIW and its applications to microwave components," *Electronics*, vol. 11, no. 7, p. 1160, 2022.

[8] S. Kurudere, "Design of substrate integrated waveguide based bandpass filters and power dividers," Bilkent Universitesi (Turkey), 2013.

[9] Z. Fifer, "Analog cosmology with two-fluid systems," University of Nottingham, 2022.

[10] M. Bozzi, L. Perregrini, G. Conciauro, and W. Ke, "Multi-mode equivalent circuit models for substrate-integrated waveguide discontinuities," 2006.

[11] G. Conciauro, M. Guglielmi, and R. Sorrentino, "Advanced modal analysis," 2000.

[12] M. Bozzi, L. Perregrini, and K. Wu, "A novel technique for the direct determination of multimode equivalent circuit models for substrate integrated waveguide discontinuities," *International Journal of RF and Microwave Computer-Aided Engineering: Co-sponsored by the Center for Advanced Manufacturing and Packaging of Microwave, Optical, and Digital Electronics (CAMPmode) at the University of Colorado at Boulder*, vol. 19, no. 4, pp. 423-433, 2009.

[13] M. Bozzi, L. Perregrini, and K. Wu, "Modeling of losses in substrate integrated waveguide by boundary integral-resonant mode expansion method," in *2008 IEEE MTT-S International Microwave Symposium Digest*, 2008: IEEE, pp. 515-518.

[14] D. Deslandes and K. Wu, "Single-substrate integration technique of planar circuits and waveguide filters," *IEEE Transactions on microwave theory and Techniques*, vol. 51, no. 2, pp. 593-596, 2003.

[15] L. Silvestri, "Novel classes of bandpass filters in substrate integrated waveguide technology," 2019.

[16] L. Silvestri, E. Massoni, C. Tomassoni, A. Coves, M. Bozzi, and L. Perregrini, "Substrate integrated waveguide filters based on a dielectric layer with periodic perforations," *IEEE Transactions on Microwave Theory and Techniques*, vol. 65, no. 8, pp. 2687-2697, 2017.

CHAPTER 4 :

Simulation and Results

4.1 Introduction:

Microwave devices are increasingly prevalent today, making precise simulation before implementation essential. In this chapter, we present the design results of microwave filters, achieved using the HFSS (High-Frequency Structure Simulator) software. This comprehensive tool facilitates both the design of filters and the plotting of their frequency responses.

In the first part of this chapter, we explore a new type of miniature microstrip dual-mode resonator for filter applications. The open-loop resonator is renowned for its versatility in designing cross-coupled resonator filters. Several filter examples demonstrate the applications of this innovative dual-mode resonator.

The second part delves into a novel class of bandpass SIW (Substrate Integrated Waveguide) filters, which utilize periodic perforation of the dielectric substrate. We provide two examples to illustrate the applications of these SIW filters.

4.2 Microwave Filter Design Theory

4.2.1Bandpass filter based on an electronic circuit:

The design of bandpass filters based on electronic circuits is based on the following steps: Specification specifications: filter type, filter order n, filter ripple level, filter bandwidth BW, relative bandwidth FBW, cutoff frequency, and centre frequency determination of the values of the elements g_i.

- calculation of the coupling elements $M_{i,i+1}$ and the external quality factors (Q_{e1} and Q_{en}), which are linked to the elements g_i.
- calculation of localised elements $R_0L_0C_0$ of resonators.
- calculation of series impedances of equivalent circuits with lumped elements.

4.3 Dual-Mode Open-Loop Resonators :

4.3.1 two-pole Dual-Mode Open-Loop Resonators

↳ example A

- **Filter specifications:**

Settings	Values
Filter order (Number of poles)	02
Type of approximation	Chebyshev
Central frequency f_0	1.063GHz
Bandwidth (BW) à –3 dB	0.120 GHz
Amplitude of l'ondulation LAr (passband ripple)	0.1 dB
Attenuation	< -20 dB
TFZ	f_{zt1}=1.1667 GHz

Table 4.1: Specifications

- **Frequency response of the ideal bandpass filter:**

Once the order of the filter is determined, knowing the maximum ripple of 0.1 dB and the specifications defined in the specifications, we obtain the coefficients g_i (i=1-2) of the bandpass prototype of the type filter Chebyshev:

g_0	g_1	g_2	g_3
1	0.8431	0.6620	1.3554

Using the specifications defined in the specifications to calculate:

Relative bandwidth:

$$\omega_0 = 2\pi f_0 \tag{4.1}$$
$$= 6.675664$$
$$FBW = \frac{BW}{f_0} \tag{4.2}$$
$$= 0.1128 = 11.28\%$$

Quality Factor [1]:

$$Q_{e1} = \frac{1}{ms1^2 \times FBW} \tag{4.3}$$

$$= \frac{1}{1.0372^2 \times 0.1128} = 8.2407$$

$$Q_{e2} = \frac{1}{ms2^2 \times FBW} \tag{4.4}$$

$$= \frac{1}{0.6734^2 \times 0.1181} = 19.5499$$

The resonant frequency [1] :

$$f_{01} = f_0 \cdot \left(1 - \frac{m11.FBW}{2}\right) \tag{4.5}$$

$$= 1.063 \times \left(1 - \frac{1.6127 \times 0.1181}{2}\right) = 0.96\ GHz$$

$$f_{02} = f_0 \cdot \left(1 - \frac{m22.FBW}{2}\right) \tag{4.6}$$

$$= 1.063 \times \left(1 - \frac{-1.5589 \times 0.1181}{2}\right) = 1.1564\ \text{GHz}$$

Coupling coefficients:

$$M_{i,i+1} = \frac{1}{\sqrt{g_i g_{i+1}}} \tag{4.7}$$

Q_{e1}	M_{12}	M_{21}	Q_{e2}
8.2407	0.1578	0.1578	19.5499

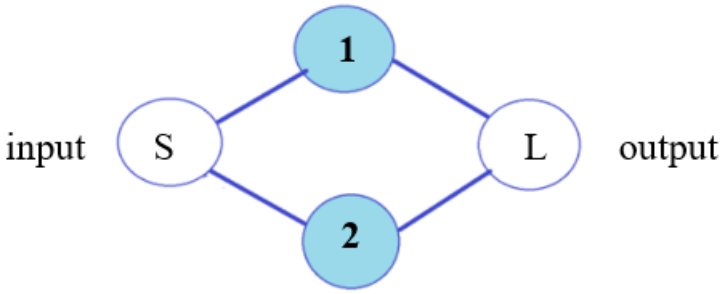

***Figure 4.1**:Coupling structure for a two-pole dual-mode open-loop resonator filter*[1]

- **Coupling matrix**

⇨ **Normalized:**

where the node S denotes the source or input, the node L denotes the load or output, and the nodes 1 and 2 represent the odd and even modes[1], respectively. For this coupling structure, an n + 2 coupling matrix is given by:

$$m=\begin{bmatrix} 0 & ms1 & ms2 & 0 \\ ms1 & m11 & 0 & mL1 \\ ms2 & 0 & m22 & mL2 \\ 0 & mL1 & mL2 & 0 \end{bmatrix} \quad (4.8)$$

$$m=\begin{bmatrix} 0 & 1.0372 & 0.6734 & 0 \\ 1.0372 & 1.6127 & 0 & -1.0372 \\ 0 & 0 & -1.5589 & 0.6734 \\ 0 & -1.0372 & 0.6734 & 0 \end{bmatrix}$$

it should be noted that $m_{L1} = -m_{S1}$ for the odd mode and $m_{L2} = m_{S2}$ for the even mode. Using the formulations introduced in[1] .

⇨ **Dénormalized:**

After determining the normalized coupling matrix [*m*] for a coupled resonator topology, the actual coupling matrix [*M*] of a coupled resonator device with given specification can be calculated by prototype de-normalization of the matrix [*m*] at a desired bandwidth, as follows:

$$M_{i,i+1} = m_{i,i+1}.FBW \text{ For i=1 to n-1} \quad (4.9)$$

- **Filter equivalent circuit:**

gThe filter specifications result in desired coupling matrix elements $M_{i,i+1}$,Q_e and Q_s . The circuit diagram for this filter is shown in Figure 4.1 , where the lumped elements $R_0L_0C_0$ represent the four synchronously tuned resonators and quarter-wave transmission lines, which

have an electrical length EL = ±90° at frequency central f_0, The corresponding design parameters for the bandpass filter are:

The localized elements $R_0L_0C_0$ of resonators:

$$L_0 = \frac{Z}{\omega_0 Q_e} * 10^9 nH \tag{4.10}$$

$$= 1.0273\text{nH}$$

$$C_0 = \frac{Z}{\omega_0 Q_e} * 10^{12} pF \tag{4.11}$$

$= 0.22364\ \text{p}F$

$R_0 = 100000\ \Omega$

Resonator impedances:

$$Z_{i,i+1} = \frac{Z}{Q_e M_{i,i+1}} \tag{4.12}$$

Lorsque $Z_0 = 50\Omega$ est l'impédance d'alimentation au niveau des ports d'E/S :

$$Z_{12} = 42.9497\Omega$$

4.3.1.1 Equivalent scheme under AWR:

The bandpass filter prototype operates using the characteristic impedance of the positive two-wave resonator lines, and a parallel $R_0L_0C_0$ resonant circuit. After calculating the elements of the series and parallel branches, the equivalent circuit of the filter is illustrated in Figure 4.2:

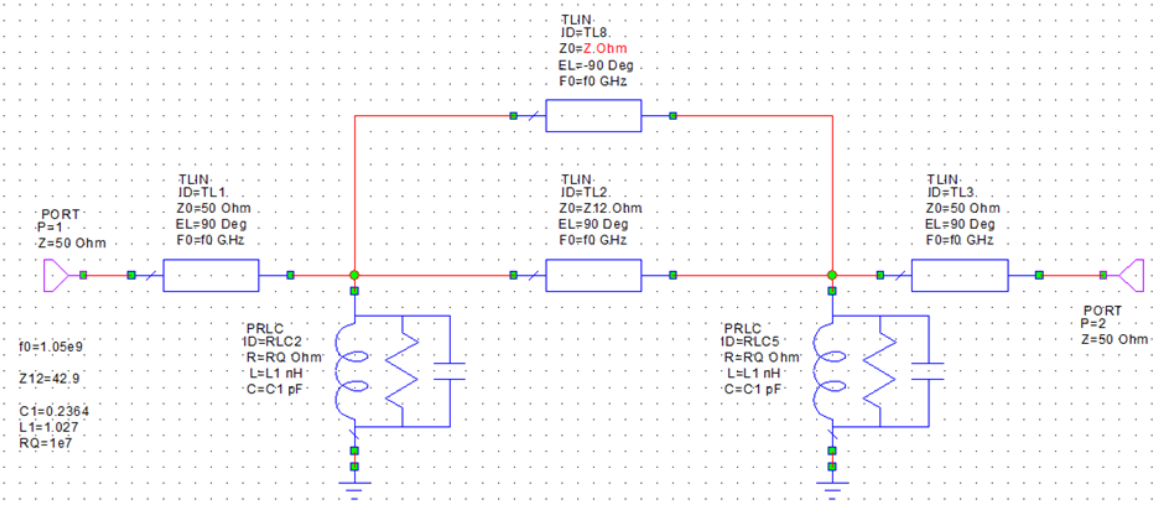

***Figure 4.2**: bandpass filter with localized elements of order 2 with circuit*

resonant $R_0L_0C_0$ parallel.

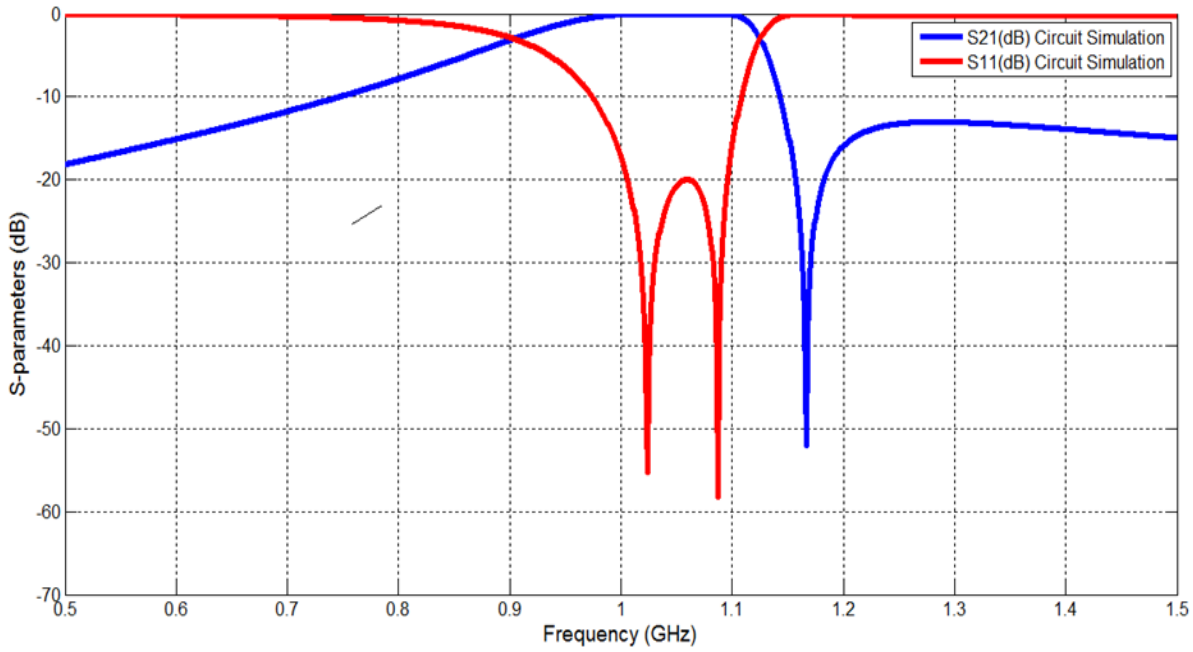

***Figure 4.3**: Ideal response of the Chebyshev bandpass filter of order 2*

The ideal response in transmission and reflection of the equivalent circuit in lumped elements, analyzed with AWR is shown in Figure (4.3)

4.3.1.2 EM design of the bandpass filter in planar technology:

Figure 4.4 shows the basic topology of a dual-mode microstrip open-loop resonator. The dual-mode resonator consists of an open loop with an open gap, g.

The open loop has a line width of W1 andasizeofL1a × L1b. A loading element with a form of open stepped impedance stub, is tapped from inside onto the open loop. The loading element has dimensions of L2a and W2a for the narrow line section and L2b and W2b for the wide-line section. The resonator is coupled to the input and output(I/O)ports with a feed structure having a line width of W and a coupling spacings. The port terminal impedance is Wfeed. The first two resonating modes, existing in the resonator of Figure 4.4, are referred to as the odd and even modes.

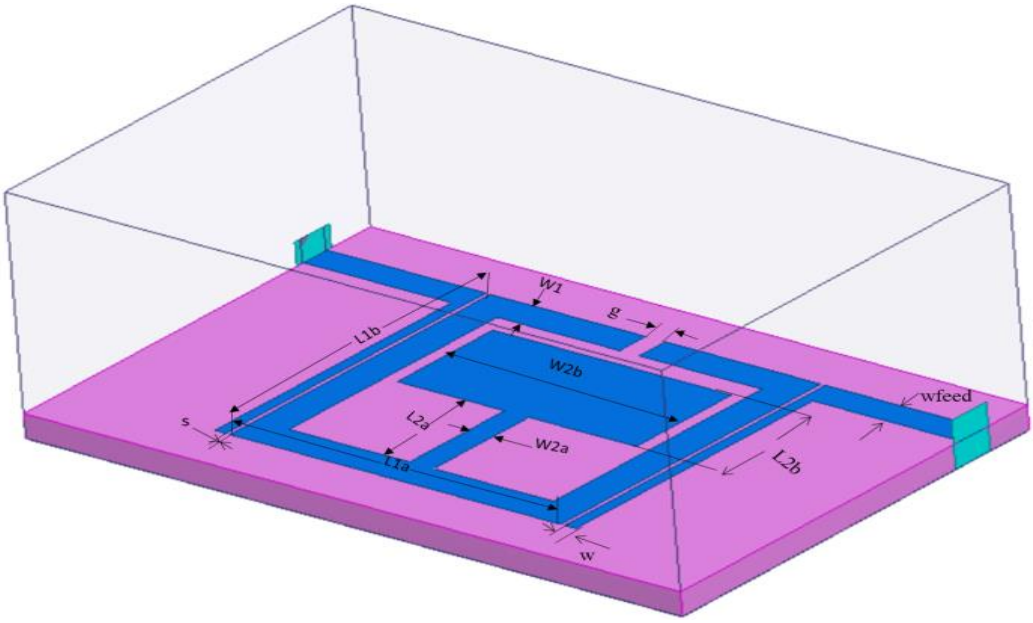

Figure 4.4 *:topology of a dual-mode microstrip open-loop resonator*

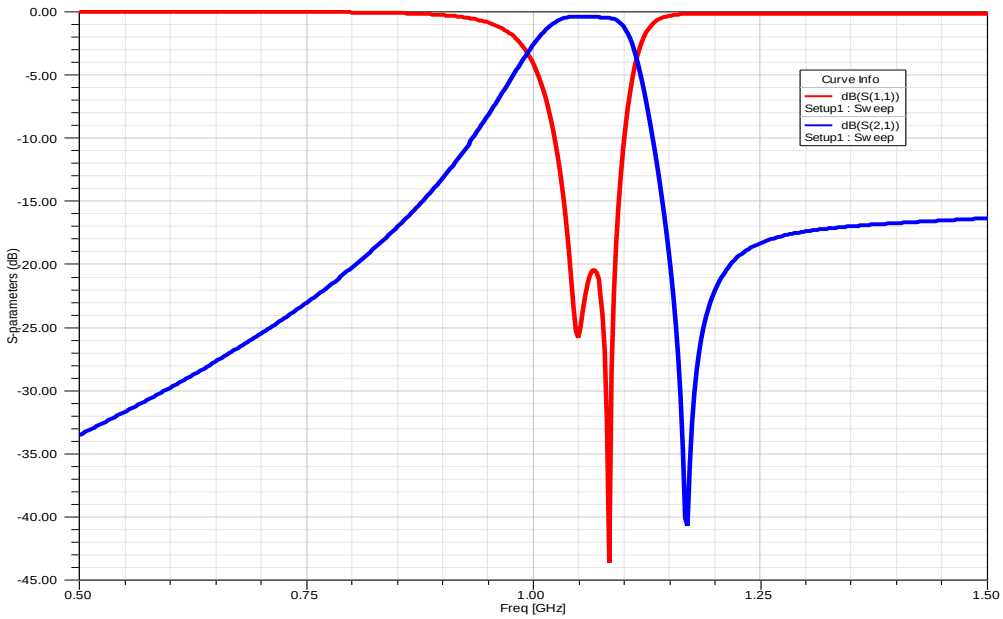

Figure 4.5*: EM-simulated responses of the filter with HFSS*

We present in Figure 4.5, the simulation results of the filter (two pole dual mode open-loop) and transmission obtained with the HFSS software.

The central frequency of this filter is of order 3 and f = 1.063 GHz and the bandwidth is approximately 0.120 GHz. The frequency response shows that|S11| is less than -20dB between 0.89 GHz and 1.02 GHz.

- **The Electromagnetic design of the applied filter:**

This geometric configuration is simulated on a "RO3010" substrate having a relative permittivity ε_r=10.2, a dielectric loss tangent 0.017 and a thickness of h= 1.27 mm.

Settings	x_1	y_1	H	H_s	L_{1a}	L_{1b}	L_{2a}	L_{2b}	W_{2a}	W_{2b}	s	g	W_{feed}	W1
Values	20	30	0.017	1.27	15.1	15	5.5	5.5	0.7	8.1	0.2	0.9	2	1.5

Table 4.2: planar bandpass filter dimensions for example A

example B

- **Filter specifications:**

Settings	Values
Filter order (Number of poles)	02
Type of approximation	Tchebychev
Central frequency f_0	1.0155GHz
Bandwidth (BW) à –3 dB	0.120 GHz
Amplitude of l'ondulationLAr (passband ripple)	0.1 dB
Attenuation	< -20 dB
TFZ	f_{zt1}=0.8409 GHz

Table 4.3: Specifications B

- **Frequency response of the ideal bandpass filter:**

Once the order of the filter is determined, knowing the maximum ripple ofA_r= 0.1 dB and the specifications defined in the specifications, we obtain the coefficients g_i (i=1-2) of the bandpass prototype of the type filter Chebyshev:

g_0	g_1	g_2	g_3
1	0.8431	0.6620	1.3554

Using the specifications defined in the specifications to calculate:

Relative bandwidth :

$$\omega_0 = 2\pi f_0 \tag{4.1}$$
$$= 6.37734t$$
$$FBW = \frac{BW}{f_0} \tag{4.2}$$
$$= 0.1181 = 11.81\%$$

Quality Factor:

$$Q_{e1} = \frac{1}{ms1^2 \times FBW} \tag{4.3}$$
$$= \frac{1}{0.9024^2 \times 0.1181} = 10.398$$
$$Q_{e2} = \frac{1}{ms2^2 \times FBW} \tag{4.4}$$
$$= \frac{1}{0.5714^2 \times 0.1181} = 25.9340$$

The resonant frequency :

$$f_{01} = f_0 \cdot \left(1 - \frac{m11.FBW}{2}\right) \tag{4.5}$$
$$= 1.0155 \times \left(1 - \frac{-1.0918 \times 0.1181}{2}\right) = 1.08GHz$$
$$f_{02} = f_0 \cdot \left(1 - \frac{m22.FBW}{2}\right) \tag{4.6}$$
$$= 1.0155 \times \left(1 - \frac{1.3487 \times 0.1181}{2}\right) = 0.9346 \text{ GHz}$$

Coupling coefficients:

$$M_{i,i+1} = \frac{1}{\sqrt{g_i g_{i+1}}} \tag{4.7}$$

Q_{e1}	M_{11}	M_{22}	Q_{e2}
10.398	0.1744	0.1744	25.9340

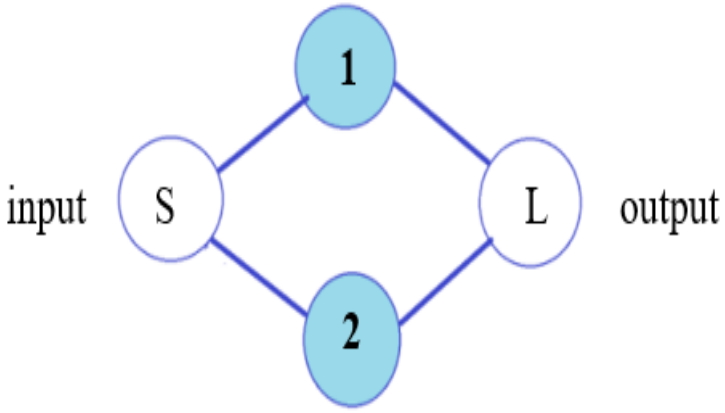

Figure 4.6 : *Coupling structure for a two-pole dual-mode open-loop resonator filter*[1].

- **Coupling matrix**

⇨ **Normalized:**

where the node S denotes the source or input, the node L denotes the load or output, and the nodes 1 and 2 represent the odd and even modes[1], respectively. For this coupling structure, an n + 2 coupling matrix is given by:

$$m=\begin{bmatrix} 0 & 0.9024 & 0.5714 & 0 \\ 0.9024 & -1.0918 & 0 & -0.9024 \\ 0 & 0 & 1.3487 & 0.5714 \\ 0 & -0.9024 & 0.5714 & 0 \end{bmatrix}$$

it should be noted that $m_{L1} = -m_{S1}$ for the odd mode and $m_{L2} = m_{S2}$ for the even mode. Using the formulations introduced in[1]

- **Filter equivalent circuit:**

The localized elements $R_0L_0C_0$ of resonators:

$$L_0 = \frac{Z}{\omega_0 Q_e} * 10^9 nH \quad (4.10)$$

$$= 1.255 \text{ nH}$$

$$C_0 = \frac{Z}{\omega_0 Q_e} * 10^{12} pF \quad (4.11)$$

$= 0.22364$ pF

$R_0 = 100000\ \Omega$

Resonator impedances :

$$Z_{i,i+1} = \frac{Z}{Q_e M_{i,i+1}} \tag{4.12}$$

Lorsque $Z_0 = 50\Omega$ est l'impédance d'alimentation au niveau des ports d'E/S :

$$Z_{12} = 42.9497\Omega$$

4.3.2.1 Equivalent scheme under AWR:

The bandpass filter prototype operates using the characteristic impedance of the positive two-wave resonator lines, and a parallel $R_0L_0C_0$ resonant circuit. After calculating the elements of the series and parallel branches, the equivalent circuit of the filter is illustrated in Figure 4.7:

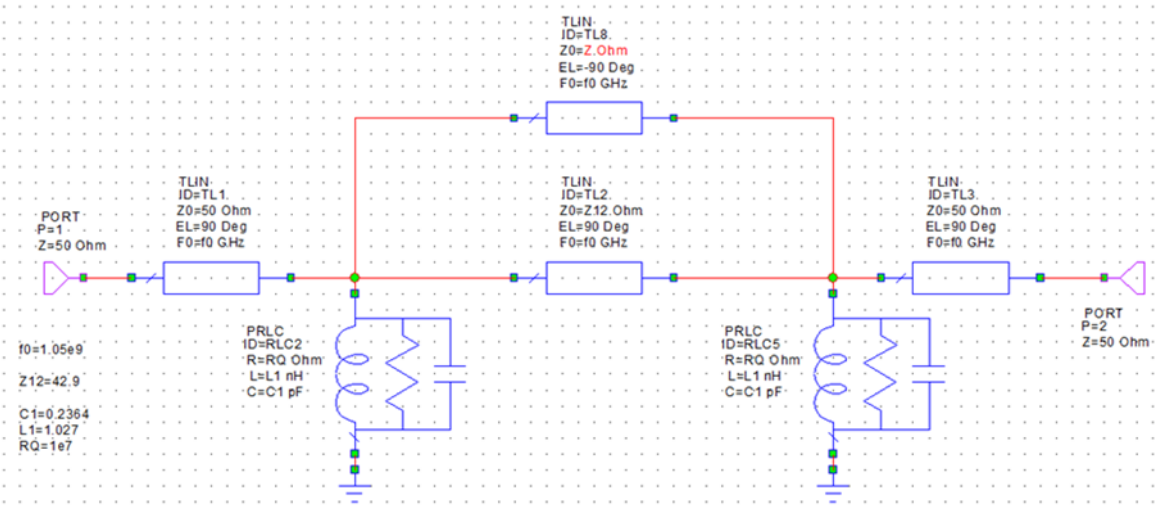

***Figure 4.7**: bandpass filter with localized elements of order 2 with circuit resonant $R_0L_0C_0$ parallel.*

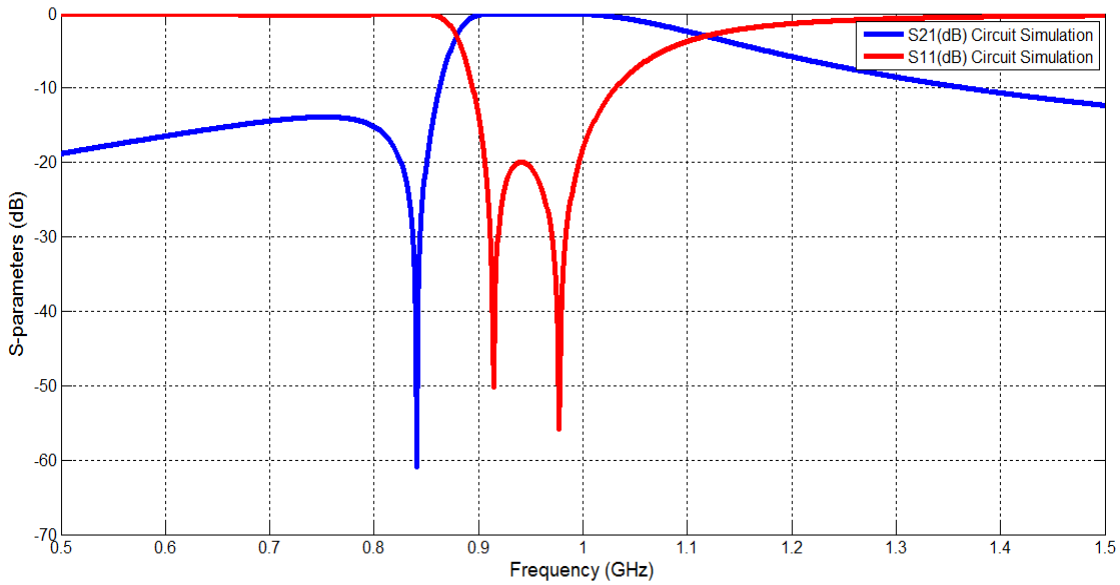

***Figure 4.8**: Ideal response of the Chebyshev bandpass filter of order 2 .*

The ideal response in transmission and reflection of the equivalent circuit in lumped elements, analyzed with AWR is shown in Figure (4.8).

4.3.2.2 EM design of the bandpass filter in planar technology:

Figure 4.9 a displays the layout of the designed filter. The two small open stubs attached to the loading element inside the open loop are deployed for an additional control of the even-mode characteristics, which also allow an efficient utilization of the circuit area inside the open loop

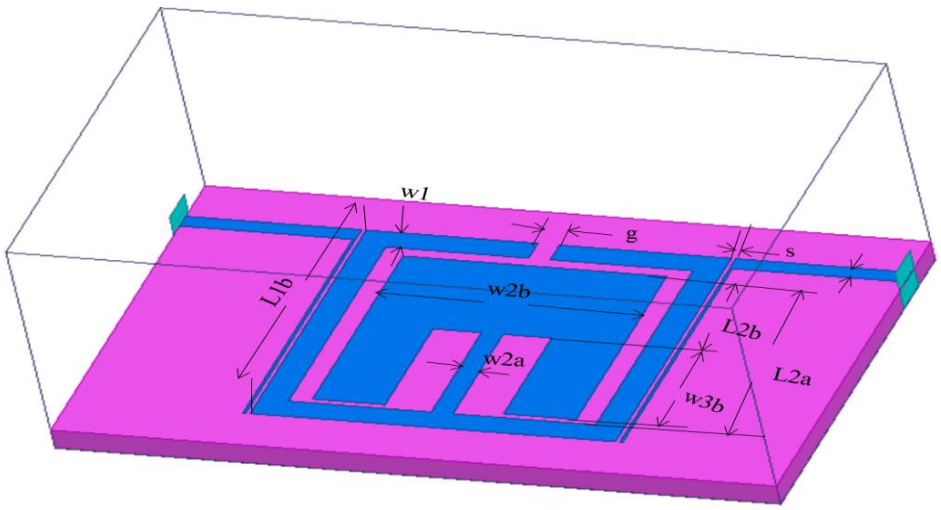

***Figure 4.9**: topology of a two-port microstrip dual-mode open loop filter*

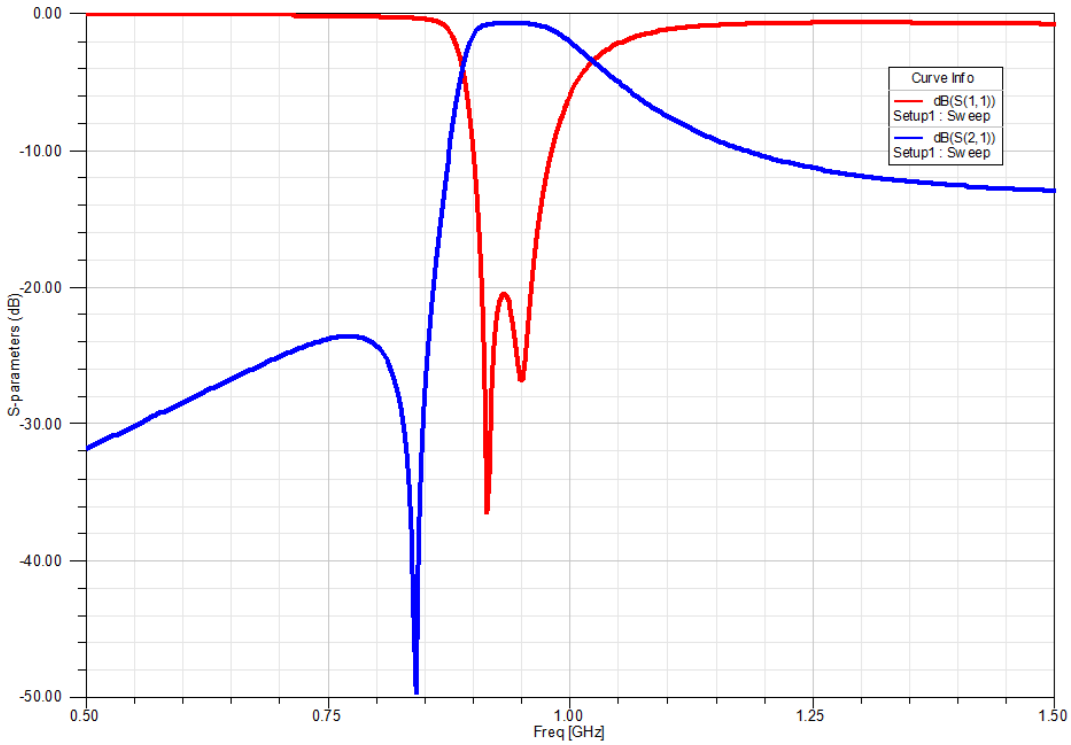

***Figure 4.10**:EM-simulated responses of the filter with HFSS*

We present in Figure 4.10, the simulation results of the filter (two pole dual mode open-loop) and transmission obtained with the HFSS software. The central frequency of this filter is of order 3 and f = 1.0155 GHz and the bandwidth is approximately 0.120 GHz. The frequency response shows that|S11| is less than -20dB between 0.89 GHz and 1.02 GHz.

- **The Electromagnetic design of the applied filter:**

This geometric configuration is simulated on a "RO3010" substrate having a relative permittivity εr=10.2, a dielectric loss tangent 0.017 and a thickness of h= 1.27 mm.

Settings	x_1	y_1	H	Hs	L1a	L1b	L2a	L2b	W2a	W2b	s	g	W_{feed}	W1	W3b
Values	20	30	0.017	1.27	15.1	15	5.5	5.5	0.7	8.1	0.2	0.9	2	1.5	4.9

Table 4.4 :the filter dimensions for example B

4.3.3 The dimensions:

The first two resonating modes, existing in the resonator of Figure 4.4 , are referred to as the odd and even modes,Depending on the dimensions of the resonator these two modes can have the same or different modal frequencies and, for the latter, themodalresonantfrequencyofonemodecanbeeitherhigherorlowerthanthatofthe other one. The characteristics of the dual-mode open-loop resonator are investigated by full-wave electromagnetic (EM) simulation. To excite the resonator, two ports are weakly coupled to the resonator with a large spacing s

4.3.3 Quality factor extraction:

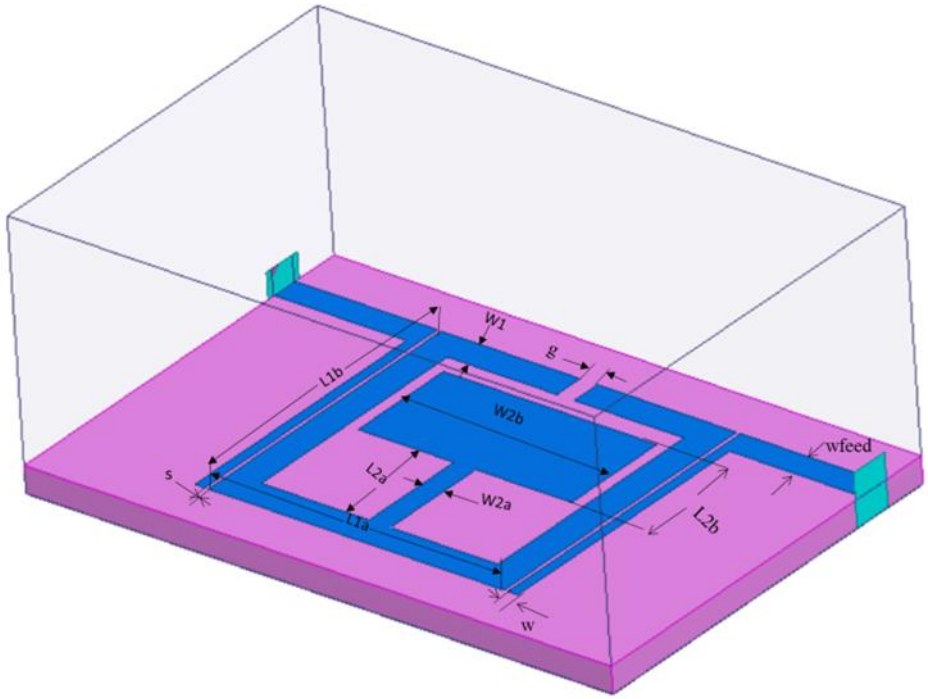

***Figure 4.11**: Structure of a two-port microstrip dual-mode open loop filter*

Figure 4.11 illustrates a device for extracting the external quality factor of the I/O resonator. The resonator, which is assumed to be lossless in the simulation, is excited at port 1 through a 50 ohm line at a location indicated by t. Port 2 is very weakly coupled to the resonator in order to find a bandwidth of -3 dB of the response quantity of S_{21} for the extraction of the external quality factor Q_e.

- **Extraction of coupling coefficient :**

The coupling between two resonators depends on the distance separating them. Indeed, when two resonators are close to each other, their resonances are disturbed because of the coupling that connects them. The HFSS simulator is used to calculate the resonance frequency of even and odd modes. The inter-resonator coupling coefficient, denoted (k), is given by the following formula:

$$K = \frac{{f_2}^2 - {f_1}^2}{{f_2}^2 + {f_1}^2} \tag{4.13}$$

4.3.5Field distribution:

A frequency analysis in the [1-2] GHz band **L** of this structure was carried out with the HFSS software. Figures 4.12, respectively, illustrate the distribution of the field lines. electrical bandpass filter and electric field mapping of the filter

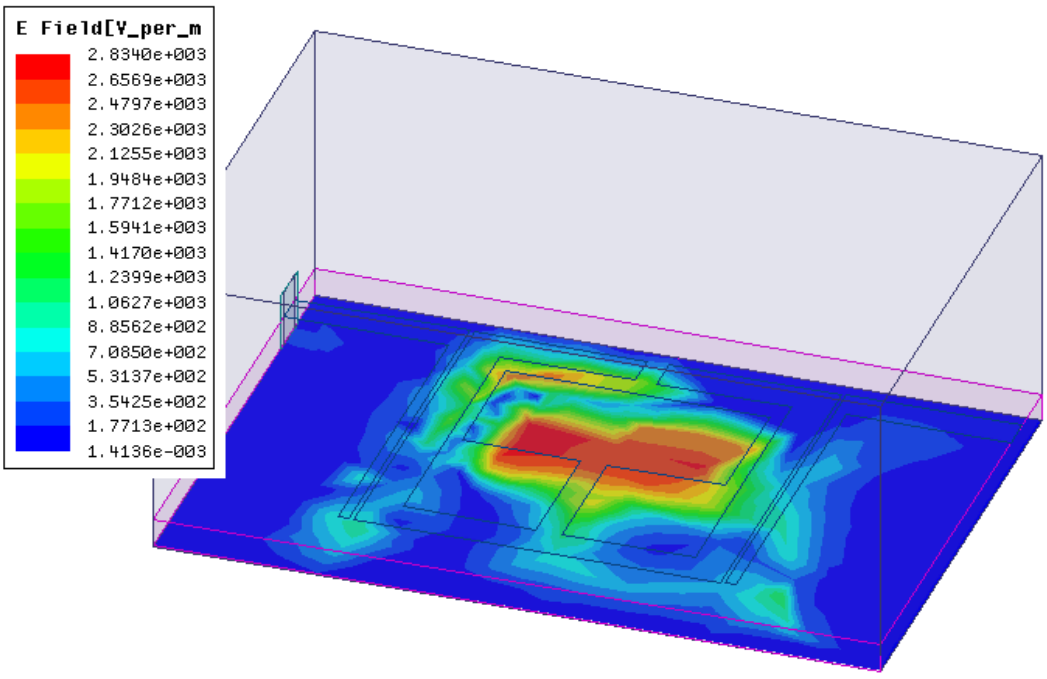

***Figure 4.12**: Distribution of the electric field of the 3th order bandpass filter.*

4.3.6 Four-pole Dual-Mode Open-Loop Resonators :

- **Filter specifications:**

Settings	Values
Filter order (Number of poles)	03
Type of approximation	Tchebychev
Central frequency f_0	1.05GHz
Bandwidth (BW) à –3 dB	0.115 GHz
Amplitude of l'ondulationLAr (passband ripple)	0.1 dB
Attenuation	< -20 dB
TFZ	f_{zt1}=1.0955 GHz

Table 4.5: Specifications C

- **Frequency response of the ideal bandpass filter:**

Once the order of the filter is determined, knowing the maximum ripple of A_r= 0.1 dB and the specifications defined in the specifications, we obtain the coefficients g_i (i=1-2) of the bandpass prototype of the type filter Chebyshev:

N	g1	g2	g3	g4
3	1.0316	1.1474	1.0316	1.0000

Using the specifications defined in the specifications to calculate:

Relative bandwidth:

$$\omega_0 = 2\pi f_0 \quad (4.1)$$

$$= 6.594$$

$$FBW = \frac{BW}{f_0} \quad (4.2)$$

$$= 0.1095 = 10.95\%$$

Quality Factor:

$$Q_{e1} = \frac{1}{ms1^2 \times FBW} \tag{4.3}$$

$$= \frac{1}{0.85^2 \times 0.1095} = 12.64$$

$$Q_{e2} = \frac{1}{ms2^2 \times FBW} \tag{4.3}$$

$$= \frac{1}{0.58^2 \times 0.1095} = 27.1475$$

Coupling coefficients:

$$M_{i,i+1} = \frac{1}{\sqrt{g_i g_{i+1}}} \tag{4.7}$$

Q_{e1}	M_{11}	M_{22}	M_{33}	Q_{e2}
12.64	0.1744	0.1744	0.1744	27.1475

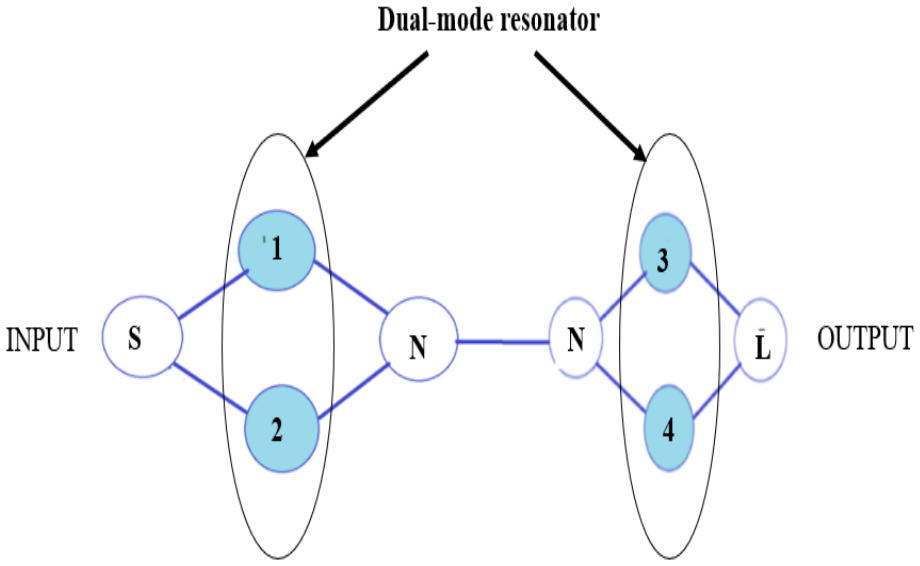

Figure 4.13*. Order 3 coupling graph of the filter*[1]

- **Coupling matrix**

⇨ **Normalized:**

The extracted coupling matrix is given by :

$$m=\begin{bmatrix} 0 & 0.85 & 0.58 & 0.01 & 0 & 0 & 0 & 0 \\ 0.85 & 0.96 & 0 & -0.85 & 0 & 0 & 0 & 0 \\ 0.58 & 0 & -1.01 & 0.58 & 0 & 0 & 0 & 0 \\ 0.01 & -0.85 & 0.58 & 0 & 1.1 & 0 & 0 & 0 \\ 0 & 0 & 0 & 1.1 & 0.74 & -0.6 & 0.46 & 0.01 \\ 0 & 0 & 0 & 0 & 0.46 & 0 & 1.06 & 0.46 \\ 0 & 0 & 0 & 0 & 0.01 & -0.7 & 0.46 & 0 \end{bmatrix}$$

- **Filter equivalent circuit:**

The localized elements $R_0L_0C_0$ of resonators:

$$L_0 = \frac{Z}{\omega_0 Q_e} * 10^9 nH \quad (4.10)$$

$$= 1.1075 \text{ nH}$$

$$C_0 = \frac{Z}{\omega_0 Q_e} * 10^{12} pF \quad (4.11)$$

$= 0.23336 \text{ p}F$

$R_0 = 100000\ \Omega$

Resonator impedances:

$$Z_{i,i+1} = \frac{Z}{Q_e M_{i,i+1}} \quad (4.12)$$

Lorsque $Z_0 = 50\Omega$ est l'impédance d'alimentation au niveau des ports d'E/S :

$$Z_{12} = 42.9497\Omega$$

$$Z_{23} = 54.4571\Omega$$

4.3.6.1 Equivalent scheme under AWR:

The bandpass filter prototype operates using the characteristic impedance of the positive two-wave resonator lines, and a parallel $R_0L_0C_0$ resonant circuit. After calculating the elements of the series and parallel branches, the equivalent circuit of the filter is illustrated in Figure 4.14.

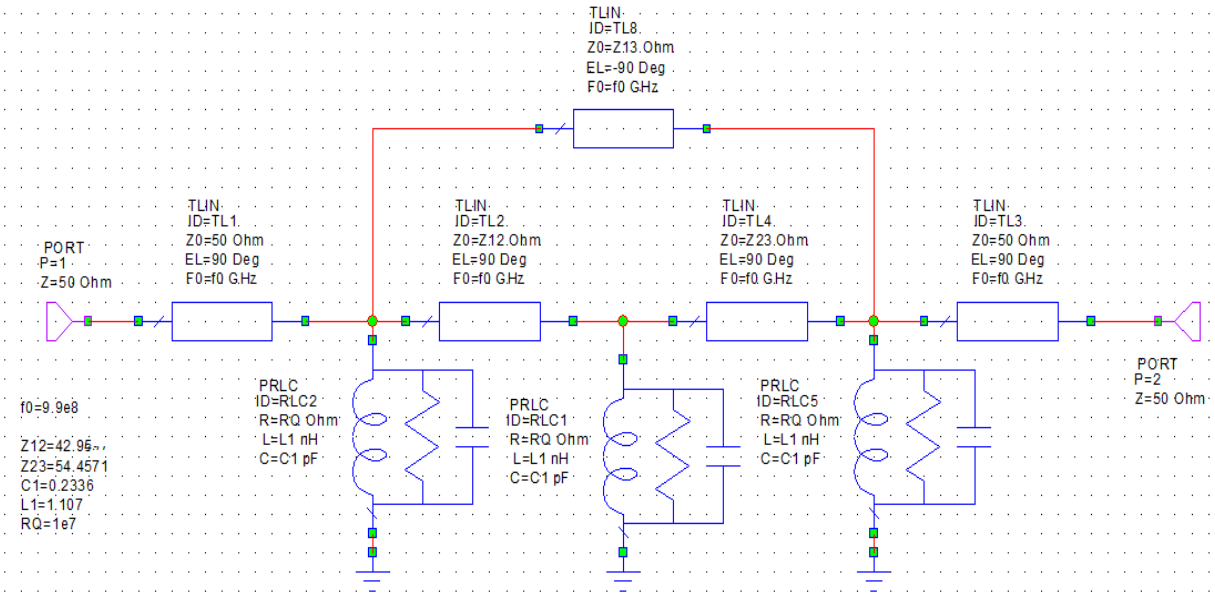

***Figure 4.14**: bandpass filter with localized elements of order 3 with circuit*

$resonant $R_0L_0C_0$ parallel.

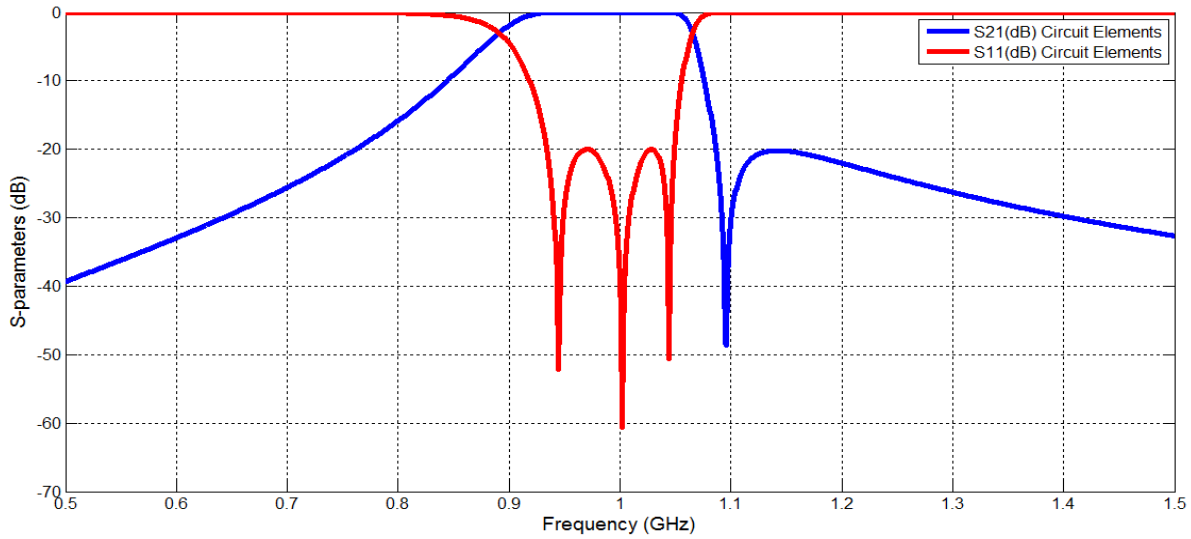

***Figure 4.15**: Ideal response of the Chebyshev bandpass filter of order 3.*

The ideal response in transmission and reflection of the equivalent circuit in lumped elements, analyzed with AWR is shown in Figure (4.15), it appears from the frequency response of our band pass filter that it is centered on the frequency 1.05 GHz .

4.3.6.2 design of the bandpass filter in planar technology:

Figure 4.16 a displays the layout of the designed filter. The two small open stubs attached to the loading element inside the open loop are deployed for an additional control of

the even-mode characteristics, which also allow an efficient utilization of the circuit area inside the open loop

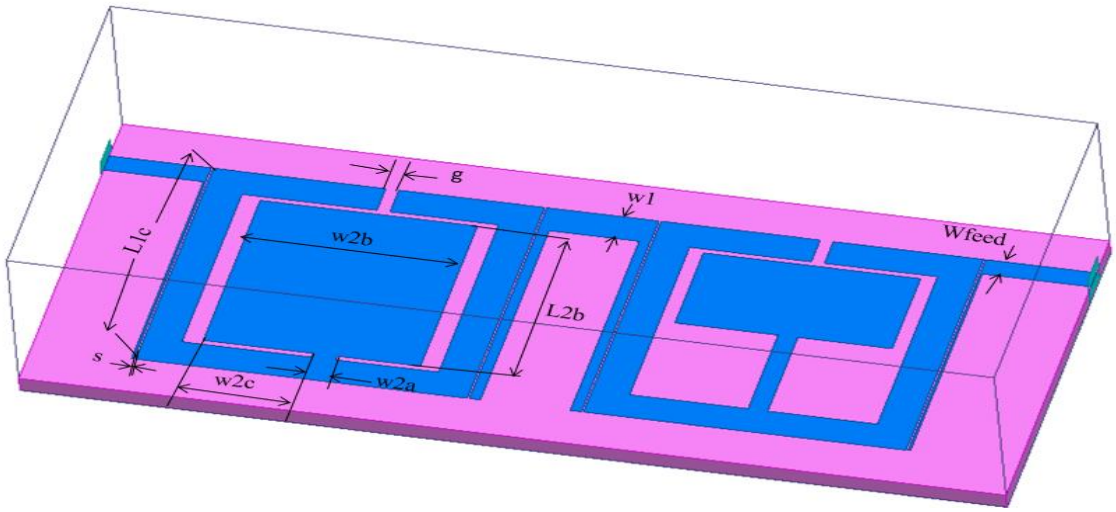

***Figure 4.16**: Structure of filter with three resonators.*

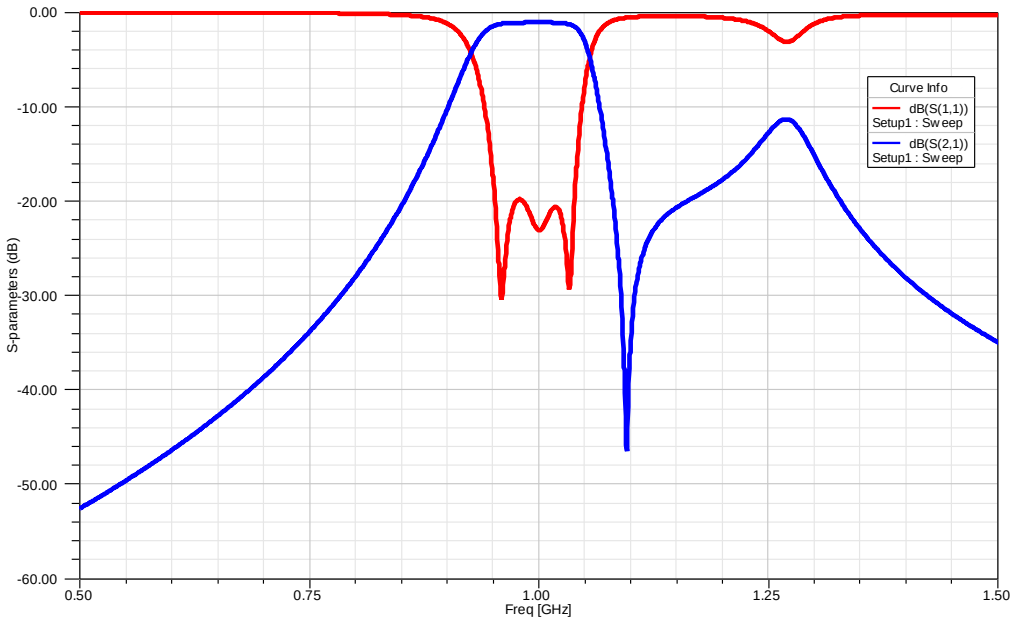

***Figure 4.17**:EM-simulated responses of the filter with HFSS*

We present in Figure 4.17, the simulation results of the filter (four pole dual mode open-loop) and, transmission obtained with the HFSS software. The central frequency of this filter is of order 3 and f = 1.05 GHz and the bandwidth is approximately 0.115 GHz. The frequency response shows that|S11| is less than -20dB between 0.9277 GHz and 1.0559 GHz.

4.3.6.3 Influence of geometric parameters:

- **Variation of via hole diameter "W1":**

The following curves present the influence of some geometric parameters on the frequency response of the parameters S. Figure 4.18 shows the variations of the coefficient reflection and transmission as a function of frequency, taking the diameter of the via (W1) as set to vary. In our simulation, we chose three diameter values: W1= 1.51 mm, W1 = 1.71 mm (this is the reference model), W1= 1.91 mm.

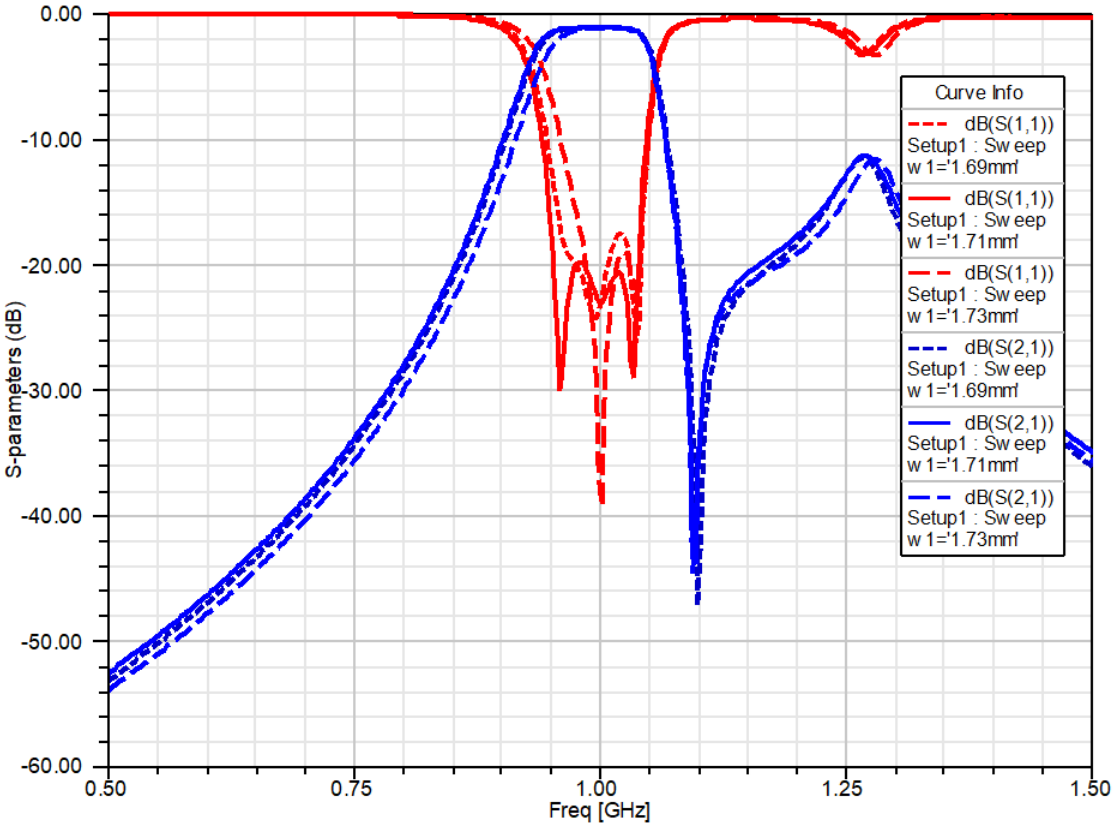

Figure 4.18 *:Simulation results of the planar technology cell proposed with different -W1 values*

The effect of the spacing S on the frequency response of the filter:

The first parametric study shows the influence of the S1 spacing on the simulation results (Figure 4.19). When the S1 space increases (space between the first resonator and the second resonator), we can see that the bandwidth decreases, which implies a narrower bandwidth. We can also see that the best result we obtained is at the value S1=0.62 mm of reflection losses below -20 dB and bandwidth between 0.925 GHz and 1.075 GHz.

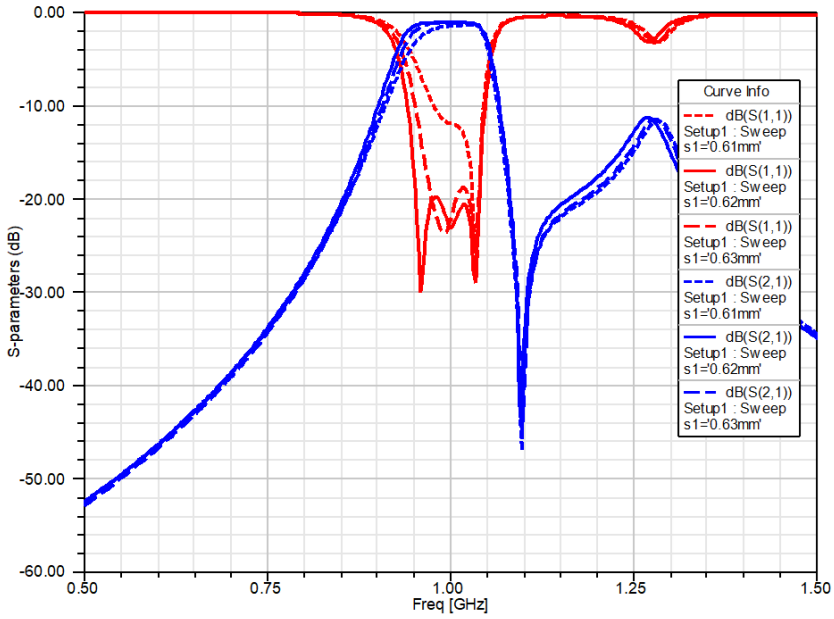

***Figure 4.19**: Results of proposed HFSS simulation with different values of S1*

Figure 4.20 shows the proposed HFSS simulation results with different values of S2. This second parametric study shows the influence of the 'S2' spacing between the second and third resonators. When 'S2' increases, the lower cutoff frequency remains the same and the upper cutoff frequency moves lower. Therefore, 'S2' is the second parameter that affects the HFSS result: when 'S2' increases, the reduced bandwidth

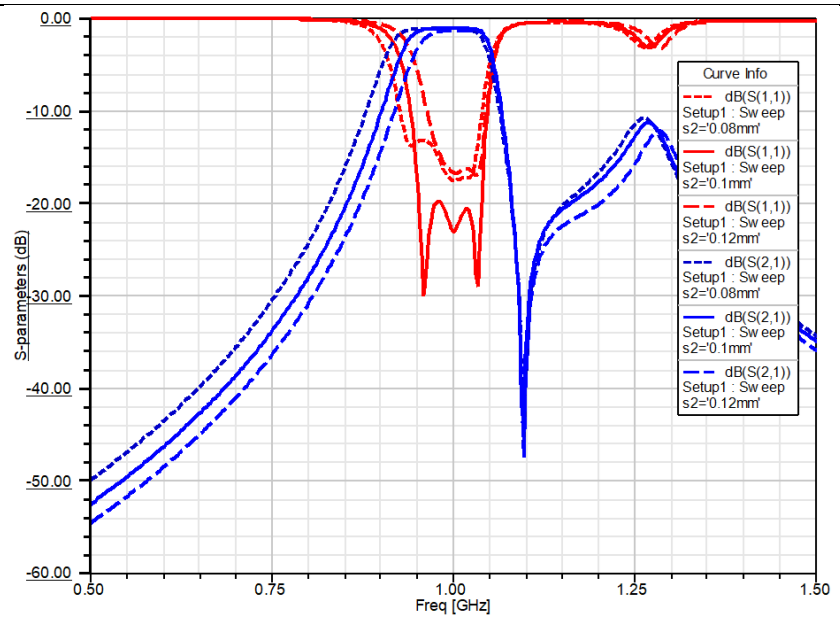

***Figure 4.20** :Résultats de simulation HFSS proposée avec différentes valeurs de S2*

The electric field distribution of the proposed bandpass filter is shown in Figure (4.21)

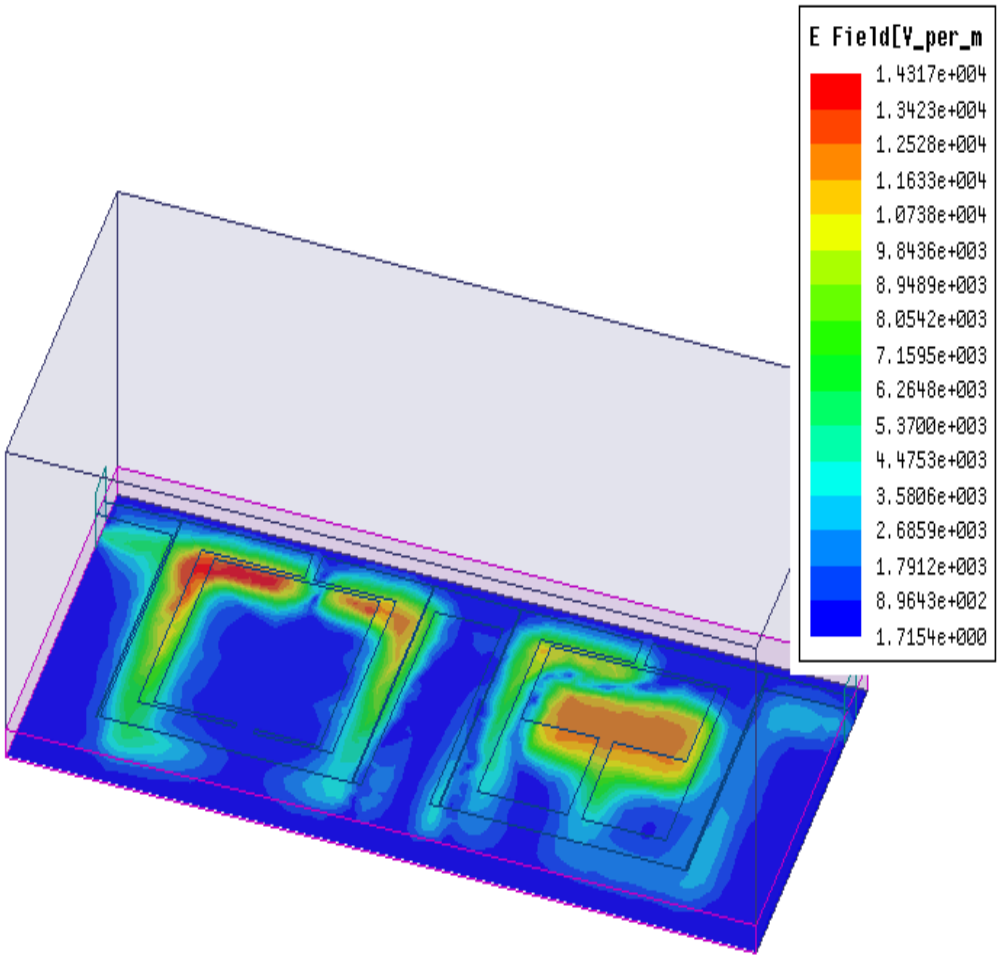

***Figure 4.21**: Distribution of the electric field of the 3th order bandpass filter.*

Figure (4.21) illustrates the electric field distribution of the 3rd order bandpass filter. We notice that the maximum of the E fields is represented by dark colors (high intensity)

In all the cases, it is found that only one modal resonant frequency is affected, while the other one is hardly changed. It can be shown that the mode whose resonant frequency is being affected is an even mode.

4.4SubstrateIntegratedWaveguideFiltersBasedonaDielectricLayerwithPeriodicPerforations:

4.4.1 Bandpass filter in SIW technology

- **Filter specifications:**

Settings	Values
Filter order (Number of poles)	04
Type of approximation	Chebyshev
Central frequency f_0	3.65GHz
Bandwidth (BW) à –3 dB	0.6777GHz
Amplitude of l'ondulationLAr (passband ripple)	0.1 dB
Attenuation	< -20 dB

Table 4.6: SpecificationsBandpass filter in SIW technology

- **Frequency response of the ideal bandpass filter:**

Once the order of the filter is determined, knowing the maximum ripple of A_r= 0.1 dB and the specifications defined in the specifications, we obtain the coefficients g_i (i=1-2) of the bandpass prototype of the type filter Chebyshev:

g_0	g_1	g_2	g_3	g_4	g_5
1	1.1088	1.3062	1.7704	0.8181	1.3554

Using the specifications defined in the specifications to calculate:

Relative bandwidth :

$$\omega_0 = 2\pi f_0 \quad (4.1)$$
$$= 2.2934$$
$$FBW = \frac{BW}{f_0} \quad (4.2)$$
$$= 0.1856 = 18.56\%$$

Quality Factor:

$$Q_e = \frac{g_0 g_1}{FBW} \tag{4.14}$$

$$= \frac{1 * 1.1088}{0.1856} = 5.9718$$

Coupling coefficients:

$$M_{i,i+1} = \frac{1}{\sqrt{g_i g_{i+1}}} \tag{4.7}$$

Qe	$M_{12}=M_{21}$	$M_{23}=M_{32}$	$M_{34}=M_{43}$	Qs
5.9718	0.1543	0.1221	0.1543	5.9718

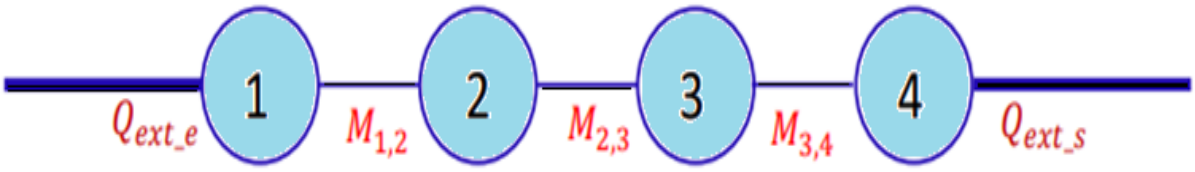

***Figure 4.22**: Order 4 coupling graph of the filter*

- **Coupling matrix**

⇨ **Normalized:**

Summary of this specification gives an order of four (4) and the following coupling matrix:

$$m=\begin{bmatrix} 0 & 1.1 & 0 & 0 & 0 & 0 \\ 1.1 & 0 & 0.83 & 0 & 0 & 0 \\ 0 & 0.83 & 0 & 0.65 & 0 & 0 \\ 0 & 0 & 0.65 & 0 & 0.83 & 0 \\ 0 & 0 & 0 & 0.83 & 0 & 1.1 \\ 0 & 0 & 0 & 0 & 1.1 & 0 \end{bmatrix}$$

⇨ **Dénormalized:**

After determining the normalized coupling matrix [m] for a coupled resonator topology, the actual coupling matrix [M] of a coupled resonator device with given specification can be calculated by prototype de-normalization of the matrix [m] at a desired bandwidth, as follows:

$M_{i,i+1} = m_{i,i+1} .FBW$ For i=1 to n-1 (4.9)

- **Filter equivalent circuit:**

The localized elements $R_0L_0C_0$ of resonators:

$$L_0 = \frac{Z}{\omega_0 Q_e} * 10^9 nH \quad (4.10)$$

$$= 0.3650 \text{ nH}$$

$$C_0 = \frac{Z}{\omega_0 Q_e} * 10^{12} pF \quad (4.11)$$

$= 5.2079 \text{p}F$

$R_0 = 100000\ \Omega$

Resonator impedances :

$$Z_{i,i+1} = \frac{Z}{Q_e M_{i,i+1}} \quad (4.12)$$

Lorsque $Z_0 = 50\Omega$ est l'impédance d'alimentation au niveau des ports d'E/S :

$$Z_{12} = 54.26\Omega$$

$$Z_{23} = 68.57\Omega$$

$$Z_{34} = 54.26\Omega$$

4.4.1.1 Equivalent scheme under AWR:

equivalent circuit in localized elements analyzed with the software (AWR Design Environment) are represented in the figure 4.23

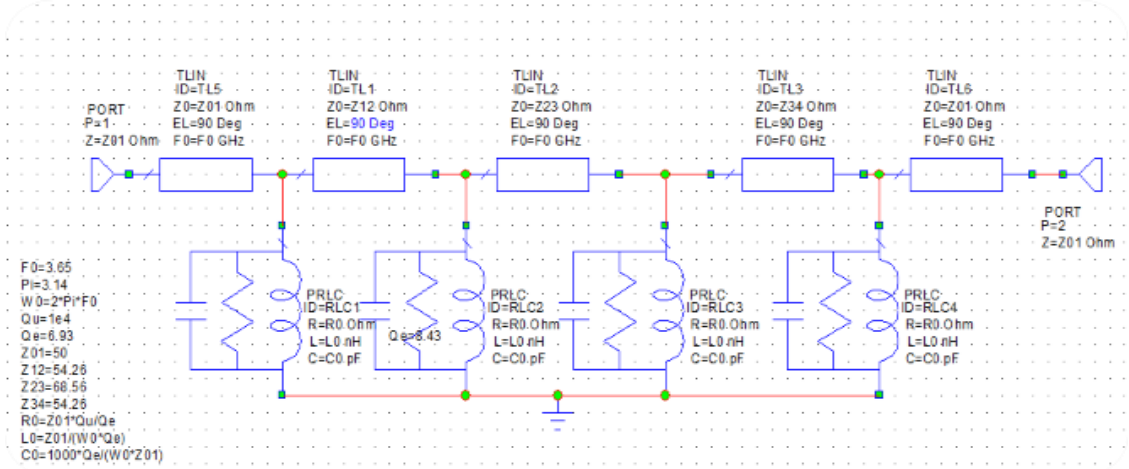

***Figure 4.23**: Schematic circuit of SIW bandpass filter.*

4.4.1.2 design of the bandpass filter in SIW technology:

The topology of our bandpass filter of order 4 is shown in figure (4.24)

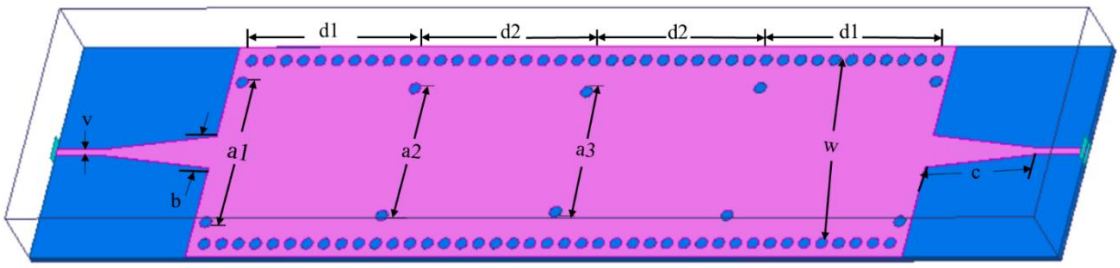

***Figure 4.24**: Geometry of the Bandpass filter in SIW technology*[2].

In the model: Measurements were made in the frequency range from 2.5 GHz to 5.5 GHz figure 4.25

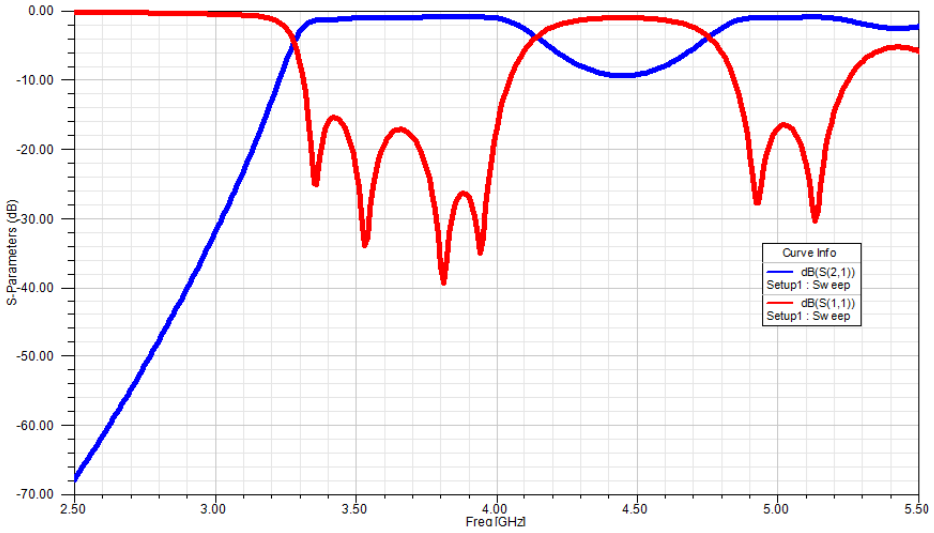

***Figure 4.25**: SIW Bandpass filter simulation results by HFSS*

We present in Figure 4.25, the simulation results of the filter SIW Bandpass filter and transmission obtained with the HFSS software. The central frequency of this filter is of order 4 and f = 3.65 GHz and the bandwidth is approximately 0.6777 GHz. The frequency response shows that|S11| is less than -20dB between 3.2800 GHz and 4.1400 GHz

- **The Electromagnetic design of the applied filter:**

This geometric configuration is simulated on a "Taconic CER-10" substrate having a relative permittivity εr=10, a dielectric loss tangent 0.035 and a thickness of h= 0.64 mm.

Settings	X1	Y1	H	Hs	V	C	L	B	a1	a2	a3	d1	d2	W
Values	20	90	0.035	0.64	0.6		62.7	3.03	13.3	12.1	11.4	15.25	15.1	17.425

Table 4.7: SIW bandpass filter dimensions

4.4.1.3 Field distribution:

A frequency analysis in the [2-4] GHz band **S** of this structure was carried out with the HFSS software.

Figure 4.26 shows the computed magnetic and electric field densities using HFSS-simulator.

As can be seen, the magnetic field is concentrated around the central ground line, so the inductance is determined by the central ground line. The electric field is concentrated around the etched slots, which represents the capacitance.

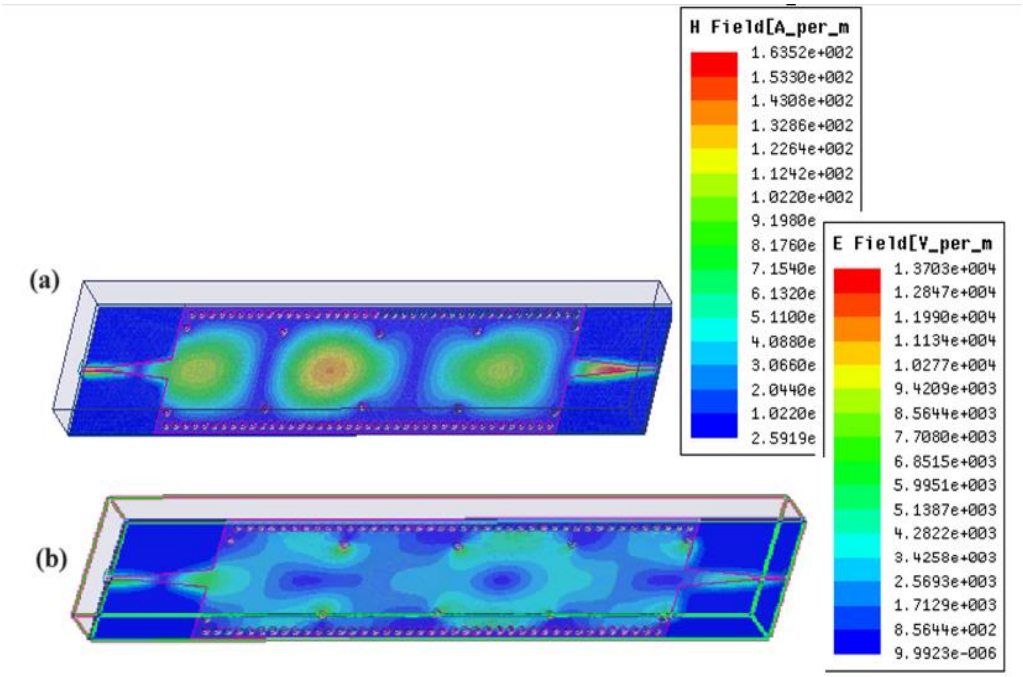

Figure 4.26: *Field distribution along the SIW (a) electric field density (b) magnetic field density*

4.4.2 Filter based on the periodic perforation of the dielectric substrate

- **Filter specifications:**

Settings	Values
Filter order (Number of poles)	04
Type of approximation	Chebyshev
Central frequency f_0	3.65 GHz
Bandwidth (BW) à –3 dB	630 MHz
Amplitude of l'ondulation LAr (passband ripple)	0.1 dB
Attenuation	< -20 dB

Table 4.8: Specificationsof the SIW perforated filter

- **Frequency response of the ideal bandpass filter:**

Once the order of the filter is determined, knowing the maximum ripple of A_r= 0.1 dB and the specifications defined in the specifications, we obtain the coefficients g_i (i=1-2) of the bandpass prototype of the type filter Chebyshev:

g_0	g_1	g_2	g_3	g_4	g_5
1	1.1088	1.3062	1.7704	0.8181	1.3554

Using the specifications defined in the specifications to calculate:

Relative bandwidth :

$$\omega_0 = 2\pi f_0 \quad (4.1)$$
$$= 2.2934$$

$$FBW = \frac{BW}{f_0} \quad (4.2)$$
$$= 0.1726 = 17.26\%$$

Quality Factor:

$$Q_e = \frac{g_0 g_1}{FBW} \quad (4.14)$$
$$= \frac{1 * 1.1088}{0.1726} = 6.4240$$

Coupling coefficients:

$$M_{i,i+1} = \frac{1}{\sqrt{g_i g_{i+1}}} \quad (4.7)$$

Q_e	M_{12}	M_{23}	M_{34}	Q_S
6.4240	0.1434	0.1135	0.1434	6.4240

***Figure 4.27**: Order 4 coupling graph of the filter*

- **Coupling matrix**

⇨ **Normalized:**

Summary of this specification gives an order of four (4) and the following coupling matrix:

$$m=\begin{bmatrix} 0 & 1.1 & 0 & 0 & 0 & 0 \\ 1.1 & 0 & 0.83 & 0 & 0 & 0 \\ 0 & 0.83 & 0 & 0.65 & 0 & 0 \\ 0 & 0 & 0.65 & 0 & 0.83 & 0 \\ 0 & 0 & 0 & 0.83 & 0 & 1.1 \\ 0 & 0 & 0 & 0 & 1.1 & 0 \end{bmatrix}$$

- **Filter equivalent circuit:**

The localized elements $R_0L_0C_0$ of resonators:

$$L_0 = \frac{Z}{\omega_0 Q_e} * 10^9 nH \quad (4.10)$$

$$= 0.3393 \text{ nH}$$

$$C_0 = \frac{Z}{\omega_0 Q_e} * 10^{12} pF \quad (4.11)$$

$= 5.6023$ pF

$R_0 = 100000\ \Omega$

Resonator impedances :

$$Z_{i,i+1} = \frac{Z}{Q_e M_{i,i+1}} \quad (4.12)$$

Lorsque $Z_0 = 50\Omega$ est l'impédance d'alimentation au niveau des ports d'E/S :

$$Z_{12} = 54.26\ \Omega$$

$Z_{23} = 68.57\ \Omega\$$

$$Z_{34} = 54.26\ \Omega$$

4.4.2.2 Design of the bandpass filter in SIW technology:

From the filter synthesis, the geometry of the prototype has been obtained[2]. Originally, in filter synthesis, the equivalent rectangular waveguide was adopted. This structure has been replaced by the SIW structure , adopting metallised vias, with *R*= 0.85 mm and *s* = 0.25 mm . In addition, tapered microstrip to SIW transitions are used to measure the filter. The final dimensions of the filter, shown in (Figure 4.28)

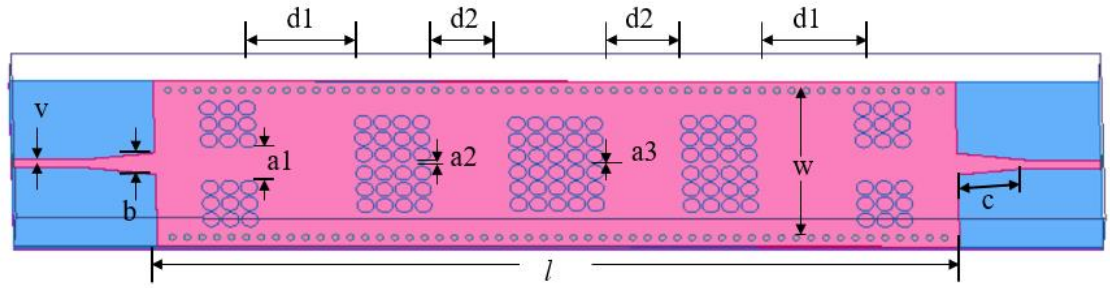

***Figure 4.28**: Geometry of the SIW perforated filter by HFSS*

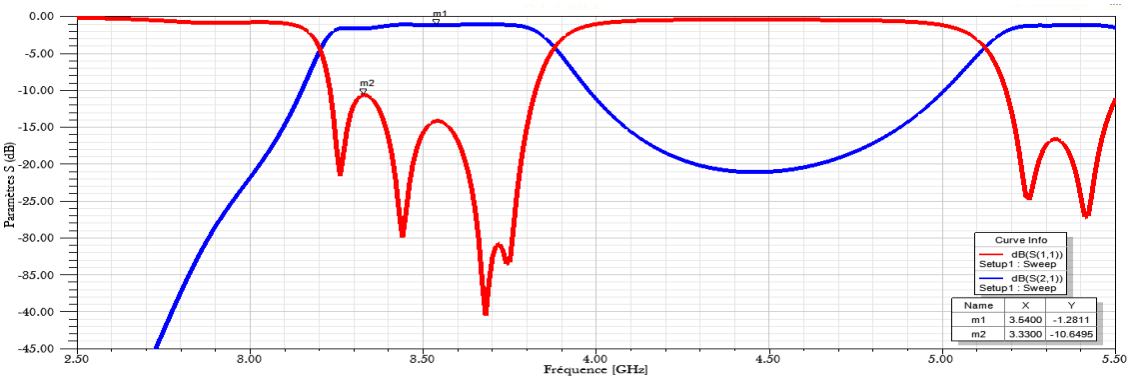

***Figure 4.29** :SIW perforated filter simulation results by HFSS*

- **The Electromagnetic design of the applied filter:**

This geometric configuration is simulated on a “Taconic CER-10” substrate having a relative permittivity εr=10, a dielectric loss tangent 0.035 and a thickness of h= 0.64 mm.

Settings	X1	Y1	H	Hs	V	C	l	b	a1	a2	a3	d1	d2	w
Values	20	110	0.035	0.64	0.6	7	81	2.6	4	0.55	0.25	10	7.95	17.8

Table 4.9: the SIW perforated filter dimensions

4.5 Conclusion:

This chapter presented some original prototypes of bandpass filters. Using analytical equations, we calculated the various synthesis parameters of a bandpass filter, including the coupling matrix, quality coefficients, and initial geometric dimensions. The ideal frequency response of the filter was obtained using an equivalent circuit with lumped elements, modeled with AWR Microwave Office.

We observed that the simulation results for the proposed bandpass filters were satisfactory in both sections. There was a good consistency between the simulation curves produced by HFSS and those generated by AWR design. The results presented in this chapter are encouraging, demonstrating that both SIW technology and planar technology can produce filters with excellent performance.

4.6 References

[1] J.-S. Hong, H. Shaman, and Y.-H. Chun, Dual-mode microstrip open-loop resonators and filters, IEEE Trans. Microwave Theory Techn. MTT-55(8), 2007, 1764–1770.

[2] R. Garg, I. Bahl, and M. Bozzi, *Microstrip Lines and Slotlines*, Third Edition, Artech House, 2013

General Conclusion

General Conclusion

In this dissertationthere have been various designs of devices operating in the microwave frequency range were presented. This process is divided into several stages: approximation, coupling matrix installation, mesh installation, selection of appropriate physical dimensions, fabrication and measurement. Specifically, I have designed band-pass filters using several technology techniques. The first chapter establishes a comprehensive state of the art of planar microwave filtering, underscoring the significance of topologies based on approximation functions and frequency transformations derived from low-pass prototypes. It also categorizes various types of planar filters, based on microstrip lines.

The second chapter explores the uses of defined ground structure (DGS) units in electrical circuit design. It starts with an overview of the basic ideas and significance of DGS units, then dives into a thorough examination of their frequency responses. The chapter examines a number of modeling techniques, such as the extraction of equivalent circuit characteristics, the complexity of N-pole DGS filter design, and modeling issues for RLC systems. It also covers modeling transmission lines, quasistatic techniques including microstrip cross-junctions and microstrip lines, and enhanced LC circuit modeling. In addition, the chapter looks into modeling standalone DGS applications. Finally, it ends with some observations on the various modeling approaches that were covered, along with a list of references for additional reading.

Substrate-Integrated Waveguide (SIW) technology is presented in Chapter 3 as a noteworthy development in millimeter-wave and microwave circuit design. SIW technology enhances functionality and minimizes system size by providing smooth integration with planar circuitry and compatibility with current PCB production techniques. It is perfect for high-frequency applications in wireless communications, radar, satellite communication, and sensor networks because of its low loss, high Q-factor, and wide bandwidth performance.

Because of SIW's design flexibility, different passive and active components that are suited for certain applications can be created. Persistent research endeavors to tackle obstacles like heat regulation and manufacturing tolerances, while also broadening the scope of SIW applications to encompass terahertz and photonic systems. SIW technology, which balances performance, integration, and ease of use, is well-positioned to spur innovation in communication and sensing technologies.

In Chapter 4, the first bandpass filter prototypes are displayed. Analytical formulas were used to calculate the bandpass filter's synthesis parameters, including the coupling matrix, quality coefficients, and beginning geometric dimensions. To find the ideal frequency response of the filter, an equivalent circuit with lumped elements was simulated using AWR Microwave Office. The simulation results for the recommended bandpass filters, which were produced using the HFSS and AWR designs, were sufficient and demonstrated good consistency. The results show the promise and efficacy of planar and SIW technologies by showing that they can both produce filters with remarkable performance.